DESIGN, FABRICATION, AND STATIC TESTING OF ATTACHED INFLATABLE DECELERATOR (AID) MODELS

GER-14940

1 MARCH 1971

COPY No 24

GOODYEAR AEROSPACE CORPORATION

AKRON, OHIO

DESIGN, FABRICATION, AND STATIC TESTING OF ATTACHED INFLATABLE DECELERATOR (AID) MODELS

By G. L. Faurote

Prepared under Contract No. NAS1-9726 by
GOODYEAR AEROSPACE CORPORATION
Akron, Ohio

for

Langley Research Center

NATIONAL AERONAUTICS AND SPACE ADMINISTRATION

FOREWORD

Work described in this document was performed by Goodyear Aerospace Corporation, Akron, Ohio, under NASA Contract NAS1-9726. The contractor's number for this report is GER-14940.

CONTENTS

ILLUSTRATIONS

TABLES

DESIGN, FABRICATION, AND STATIC TESTING OF ATTACHED INFLATABLE DECELERATOR (AID) MODELS

By G. L. Faurote
Goodyear Aerospace Corporation

SUMMARY

Goodyear Aerospace Corporation (GAC) designed and fabricated wind-tunnel models of an Attached Inflatable Decelerator (AID) for the NASA Langley Research Center (LRC). An AID is a flexible canopy, deployed and inflated by ram air, which is attached to the base of the body to be decelerated. The geometry of the canopy can be tailored to the application for which it is intended and to the available attachment locations.

Three models were furnished by Goodyear Aerospace for the current program: two AID canopies were attached to a simulated payload within a 120-deg conical aeroshell while the third canopy had an outer attachment to a 140-deg conical aeroshell and an inner attachment to a simulated payload. All models utilized four quick-release aeroshell inlets for deployment and four canopy inlets to produce final canopy pressurization.

An inflation test was conducted in an environmental chamber to investigate packing, deployment, and inflation characteristics of the model prior to wind-tunnel testing.

I. - INTRODUCTION

The need for a deceleration system with good operational characteristics at supersonic speeds has led to the development of an Attached Inflatable Decelerator (AID). An AID is a flexible canopy normally deployed and inflated by ram air, which is attached to the base of the body decelerated.

A summary of the extensive analytical and experimental development of the AID to date is presented in References 1 through 8. The encouraging results of these development efforts have prompted planetary-mission studies (References 1 and 9) in which the AID is considered for application as an initial stage of a two-stage deceleration system. Basically, this two-stage approach takes advantage of the high supersonic drag of the AID and the high subsonic drag of a terminal stage parachute such as the disk-gap-band parachute (see Figure 1). Reference 1 indicates that for entry into the low density atmosphere of Mars, the AID will relax the stringent deployment conditions on the parachute and will provide significant increases in landed-payload mass without increasing the size of the basic entry aeroshell (see Figure 2). To compliment the work accomplished in Reference 1, Goodyear Aerospace is performing a parametric thermal and stress analysis of an AID operating in the most severe of the postulated Mars atmospheres. The results of this work are presently unpublished.

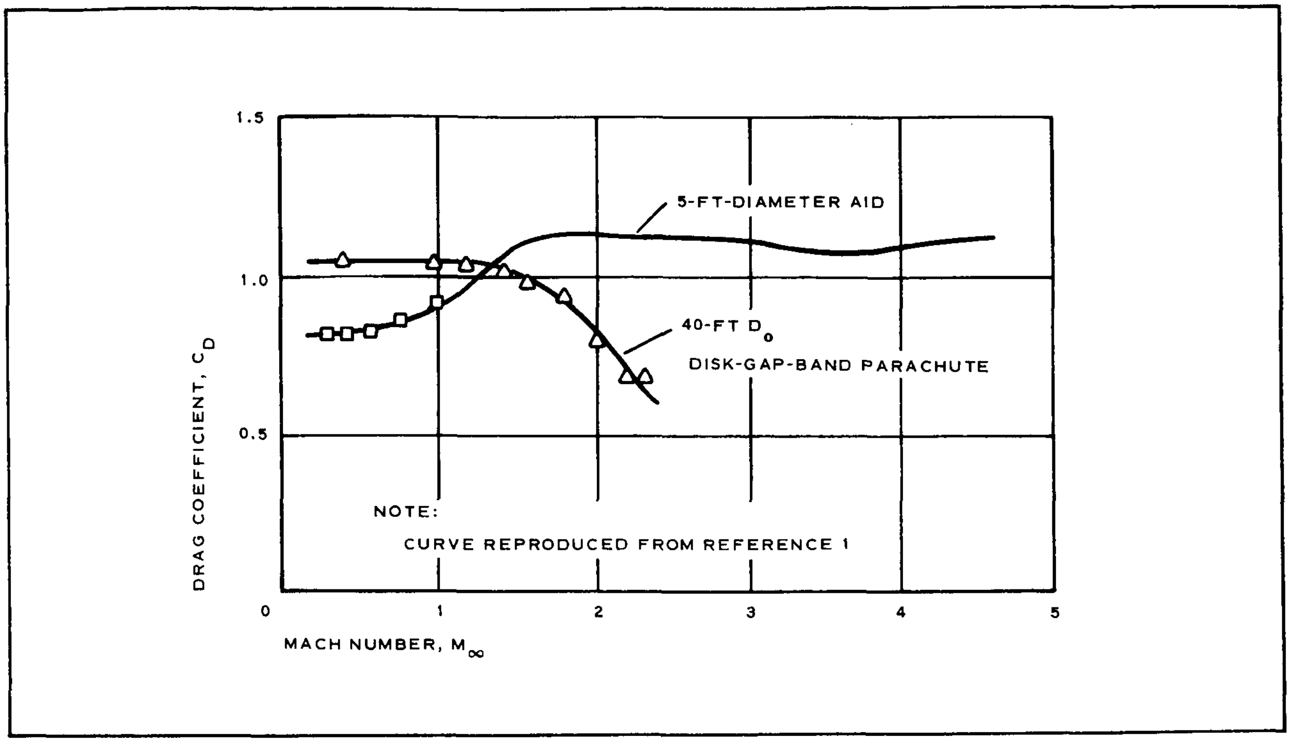

Figure 1. - Drag Performance of AID and Disk-Gap-Band Parachute

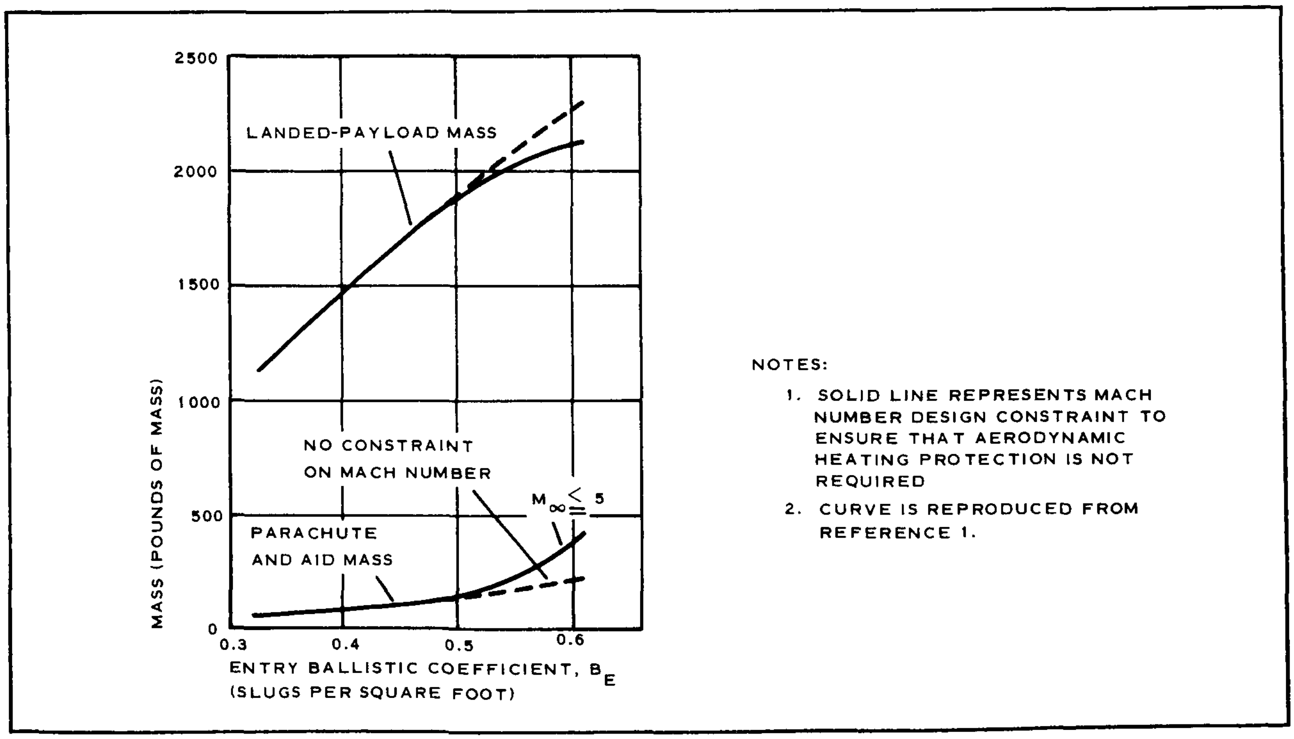

Figure 2. - Variations in Decelerator Mass and Landed-Payload Mass with Ballistic Coefficient

The current investigation is part of a continuing effort by LRC to develop and evaluate the AID. Since the AID is aerodynamically shaped, its canopy may be tailored to the application for which it is intended and to the available attachment locations. The detailed design presented in Reference 3 is for an AID attached to the periphery of a 120-deg conical aeroshell with inflation initiated by a water vaporization system. Utilizing the same aerodynamic shape, the inflation system was subsequently replaced with ram air inlets located at the aeroshell periphery (see Reference 1). Key features of the design presented herein are the canopy attachment to a simulated payload interior to the periphery of the aeroshell and small ram-air inlets as an integral part of the aeroshell. Thus, the objectives of the program are the design, fabrication, and static testing of AID models in preparation for wind tunnel testing to evaluate the following: (1) demonstrate ram-air deployment of the AID by quick-opening aeroshell inlets; (2) investigate the supersonic behavior of the canopy in the vicinity of the aeroshell rim where the canopy is unrestrained; (3) determine the effect of increased inflation time on the deployment integrity of the AID; and (4) measure the transient loads in the meridional tapes of the AID. These objectives are discussed in detail at various points throughout the report.

SYMBOLS

A	area, sq in.
B	ballistic coefficient, slugs/sq ft
C_D	drag coefficient based on maximum projected diameter
c_p	pressure coefficient, $p_L - p_\infty/q_\infty$
D	diameter, in.; drag, lb
d_g	depth of lobe, in.
E	Young's modulus, psi
F	circumferential membrane stress coefficient; force, lb
F.S.	factor of safety
F_t	tensile strength, lb; lb/in.
f	fabric stress, lb/in.
$\bar{f}$	nondimensional fabric stress
f_c	circumferential fabric stress resultant, lb/in.
f_m	meridional fabric stress resultant, lb/in.
H	compressible form factor
h	inlet height, in.

k	constant dependent upon material properties
l	length, in.
M	Mach number
M.S.	margin of safety
$\dot{m}$	mass flow, slugs/cu ft
N	stress, lb/in.
n	number of gores
p	$p_i - p_b$, psf; static pressure, psf
p_{t_2}	total pressure across bow shock, psf
q	dynamic pressure, psf
R	maximum canopy radius excluding burble fence, in.; gas constant, ft-lb/lb-deg R
r	aeroshell base radius, in.
r_g	lobe radius, in.
s	surface distance from apex to base of aeroshell
S_g	half-arc length of lobe, in.
T	tension, lb
$\bar{T}$	nondimensional meridional tape load
u	free-stream velocity, fps
V	velocity, fps
V_a	aeroshell volume, cu ft
V_b	burble fence volume, cu ft
V_c	canopy volume, cu ft
V_e	total enclosed volume, cu ft
x	inlet width, in.
β	central half-lobe angle, deg; constant dependent upon material properties
γ	bias thread set angle, deg, ratio of specific heats for air
Δ	elongation, in.
δ	boundary layer thickness, in.; elongation, in./in.
δ^*	displacement thickness, in.

ϵ	strain due to thread racking, in./in.
θ	local surface angle relative to direction of free-stream flow, deg; momentum thickness, ft; circumferential direction
λ	porosity
μ	Poisson's ratio
σ	stress, psi
ϕ	meridional direction

Superscript

k	constant dependent on material properties

Subscripts

a	aerodynamic; aeroshell
b	direction of bias threads; base; bending
br	bearing
c	canopy, closed
E	entry
e	external
f	fabric; final; forward
fm	maximum friction force, lb
i	internal; initial, inlet
is	inlet spring
L	local
m	meridian, maximum
o	stagnation; nominal
p	porosity, pressure, principal
r	rear
rl	release lever
s	surface, shear, spring
t	total
u	ultimate
η	inlet efficiency
θ	circumferential direction of surface element
ϕ	meridional direction of surface element
∞	free stream

II. - AID MODEL DESCRIPTION

The configuration details of each of the three AID models discussed in this report are shown in Figures 3 through 5. Additional design details of the models described in Figures 3 through 5 are presented in assembly Drawings 645A000-003-101, -103, and -105, respectively. These assembly numbers will be used in any future reference made to specific details of the models. A complete set of drawings for the models is presented in Appendix A.

The models shown in Figures 3 through 5 are similar to those previously designed and fabricated by Goodyear Aerospace for supersonic wind-tunnel evaluation by LRC. However, important differences that relate to the objectives of this investigation do exist. To point out these differences, the configurational details of the models previously tested are presented in Figures 6 and 7; additional details of these models are presented in References 3 and 1, respectively. The model shown in Figure 6 was deployed by rapid vaporization of a water-alcohol solution. Vaporization of this solution provided sufficient internal pressure to erect the ram-air inlets, which then fully inflate the model. The model shown in Figure 7 was deployed and inflated entirely by ram air. The forward inlets, packaged behind the aeroshell prior to deployment, are released at deployment and create sufficient internal pressure to erect the rear canopy inlets, which then produce full inflation. A model also was tested successfully that used only the forward inlets.

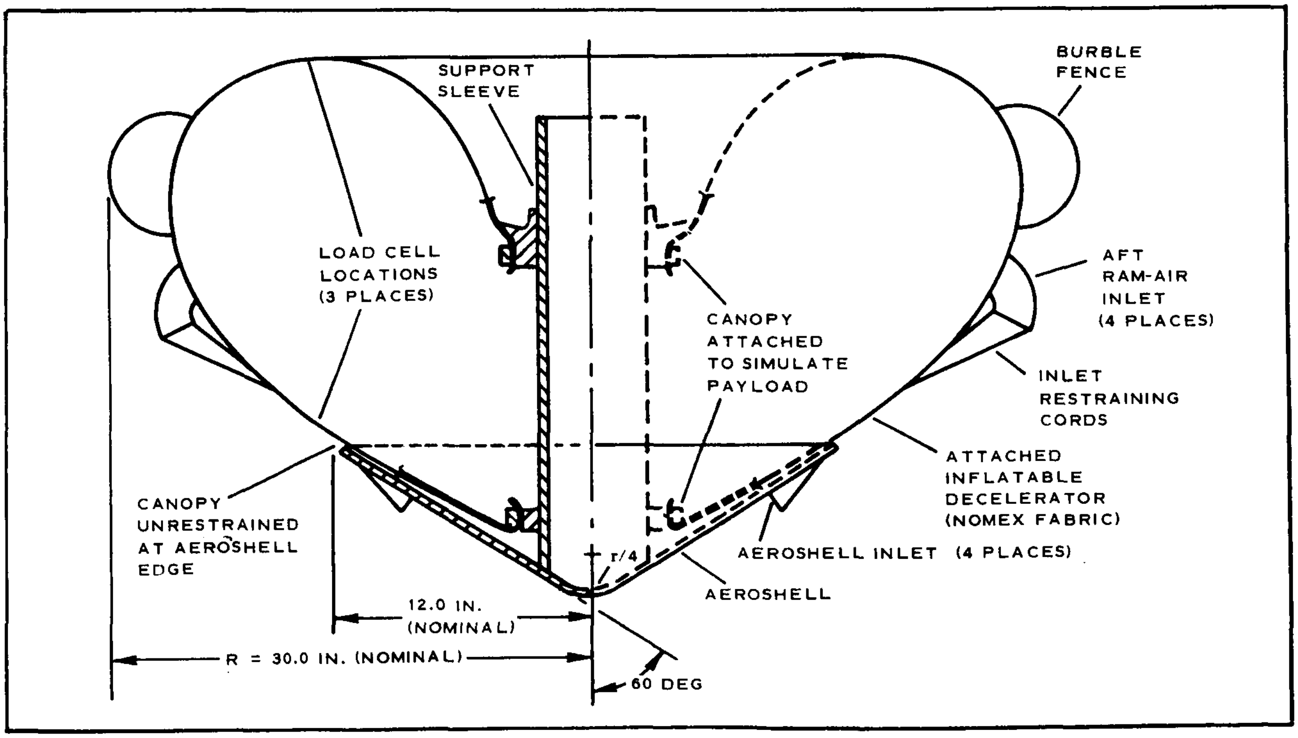

Figure 3. - Details of -101 Assembly

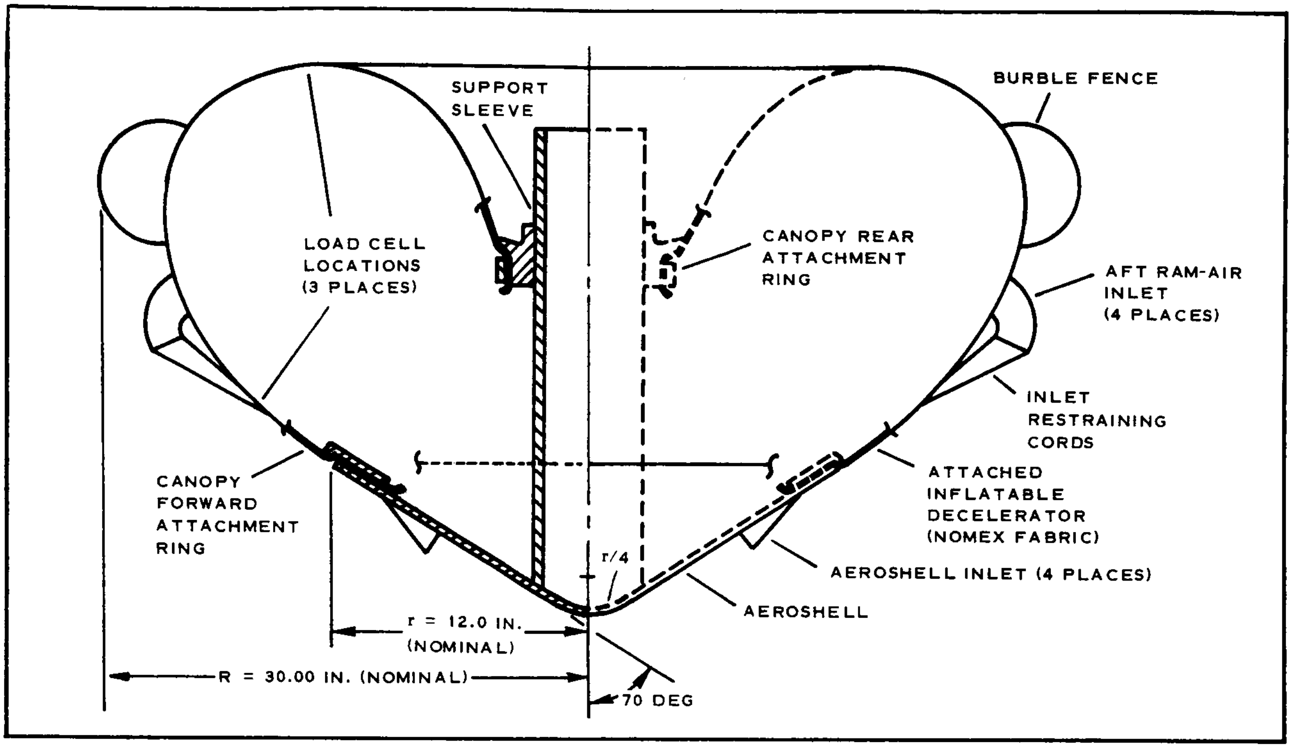

Figure 4. - Details of -103 Assembly

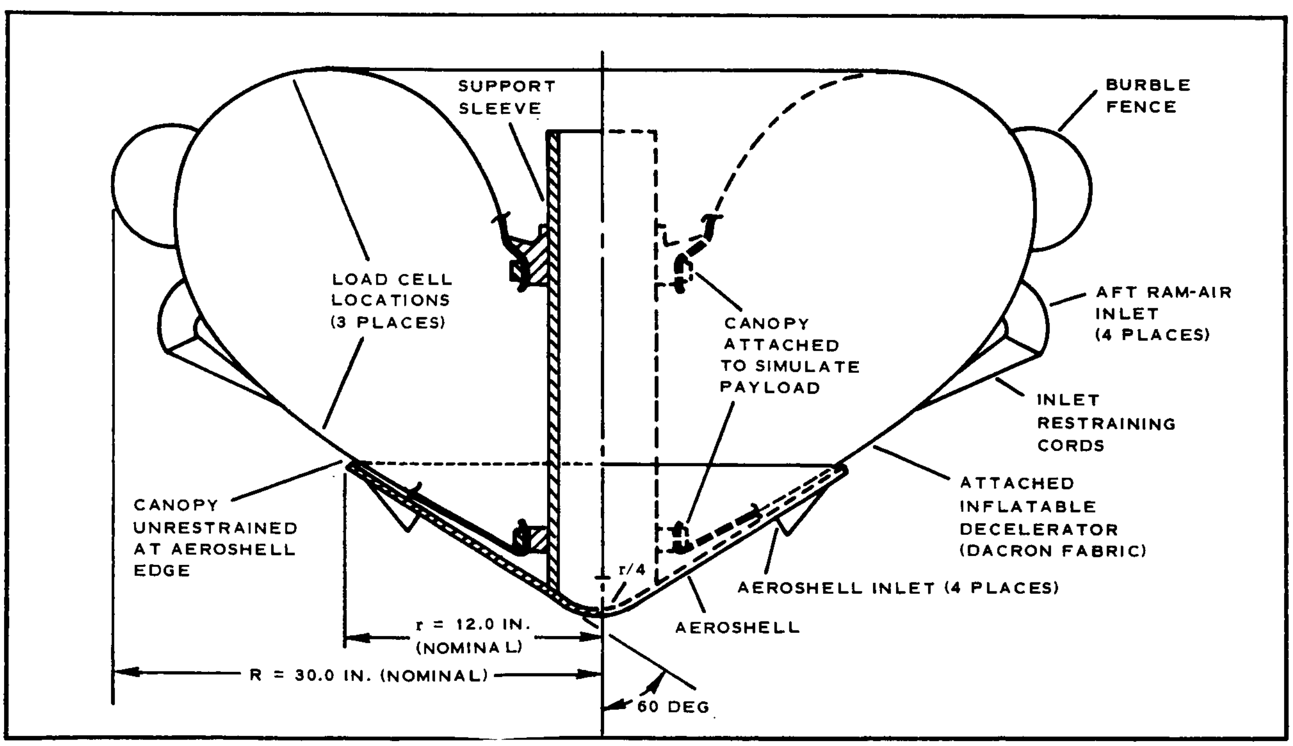

Figure 5. - Details of -105 Assembly

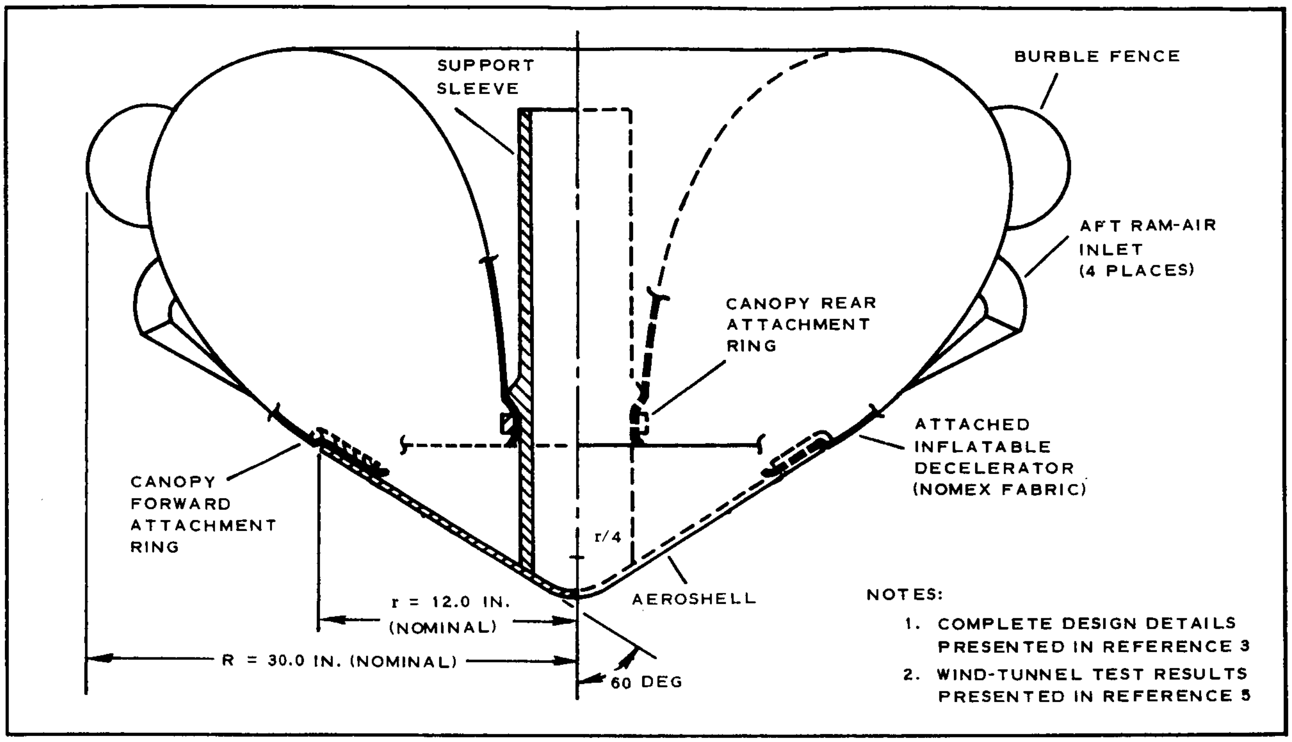

Figure 6. - Details of AID Deployed by Water-Alcohol Solution

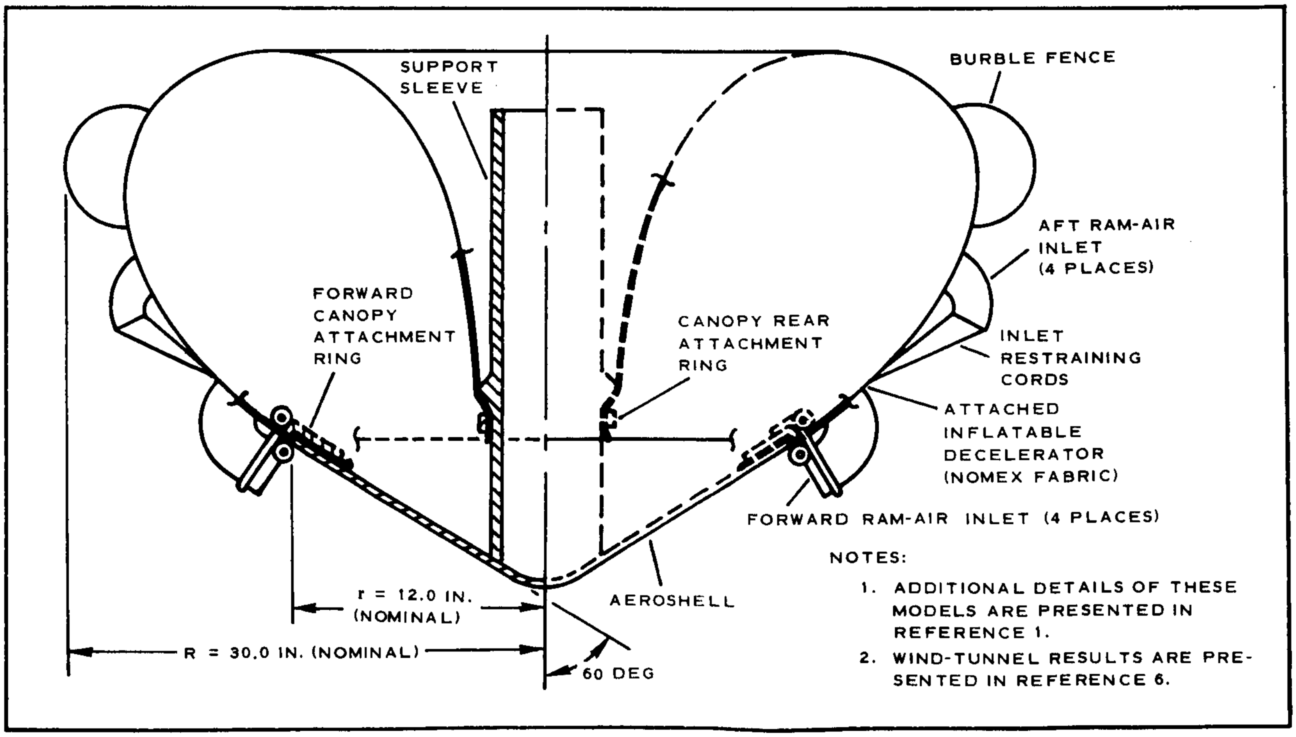

Figure 7. - Details of Ram-Air Deployed AID

The use of ram air to deploy the AID, rather than water-alcohol, would provide a weight savings, which is of obvious importance in the design of a flight unit. In addition, the ram-air deployment technique eliminates the potential problem of sterilization associated with using a liquid-vaporization system for planetary mission applications.

It may be advantageous in certain instances to have available an alternative ram-air deployment scheme to that described above. Therefore, one purpose of this investigation was to develop a system whereby the AID canopies are deployed by four symmetrically located aeroshell inlets. As in the models previously tested, the canopy inlets are retained to provide full inflation and final pressurization.

III. - DESIGN CONDITIONS

The aerodynamic and structural design conditions for the AID canopies are presented in Table I. The hard structure was designed to meet the requirements specified in Arnold Engineering Development Center (AEDC) Document QCP-000-21.

TABLE I. - AID DESIGN CONDITIONS

Condition	Magnitude
Maximum inflated radius, R_p	2.5 ft
Canopy attachment	
Forward	$x/R = 0.1538$; $y/R = -0.745$
Aft	$x/R = 0.1538$; $y/R = 0.291$
Nondimensional meridional tape load, $\bar{T}$	0.44
Nondimensional fabric, f	0.09
Number of gores, n	48
Ratio of circumferential fabric stresses to meridional stresses, f_c/f_m	$0.8 \leqq f_c/f_m \leqq 2.0$
Free-stream Mach number, M_∞	3.0
Free-stream dynamic pressure, q_∞	120 psf

IV. - AERODYNAMIC ANALYSIS

General

The AID, which is constructed by overlaying a coated fabric with many load-carrying meridional tapes (see Figure 8), is basically a uniform-stress (isotensoid) structure as described in Reference 4.

The canopy shape is maintained by pressure recovered from ram-air inlets aligned with the local airflow. For subsonic speeds, a burble fence on the AID is necessary to provide stable operation.

Shape Analysis

The entire isotensoid analysis as applied to the AID was computerized during a previous program (Reference 3) conducted by Goodyear Aerospace for LRC. That analysis utilizes a theoretical aerodynamic pressure distribution to calculate an initial shape. The initial shape then can be used to obtain an experimental pressure distribution which may be inserted in the computerized analysis to obtain an "iterated" shape. This procedure can be repeated until the desired correlation is obtained.

The pressure distribution and shape (profile) for the current AID models were derived in Reference 3. The derivation of the pressure distribution used

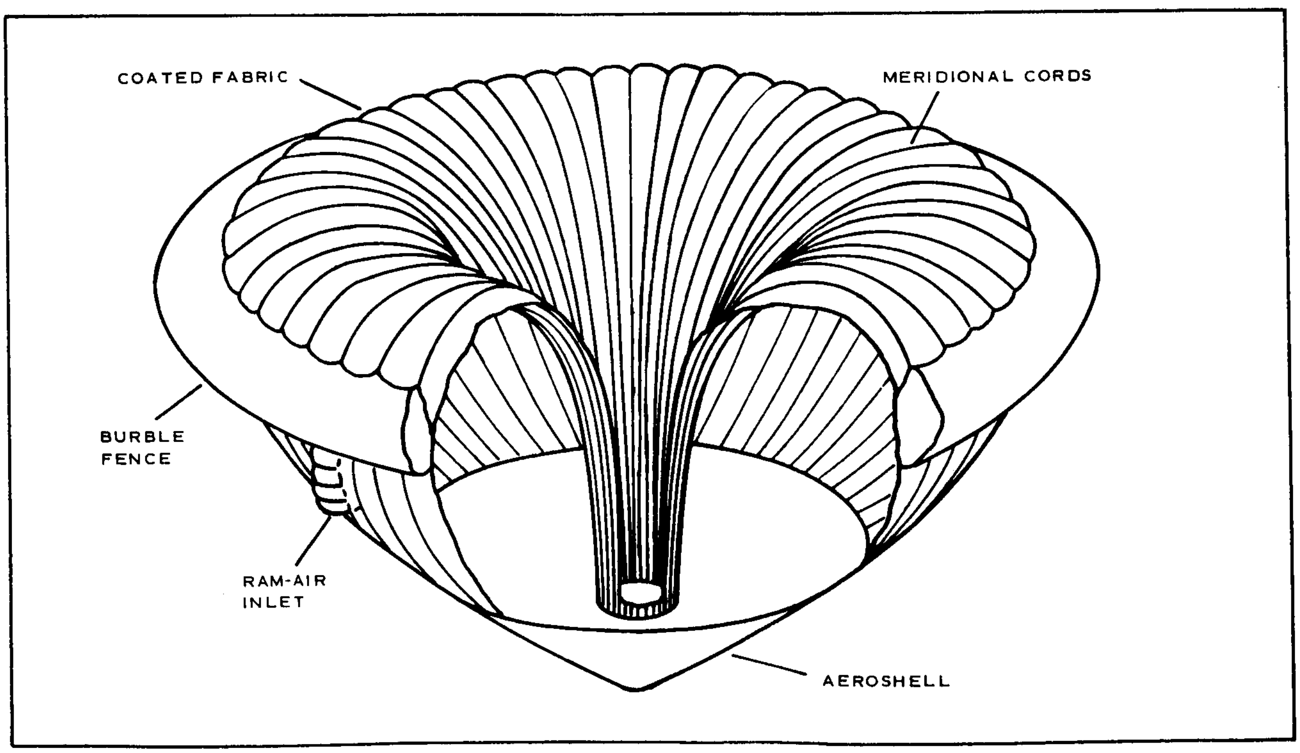

Figure 8. - Cutaway Drawing of an AID

modified Newtonian aerodynamics over the front surface of the AID and a base pressure equivalent to the free-stream static pressure. For the front surface, modified Newtonian aerodynamics relate the pressure coefficient, c_p, to the stagnation pressure coefficient, $c_{p_{max}}$ by the following relation:

$$c_p = c_{p_{max}} \sin^2 \theta ,$$

where

$$c_p = (p_L - p_\infty)/q_\infty ,$$

$$c_{p_{max}} = (p_o - p_\infty)/q_\infty ,$$

and

$$\theta = \text{local surface angle to free-stream flow.}$$

The internal canopy pressure was obtained from the empirical relation:

$$p/q_\infty = (p_i - p_b)/q_\infty$$

$$= 2.0$$

The pressure distribution derived in Reference 3 and an experimental distribution subsequently obtained by LRC (Reference 11) on a rigid wind-tunnel pressure model is presented in Figure 9. As can be seen, the calculated and measured pressure coefficients are in fair agreement over the primary AID profile.

Inflation Analysis

AID models previously tested in the wind tunnel were designed (see References 1 and 3) for rapid inflation ($t_f \leq 0.4$ sec). As the size of an AID increases, for instance to a 20-ft-diameter flight test model, the feasibility and advisability of inflating the AID within 0.4 sec is questionable. While the volume of the AID increases as a function of its radius cubed, the inlet area increases only as a function of the inlet radius squared. Therefore, to maintain the same AID volume-to-inlet area ratio, which is essential if the inflation times are to be the same for a given set of free-stream conditions, the inlet sizes begin to get cumbersome. Additionally, large local fabric velocities (possibly great enough to cause canopy failure) could occur during the inflation of a 20-ft-diameter AID within 0.4 sec. However, excessively long inflation times have the apparent disadvantage of permitting the canopy to flag in the airstream, possibly resulting in canopy failure. To investigate the effects of longer inflation times on the AID canopy, the ram-air inlets were sized to extend the inflation time in excess of one second.

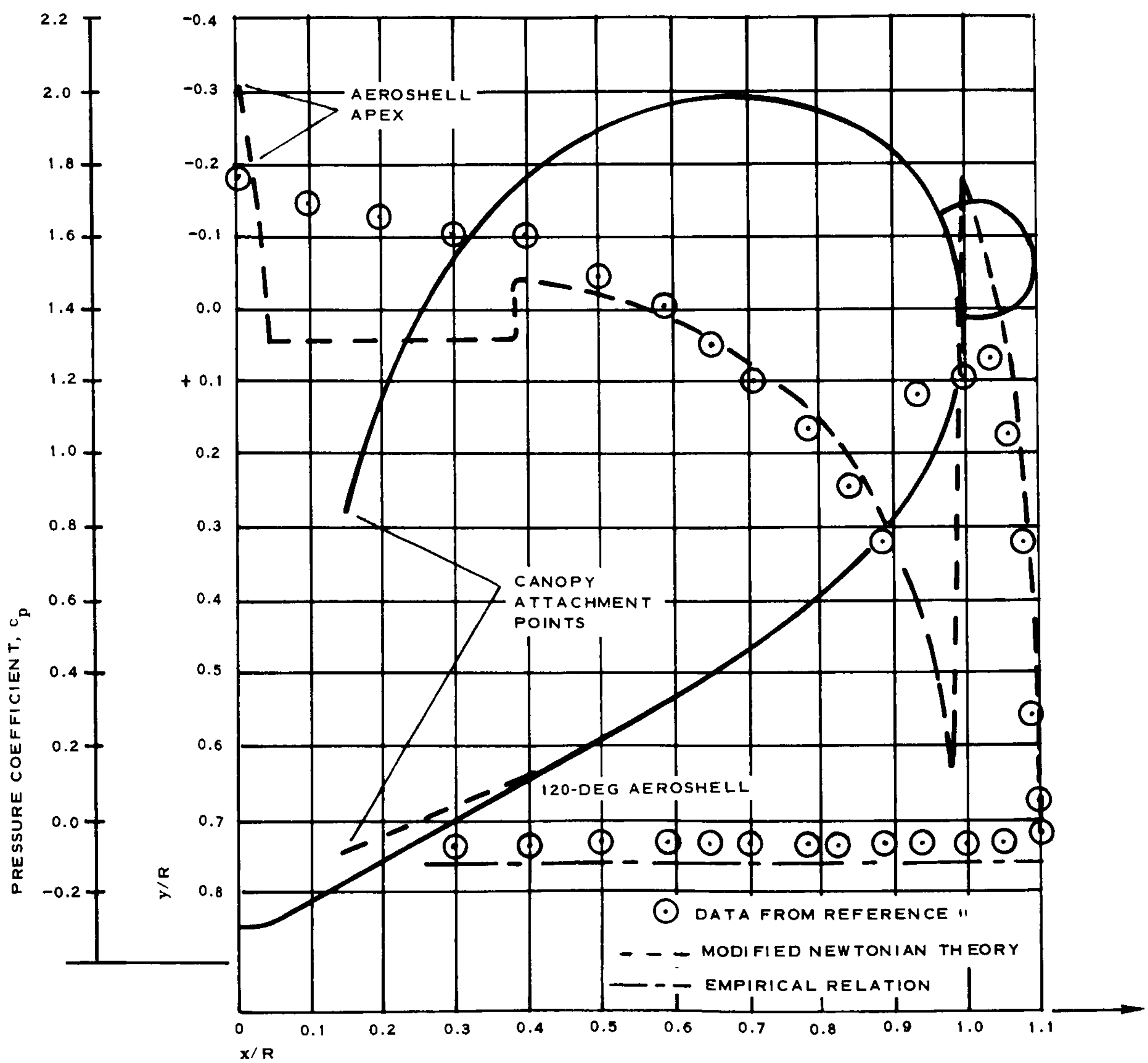

Figure 9. - Comparison of Experimental and Analytical Pressure Distributions for Current Canopy Shape ($M_\infty = 3.0$)

A computerized inflation analysis (see Appendix C), similar to the method described in Reference 1, was used to determine inlet size and inflation rate. To establish the validity of the method, the inflation times of three previously tested AID wind-tunnel models (Reference 6) were calculated. The correlation obtained for those models is presented in Figure 10.

Figure 10B shows the comparison for the AID with dual inlets. Using the analysis of Appendix C the following values of volume-to-inlet area ratios were chosen for the present models.

1. At deployment (aeroshell inlets only),

$$V_e/A_f = 8600 \text{ in.} \qquad (1)$$

2. After deployment (aeroshell and canopy inlets),

$$V_e/(A_f + A_r) = 2860 \text{ in.} \qquad (2)$$

For these restrictions on volume-to-inlet area ratio the resulting predicted inflation time is 1.5 sec as shown in Figure 11.

To solve for the actual inlet dimensions, the total enclosed volume (see Figure 12) must be determined. The canopy volume V_c is determined from the isotensoid computer analysis described in the previous section.

The total enclosed volume then is:

$$V_e = V_c + V_b + V_a{}^{*}$$

$$= 23.95 + 1.4 + 0.3$$

$$= 25.65 \text{ cu ft .}$$

*The volume difference between the 120- and 140-deg aeroshell is small and therefore, only the one value presented was considered.

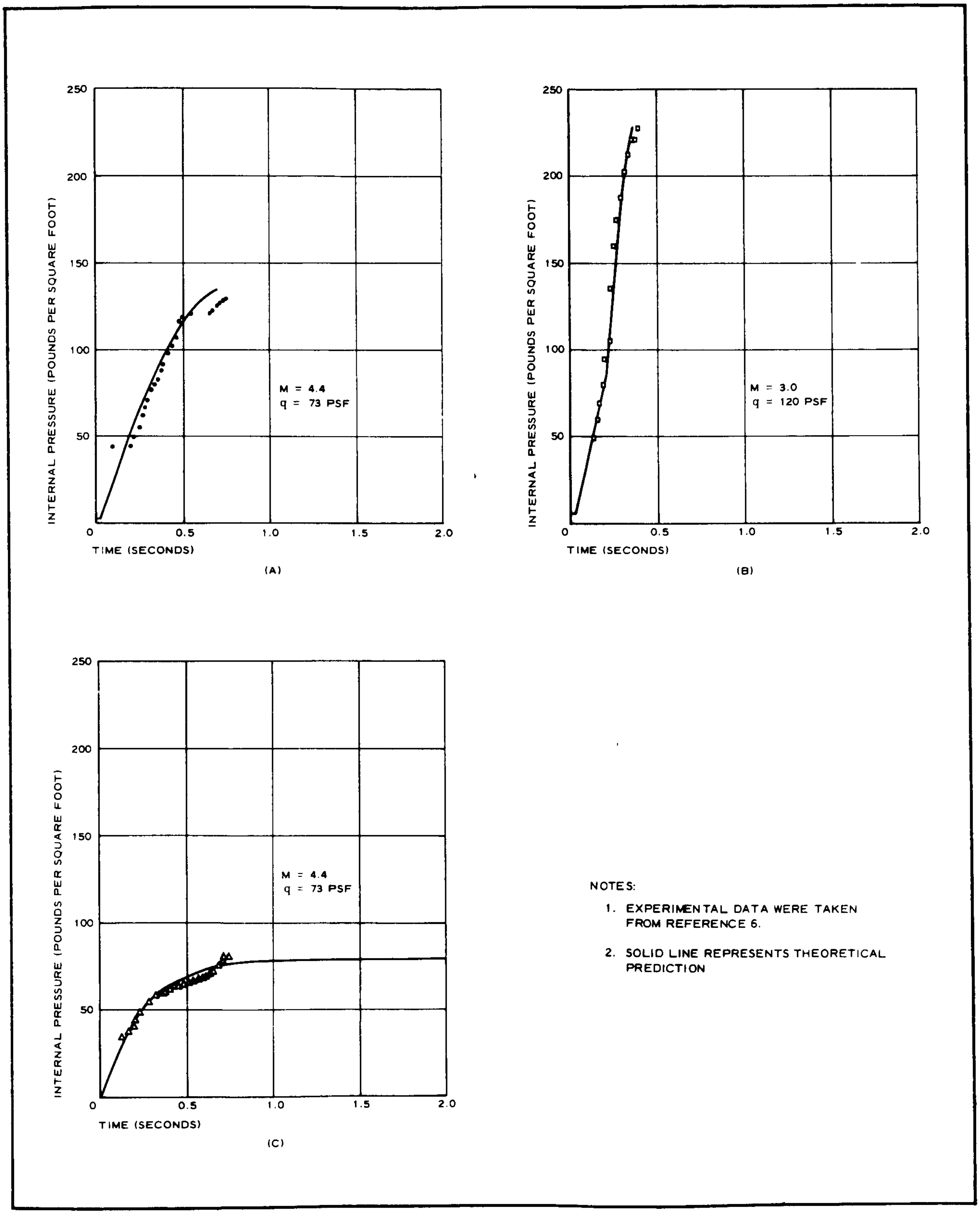

Figure 10. - Correlation of Experimental and Predicted Inflation Analysis Results

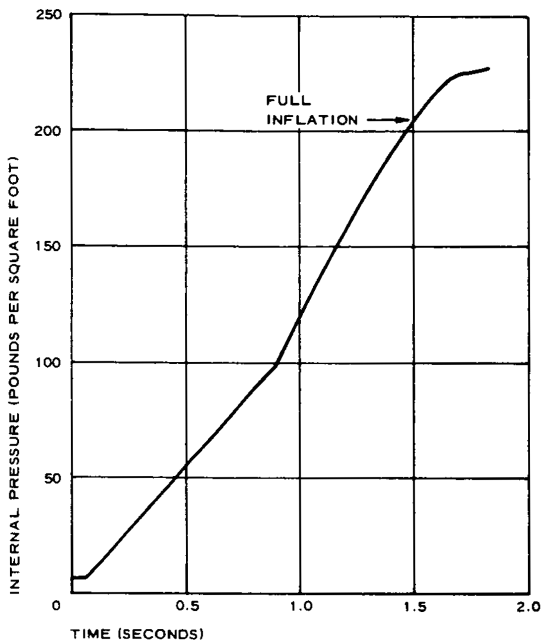

Figure 11 . - Predicted Inflation Rate for Specified Inlet Sizes

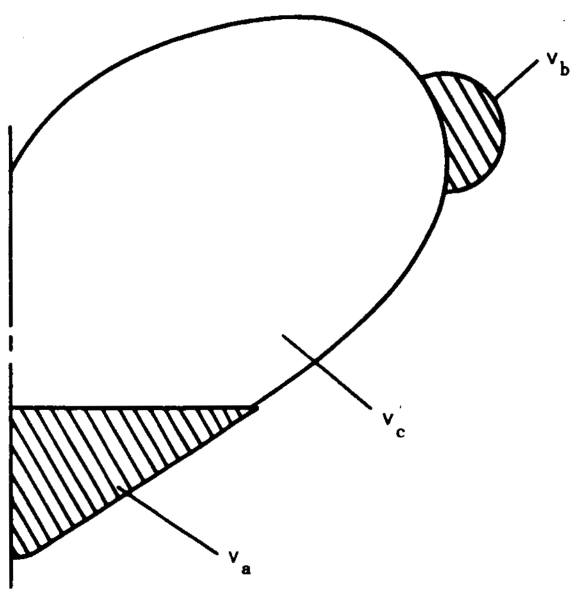

Figure 12. - Reference Areas of AID

From Equation 1

$$A_f = \frac{V_e}{8600 \text{ in.}}$$

$$= \frac{(25.65)(12)}{8600 \text{ in.}} \qquad (2)$$

$$= 5.15 \text{ sq in.}$$

The required effective area for each of the four aeroshell inlets then becomes $A_f/4$ of 1.285 sq in. From Equation 2

$$V_e/(A_f + A_r) = 2860 \text{ in.}$$

Therefore,

$$2860\ A_r = (25.6)(12) - (2860)(5.15) ,$$

or

$$A_r = 10.3 \text{ sq in.}$$

The required open area for each of the four canopy inlets then becomes $A_r/4$ of 2.56 sq in.

As shown in Figure 13, the aeroshell inlets are submerged partially in the

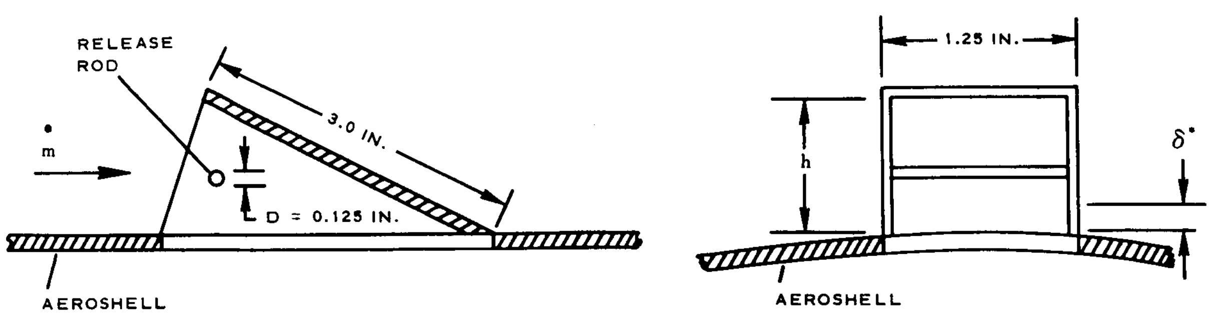

Figure 13. - Aeroshell Inlet Geometry

forebody boundary layer flow. As a result the boundary layer effects must be considered in sizing the inlets. In Figure 14, two general types of thicknesses associated with a typical boundary layer are depicted. By definition the displacement thickness, δ^*, defines the distance through which the body streamline is shifted due to the formation of the boundary layer. Since the displacement thickness describes a region of zero velocity and, therefore, zero mass flow, the height of the inlets (see Figure 13) must be increased by δ^*.

For the given wind-tunnel test conditions and based upon an aeroshell diameter of two feet, the Reynolds number for the upper one-third of the aeroshell surface is found to be on the order of 10^6. Therefore, a turbulent boundary layer analysis was reformed by using the momentum integral solution of Reference 12. A computer program from Reference 13 was utilized in the solution.

The program yielded the following values for the boundary layer momentum thickness, θ:

1. For the 120-deg cone: $\theta = 0.14315 \times 10^{-2}$ ft

2. For the 140-deg cone: $\theta = 0.15182 \times 10^{-2}$ ft

From Reference 12 a compressible form factor, H, is given by:

$$H = \frac{\delta^*}{\theta} .$$

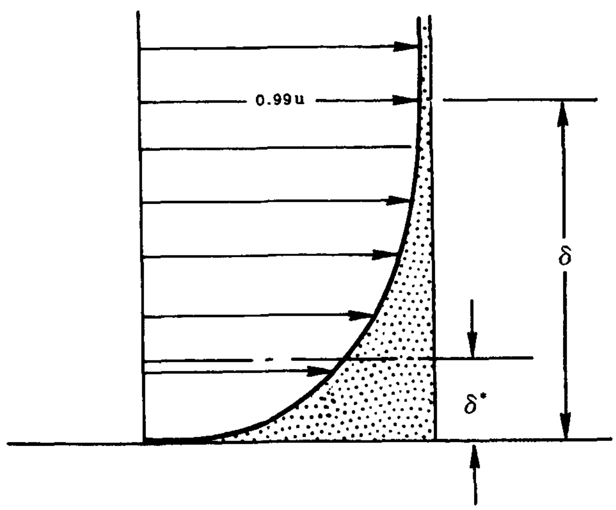

Figure 14. - Thicknesses Associated with Boundary Layer

For M_∞ = 3.0, H = 5.4. By using the results above for the momentum thickness, the displacement thickness is:

$$\delta^* = 0.0929 \text{ in. (120-deg cone)},$$

and

$$\delta^* = 0.0977 \text{ in. (140-deg cone)}.$$

The larger of these two values was utilized in arriving at the inlet height. Additionally, the diameter of the inlet release rod was accounted for in determining the inlet height. From Figure 13 the inlet height is:

$$h = \delta^* + d + \frac{A_r}{4x}$$

$$= 0.977 + 0.125 + \frac{5.15}{4(1.15)}$$

$$= 1.34 \text{ in.},$$

where x = 1.15 in. was chosen as being convenient from a fabrication standpoint.

The rear inlets of the AID models shown in Figures 6 and 7 were displaced approximately 0.25 in. from the canopy surface to minimize boundary layer effects. Based on the effective performance of those inlets during the wind-tunnel tests, the rear inlets of the current models were displaced a similar distance from the canopy. From the area of each rear inlet, which was previously established as 2.56 sq in., the diameter is:

$$D = \frac{4}{\pi}(2.56)^{1/2}$$

$$= 1.80 \text{ in.}$$

V. - SYSTEM DESIGN

Aeroshell Inlets

The aeroshell inlets are forced into the airstream by a sliding flat spring. When in the extended position, the inlet spring directs the air flow into the canopy. While other types of springs also were considered for deploying the inlets, the sliding flat spring was chosen primarily because of its compactness. Figure 15 is a photograph of the internal surface of the aeroshell showing the inlets prior to deployment. The inlets are restrained in the closed position by the release lever. As shown in Figure 15 the four release levers are connected mechanically by the restraining wire. The restraining system shown

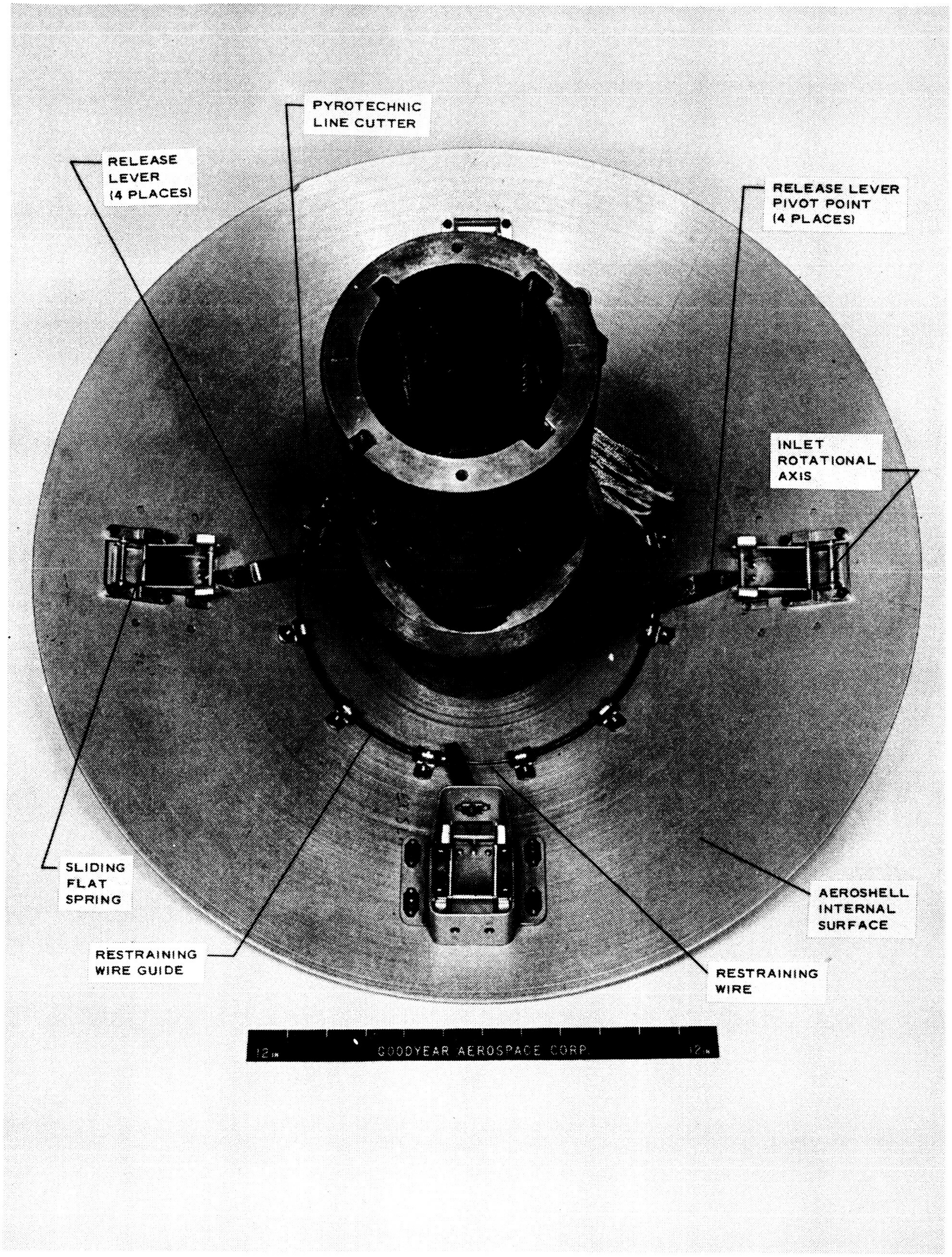

Figure 15. - Aeroshell Inlets Prior to Deployment

in Figure 15 is shown schematically in Figure 16. Figure 16 shows the inlet release spring, which is not visible in Figure 15. When the electrical pyrotechnic cutter is activated, the restraining wire is cut, permitting the inlet release spring to rotate the release levers. When the tabs rotate to the dashed position shown in Figure 15, the inlets are deployed into the airstream.

Figure 17 is a photograph of the aeroshell external surface showing the inlets in the deployed condition. The proper inlet height, as determined in Section IV, is achieved when the inlet stops contact the internal surface of the aeroshell as shown in Figure 18. A positive spring force is maintained when the inlet is in the open position to prevent the possibility of inlet flutter.

Calculations are presented in Appendix D for the (1) aerodynamic forces that an inlet spring must overcome to deploy an inlet, (2) frictional forces that an inlet release spring must overcome to release an inlet, and (3) aerodynamic forces acting on the aeroshell inlets in the open position.

Canopy Inlets

The canopy inlets, which are identical for all three models, are of the type used on the models of Figures 6 and 7. As determined in Section IV, the canopy inlets have a 1.8-in. diameter. Figure 19 shows the relative angular displacement of the canopy and aeroshell inlets. While the forward and rear inlets are not at 45 deg relative to each other, this placement should lead to satisfactory performance. If the two sets of inlets had been placed at 45 deg

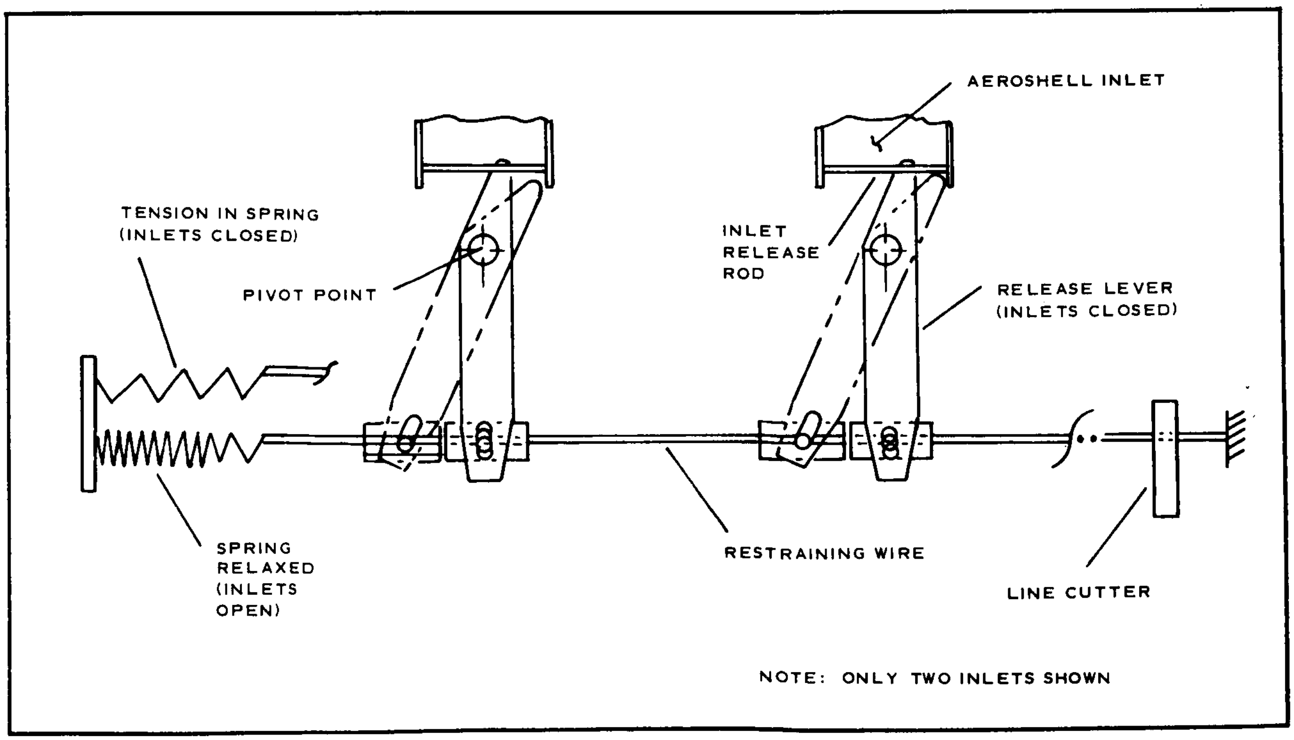

Figure 16. - Schematic of Aeroshell Inlet Restraining System

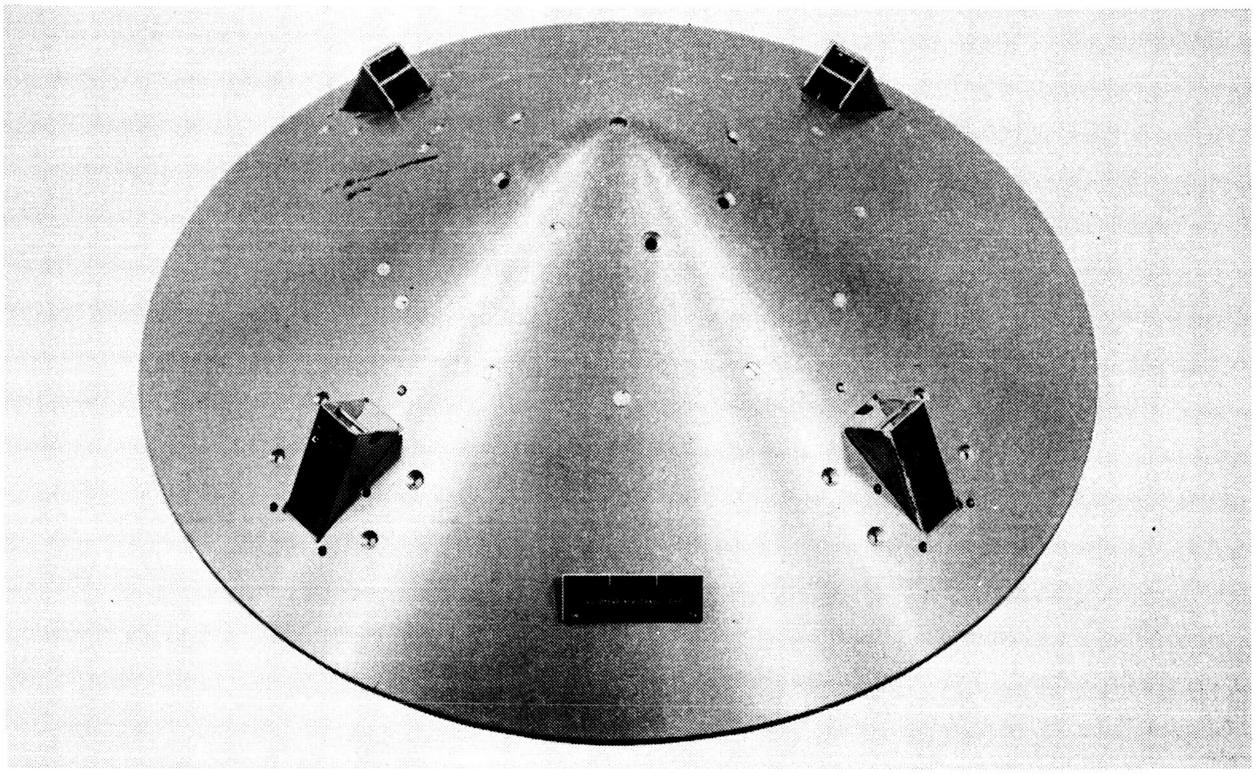

Figure 17. - Aeroshell Inlets Deployed (External View)

relative to each other, two meridional tapes would have been severed where the canopy attaches to the aeroshell inlets (see Figure 19). This latter placement then would be unacceptable from a stress standpoint.

Canopy Attachment Scheme

The forward attachment of the canopy to the hard structure of the -101 and -105 assemblies is shown in Figure 20. The canopy is clamped to the aeroshell inlet tubes as shown. Other schemes, such as a flexible fabric connection between the canopy and the inlet tubes, also were considered. However, the approach shown was adopted because of dimensional limitations and simplicity. As shown in Figure 20, the canopy will remain unrestrained in the vicinity of the aeroshell rim.

Forward attachment of the canopy for the -103 assembly was continuous at the aeroshell periphery, similar to the attachment of the models shown in Figures 6 and 7. Attachment to the simulated payload would have resulted in an undesirable displacement between the canopy and aeroshell periphery (see Figure 21) for the current canopy profile.

The rear attachment for all three models was made to the simulated payload as shown in Figure 22.

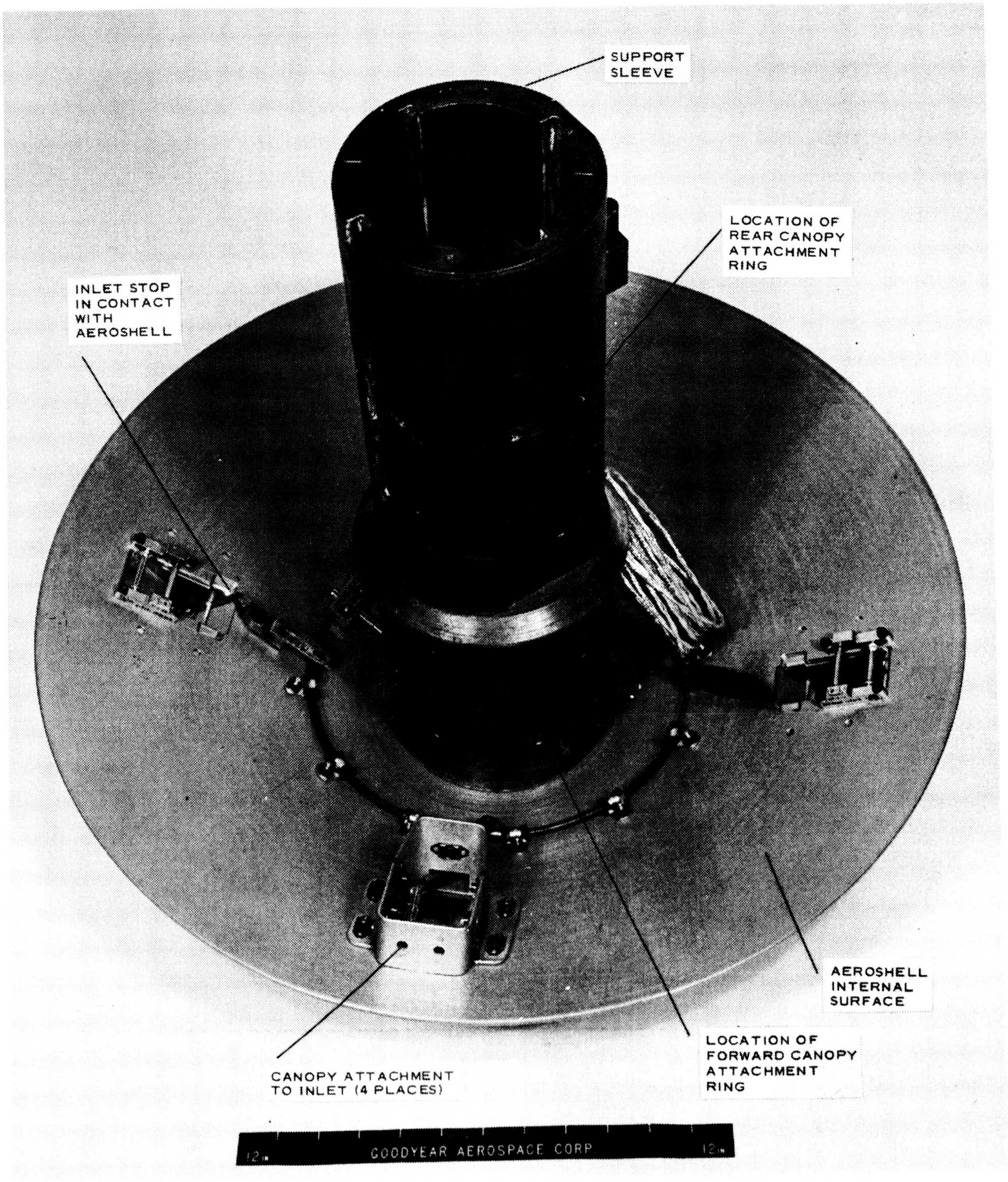

Figure 18. - Aeroshell Inlets Deployed (Internal View)

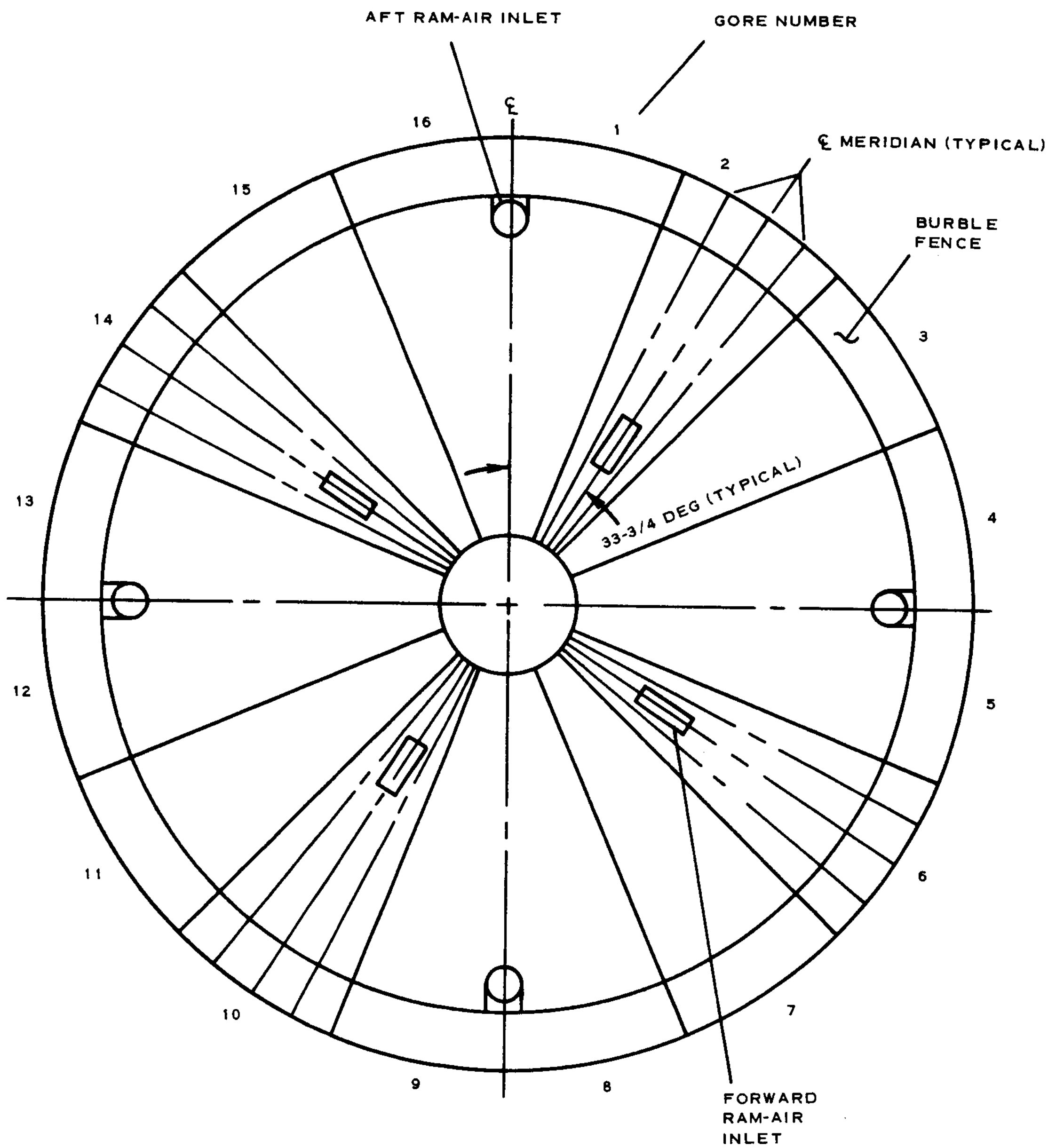

Figure 19. - Relative Angular Displacement of Inlets (Looking Downstream)

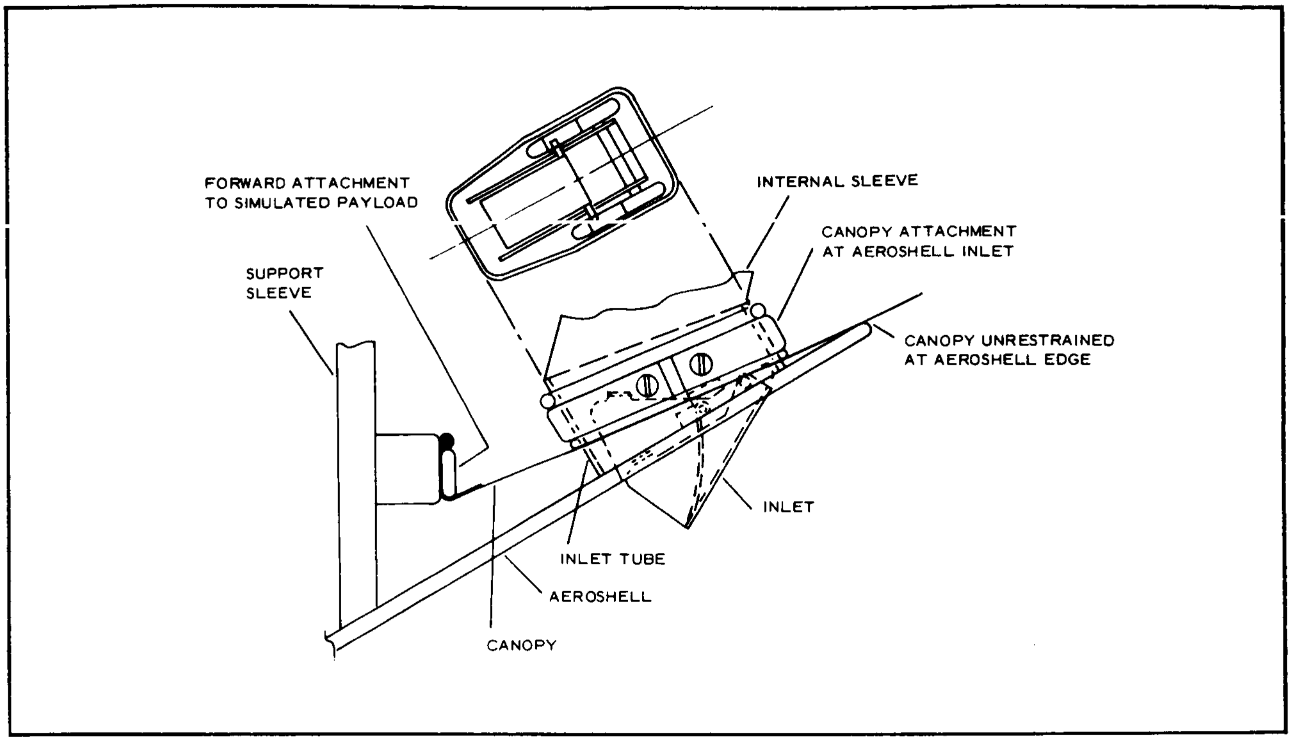

Figure 20. - Canopy Forward Attachment Scheme for -101 and -105 Models

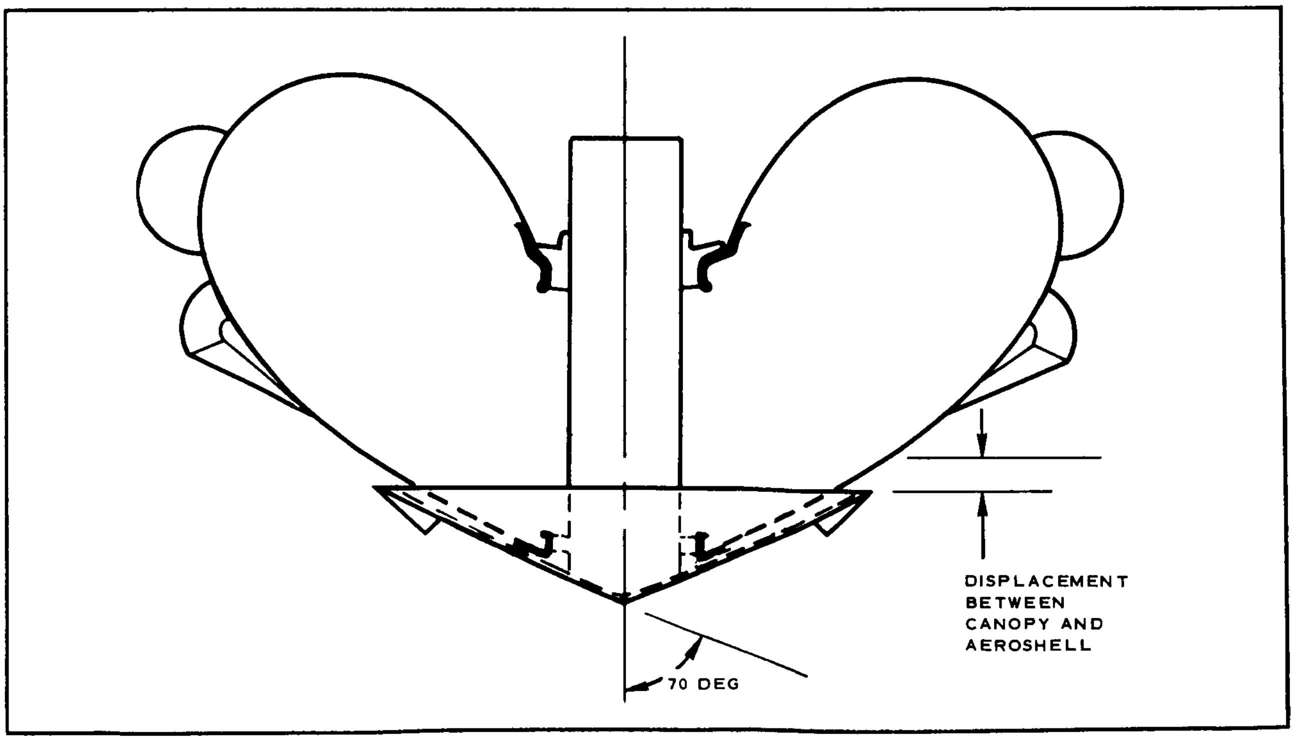

Figure 21. - Displacement between Canopy and Aeroshell Periphery

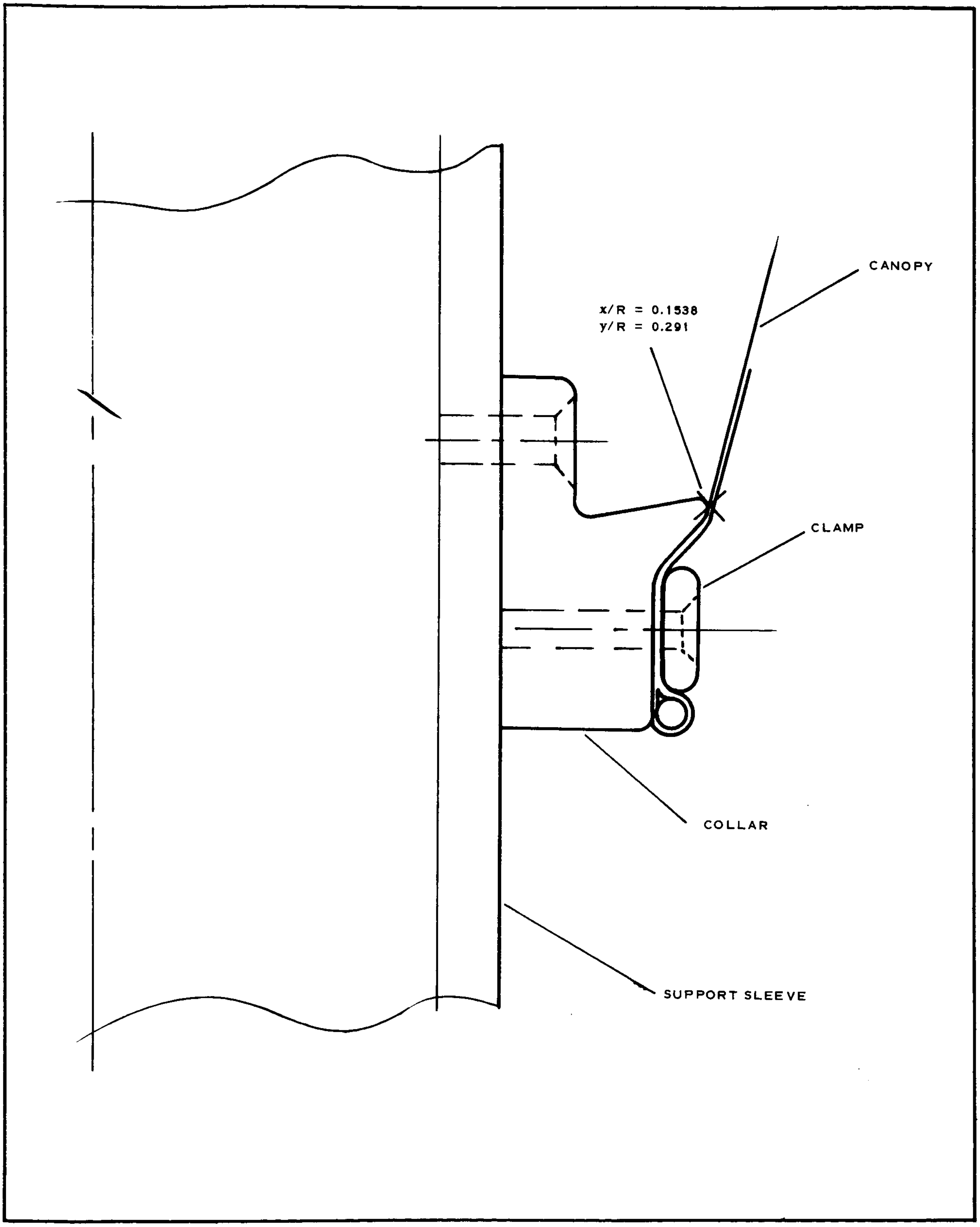

Figure 22. - Rear Attachment Scheme

Canopy Gore Pattern

While the profile of the current models, presented in Table II, is the same as the previous wind tunnel models (see Figures 6 and 7), it was necessary to modify the previous gore patterns to account for the current attachment locations. The specific equations that define the gore geometry, as derived in Reference 3, are repeated below for convenience.

$$\tan \beta = \frac{2\pi\left(\frac{x}{R}\right)}{nF} \;;$$

$$\tan \gamma = \sqrt{\frac{\sin \beta \cos \beta}{\beta}} \;;$$

$$\frac{r_g}{R} = \frac{\pi}{n \sin \beta}\left(\frac{x}{R}\right) \;;$$

$$\frac{S_g}{R} = \left(\frac{r_g}{R}\right)\beta \;;$$

$$\frac{d_g}{R} = \left(\frac{r_g}{R}\right)\left(1 - \cos \beta\right) \;;$$

$$\epsilon_{\phi} = \sqrt{2} \sin \gamma - 1 \;;$$

$$\epsilon_{\theta} = \sqrt{2} \sin \gamma - 1 \;;$$

$$f_B = F \frac{pR}{4}\left(\frac{\sin \beta}{\beta \sin^2 \gamma}\right); \quad \text{and}$$

$$\frac{f_c}{f_m} = \frac{1}{\tan^2 \gamma}$$

Table III gives the numerical values of the lobe geometry, radical growth due to unrestrained thread racking, and fabric stresses based on the preceding equations.

As shown in Figure 23, the gore patterns, as constructed, actually comprise three gores. The technique of combining three gores into one pattern to facilitate fabrication was applied successfully to the models of Figures 6 and 7. Due to fabric width limitations, a splice or cross seam in the gore pattern of the current models was necessary. The splice begins at the burble fence and proceeds to the rear postion of the pattern where less aerodynamic loading takes place. A total of 16 of the patterns shown in Figure 23, resulting in 48 actual gores, are used. Four of the 16 patterns are modified for each model to accommodate the inlet assembly as shown in Figure 23.

TABLE II. - AID COORDINATES

x/R	y/R, front surface	y/R, rear surface
1.00000000E+00	0.	0.
9.99000000E-01	3.40563513E-02	-2.35478194E-02
9.75000000E-01	1.62452220E-01	-1.15803332E-01
9.50000000E-01	2.23086659E-01	-1.59982524E-01
9.25000000E-01	2.67284617E-01	-1.91343665E-01
9.00000000E-01	3.03167273E-01	-2.15587627E-01
8.75000000E-01	3.33821811E-01	-2.34951926E-01
8.50000000E-01	3.60836801E-01	-2.50592616E-01
8.25000000E-01	3.85244206E-01	-2.63196950E-01
8.00000000E-01	4.07622681E-01	-2.73209313E-01
7.75000000E-01	4.28356524E-01	-2.80932716E-01
7.50000000E-01	4.47723896E-01	-2.86580582E-01
7.25000000E-01	4.65934253E-01	-2.90305617E-01
7.00000000E-01	4.83150325E-01	-2.92216955E-01
6.75000000E-01	4.99501793E-01	-2.92390733E-01
6.50000000E-01	5.15094220E-01	-2.90877046E-01
6.25000000E-01	5.30015103E-01	-2.87703934E-01
6.00000000E-01	5.44338105E-01	-2.82880197E-01
5.75000000E-01	5.58126106E-01	-2.76396747E-01
5.50000000E-01	5.71433447E-01	-2.68227011E-01
5.25000000E-01	5.84307618E-01	-2.58326465E-01
5.00000000E-01	5.96790546E-01	-2.46631265E-01
4.75000000E-01	6.08919603E-01	-2.33055882E-01
4.50000000E-01	6.20728396E-01	-2.17489501E-01
4.25000000E-01	6.32247084E-01	-1.99790778E-01
4.00000000E-01	6.43499407E-01	-1.79780287E-01
3.75000000E-01	6.54505351E-01	-1.57229586E-01
3.50000000E-01	6.65284423E-01	-1.31845032E-01
3.25000000E-01	6.75855781E-01	-1.03243152E-01
3.00000000E-01	6.86238304E-01	-7.09115788E-02
2.75000000E-01	6.96450654E-01	-3.41438123E-02
2.50000000E-01	7.06511337E-01	8.07752932E-03
2.25000000E-01	7.16438752E-01	5.73098813E-02
2.00000000E-01	7.26251250E-01	1.16163698E-01
1.75000000E-01	7.35967176E-01	1.89708972E-01
1.50000000E-01	7.45604921E-01	2.91079991E-01
1.25000000E-01	7.55182969E-01	0.
1.00000000E-01	7.64719940E-01	0.
7.50000000E-02	7.74234637E-01	0.
5.00000000E-02	7.83746097E-01	0.
2.50000000E-02	7.93273635E-01	0.
0.	8.02836895E-01	0.

TABLE III. - LOBE GEOMETRY, RADIAL GROWTH DUE TO UNRESTRAINED THREAD RACKING, AND FABRIC STRESSES

x/R	β		d_g/R	r_g/R	S_g/R	F_b	ν		ϵ_ϕ	ϵ_θ	f_c/f_m
	Deg	Min					Deg	Min			
0.1538*	10	55	0.00096	0.05315	0.01013	0.1050	44	39	-0.006	0.006	1.02
0.17	12	2	0.00117	0.05337	0.01121	0.1051	44	35	-0.007	0.007	1.03
0.20	14	5	0.00162	0.05380	0.01322	0.1054	44	25	-0.010	0.010	1.04
0.25	17	25	0.00251	0.05467	0.01662	0.1060	44	7	-0.016	0.015	1.06
0.30	20	38	0.00357	0.05572	0.02010	0.1067	43	43	-0.023	0.022	1.09
0.35	23	43	0.00481	0.05695	0.02357	0.1076	43	20	-0.030	0.029	1.12
0.38	25	30	0.00563	0.05777	0.02571	0.1083	43	3	-0.035	0.033	1.15
0.41	27	14	0.00650	0.05864	0.02787	0.1088	42	47	-0.039	0.038	1.17
0.4400+	28	55	0.00743	0.05956	0.03006	0.1096	42	29	-0.044	0.043	1.19
0.5102	32	38	0.00978	0.06193	0.03527						
0.6032	37	8	0.01326	0.06540	0.04239	0.1140	40	44	-0.077	0.062	1.35
0.7148	41	54	0.01791	0.07006	0.05123						
0.8264	46	4	0.02301	0.07515	0.06042	0.1229	38	6	-0.127	0.113	1.63
0.9349	49	34	0.02813	0.08044	0.06959						
0.9607	50	20	0.02956	0.08172	0.07179	0.1273	36	48	-0.152	0.131	1.79
0.9862	51	4	0.03084	0.08299	0.07397						
0.9978	51	24	0.03144	0.08360	0.07500						
1.0000	51	27	0.03154	0.08370	0.07516	0.1294	36	21	-0.163	0.139	1.85
1.0000	55	53	0.03471	0.07904	0.07709	0.1144	34	57	-0.190	0.159	2.05
0.9933	55	42	0.03433	0.07866	0.07647						
0.9608	54	49	0.03262	0.07696	0.07363	0.1145	35	4	-0.188	0.158	2.03
0.9194	53	37	0.03040	0.07473	0.06993						
0.8389	51	5	0.02624	0.07057	0.06292	0.1097	36	26	-0.160	0.138	1.84
0.7670	48	33	0.02264	0.06697	0.05675						
0.6850	45	19	0.01871	0.06304	0.04986	0.1029	38	29	-0.119	0.107	1.58
0.5885	40	59	0.01439	0.05872	0.04200						
0.4787	35	15	0.00996	0.05430	0.03341	0.0958	41	11	-0.059	0.064	1.31
0.3856	29	39	0.00668	0.05101	0.02640						
0.3000	23	53	0.00415	0.04850	0.02022	0.0914	43	19	-0.029	0.029	1.12
0.2377	19	20	0.00265	0.04698	0.01585						
0.1928	15	53	0.00176	0.04610	0.01278	0.0898	44	15	-0.012	0.013	1.05
0.1730	14	19	0.00142	0.04575	0.01143						
0.1538	12	38	0.00111	0.04603	0.01015	0.0908	44	32	-0.008	0.008	1.03

*Indicates x/R value of forward attachment point for assemblies -101 and -105.

+Indicates x/R value of forward attachment point for assembly -103.

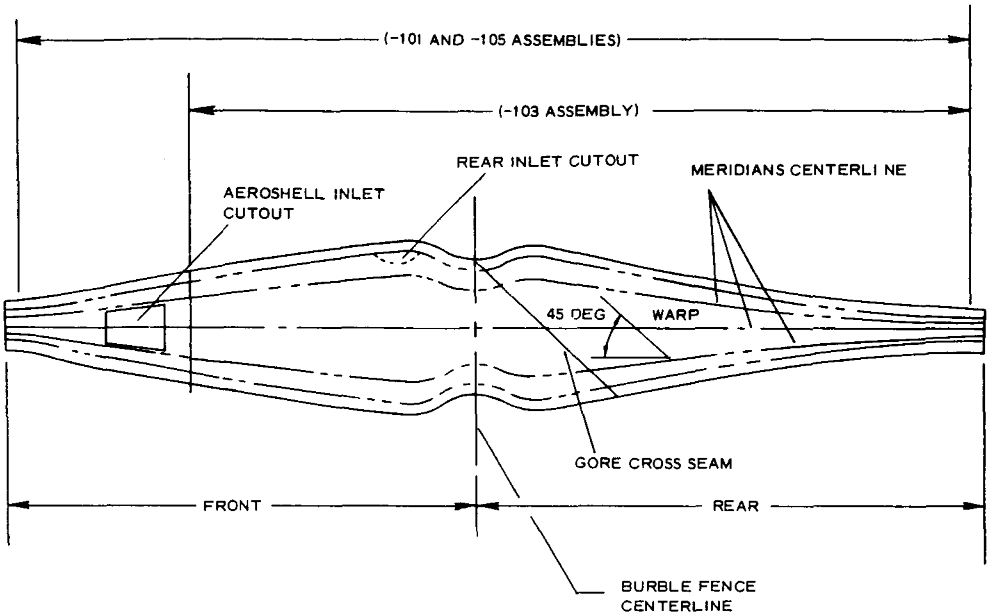

Figure 23. - Model Gore Patterns

Canopy Stowage and Release

Two methods of stowing and releasing the canopy were considered. A discussion of both is included because, depending upon interface constraints, one concept may offer advantages over the other. The first method to be discussed was the approach considered initially for the current wind-tunnel models.

This concept employed 16 small stowage loops, each of which attached to the center meridian of the individual gores. The canopy then is constrained in the packaged mode, as shown in Figure 24, by a deployment cord passing through the deployment ring and stowage loops on the meridians. The position of the stowage loops along the -103 assembly meridians would be the same since the forward attachment is continuous. However, to prevent loose canopy material in the packaged mode for the -101 and -105 assemblies, the position of the stowage loops would vary. This variation results from the interruption of the continuous attachment at the simulated payload by the attachment of the canopy at the aeroshell inlets.

The canopy may be deployed by pyrotechnically cutting the deployment cord. This permits the pressure recovery realized from the aeroshell inlets to systematically force the cut deployment cord from the stowage and deployment ring loops.

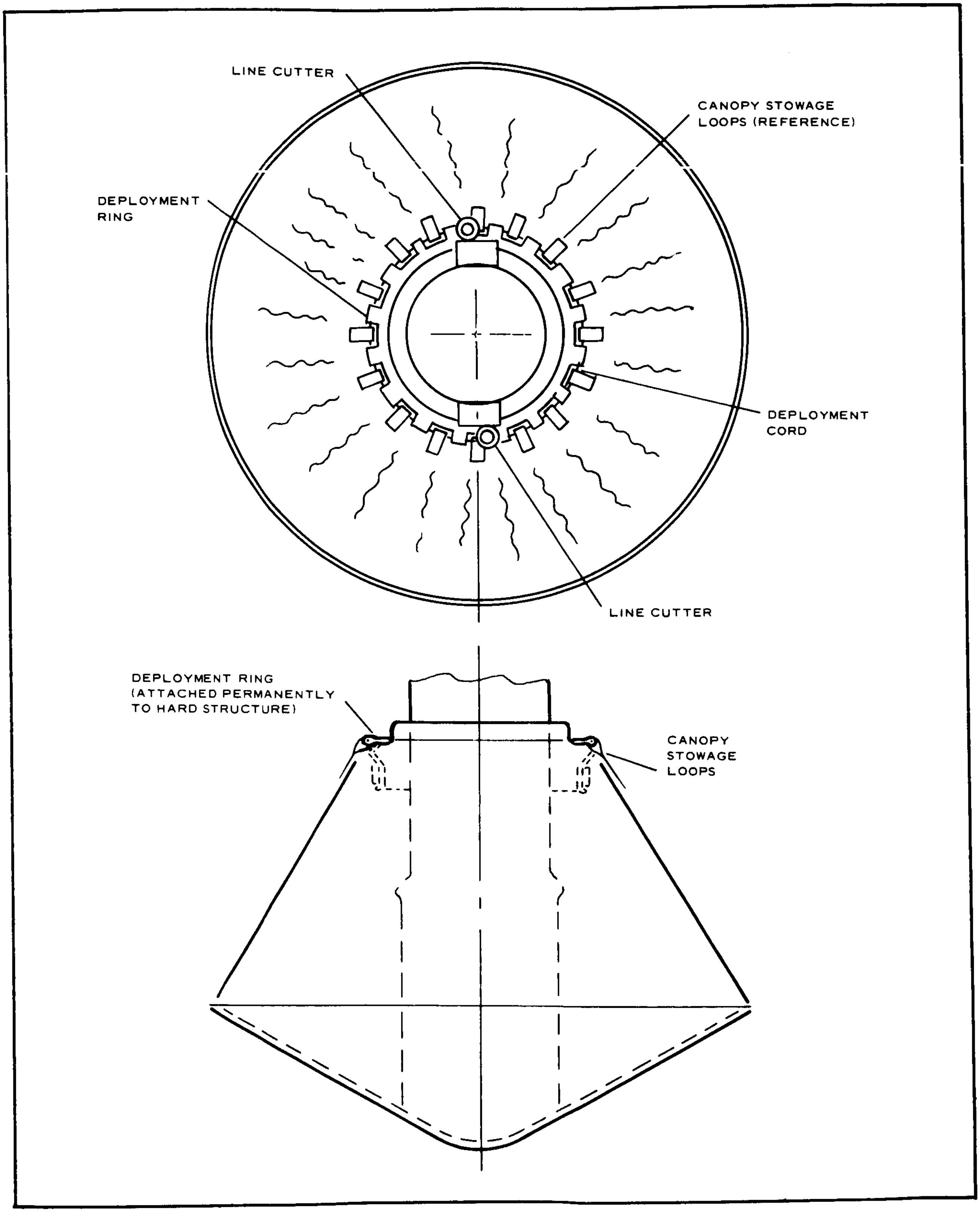

Figure 24. - Initial Stowage and Release Scheme

Though this canopy release scheme provides simplicity in design, the canopy material would be subjected to severe buffeting loads during wind tunnel start. Consequently, this scheme was discarded for the corset scheme described below.

The canopy stowage and release scheme adopted for the current models incorporates a corset to restrain the canopy prior to deployment. At deployment a flexible music wire restraining rod is extracted from loops attached to the corset by the force generated in the stretched bungee cord, permitting the corset to fall free (see Figure 25). Prior to deployment the bungee force is counteracted by a restraining cord, which is pyrotechnically cut at deployment. This cutter will be electrically sequenced with the aeroshell inlet release cutter at the wind tunnel facility so the aeroshell inlets will be released approximately 0.5 sec after release of the canopy. This delay in activating the cutters will permit the release rod sufficient time to withdraw from the corset loops.

As shown in Figure 25, the release rod is guided into the tube, which houses the bungee, to prevent the possibility of damage to the canopy by the release rod. This method of stowage and release was successfully demonstrated in an inflation test (see Section IX) conducted as part of the current program.

The sequence in which the canopy was folded prior to placing the corset in place is shown in Figure 26. The canopy folding procedure illustrated in Figure 26 was utilized on all three models. Packing of the -103 assembly was the most straightforward since the forward canopy attachment for this model was continuous at the aeroshell periphery. Packing of the -101 and -105 assemblies was more difficult due to their noncontinuous forward attachment schemes as previously described. Figure 27 shows the -103 assembly in the packaged mode.

VI. - MODEL INSTRUMENTATION

Each model was instrumented with pressure transducers, supplied by AEDC, for measuring both aeroshell inlet and canopy internal pressure-time histories. In addition, six load cells supplied by LRC were installed in each model to measure the load-time history of the meridional tapes.

The method in which the load cells were attached to the meridians is shown in Figure 28. Two load cells were installed on each of three meridional tapes per model as shown in Figure 29. The serial number and location of the load cells for the -101, -103, and -105 assemblies are presented in Figure 30.

It is expected the load cells, which are capable of measuring loads up to 180 lb, will provide good accuracy in detecting the maximum anticipated meridian load of 44.5 lb (see Appendix B).

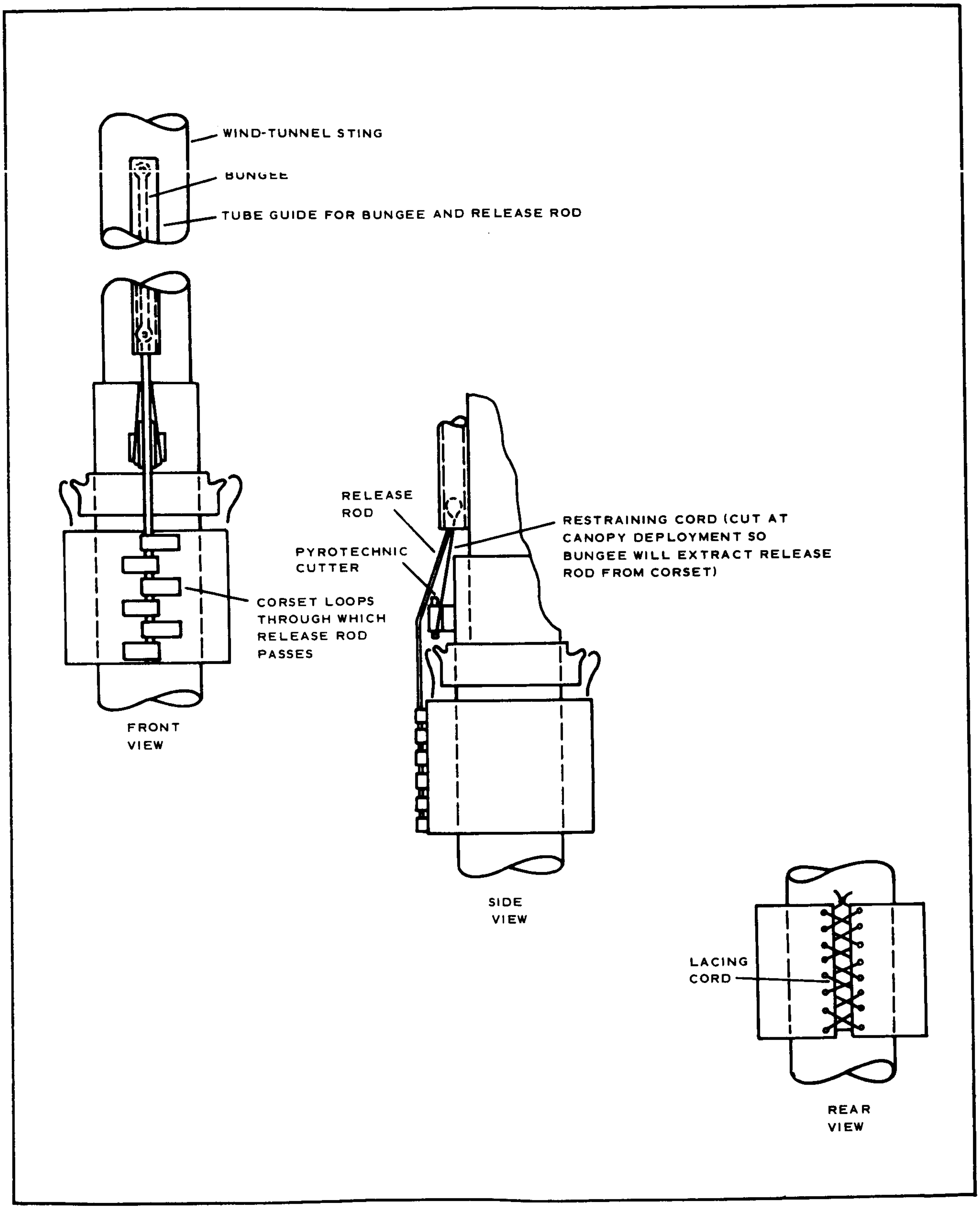

Figure 25. - Canopy Stowage and Release Scheme

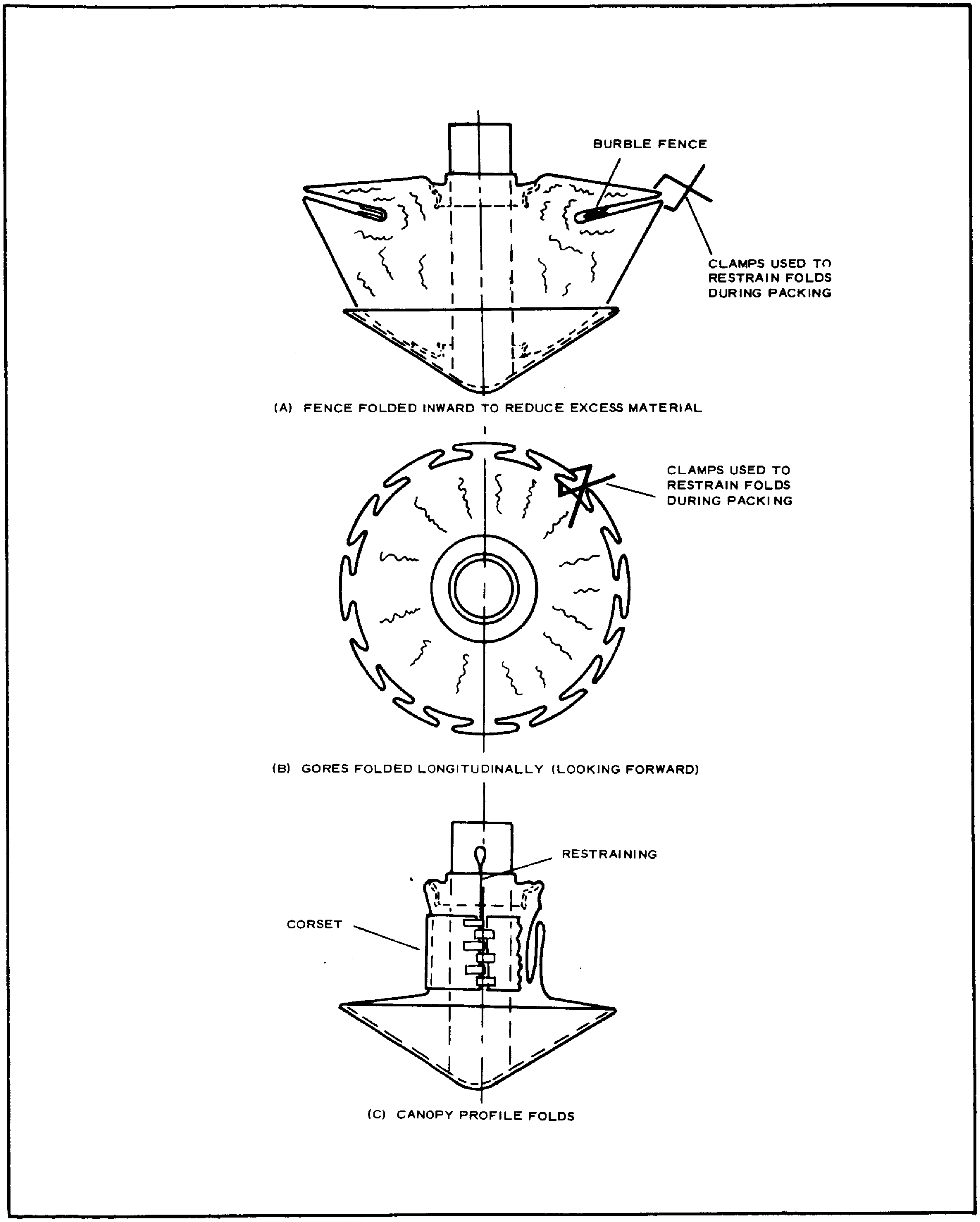

Figure 26. - Folding Sequence

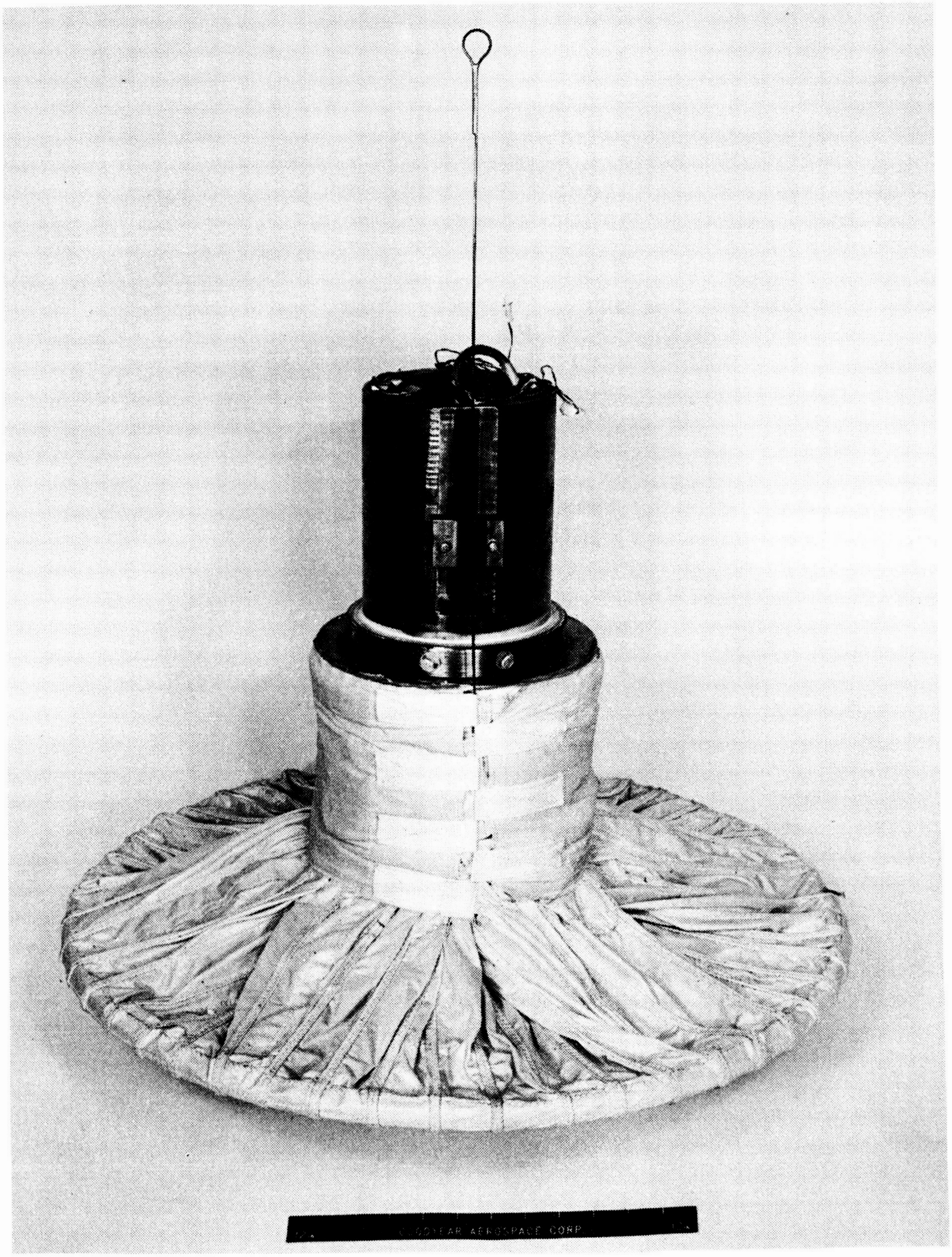

Figure 27. - AID Model in Packaged Mode

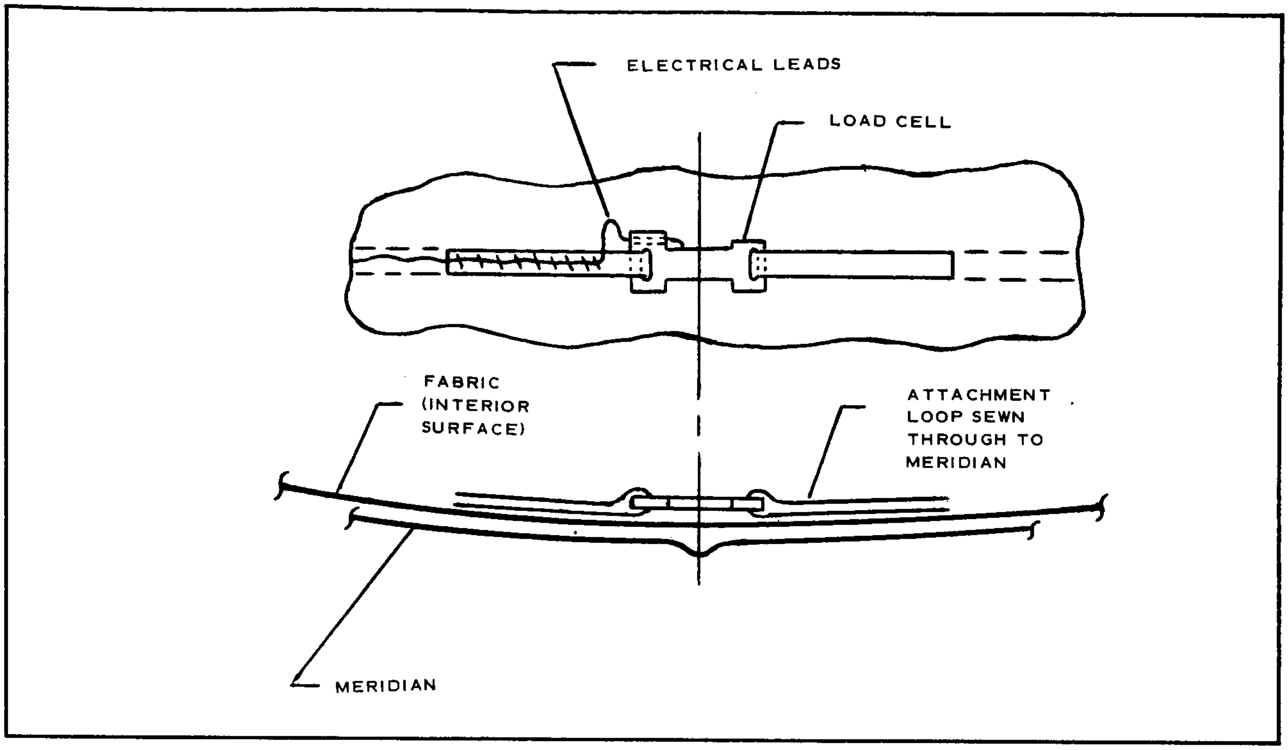

Figure 28 - Load Cell Attachment to Meridian

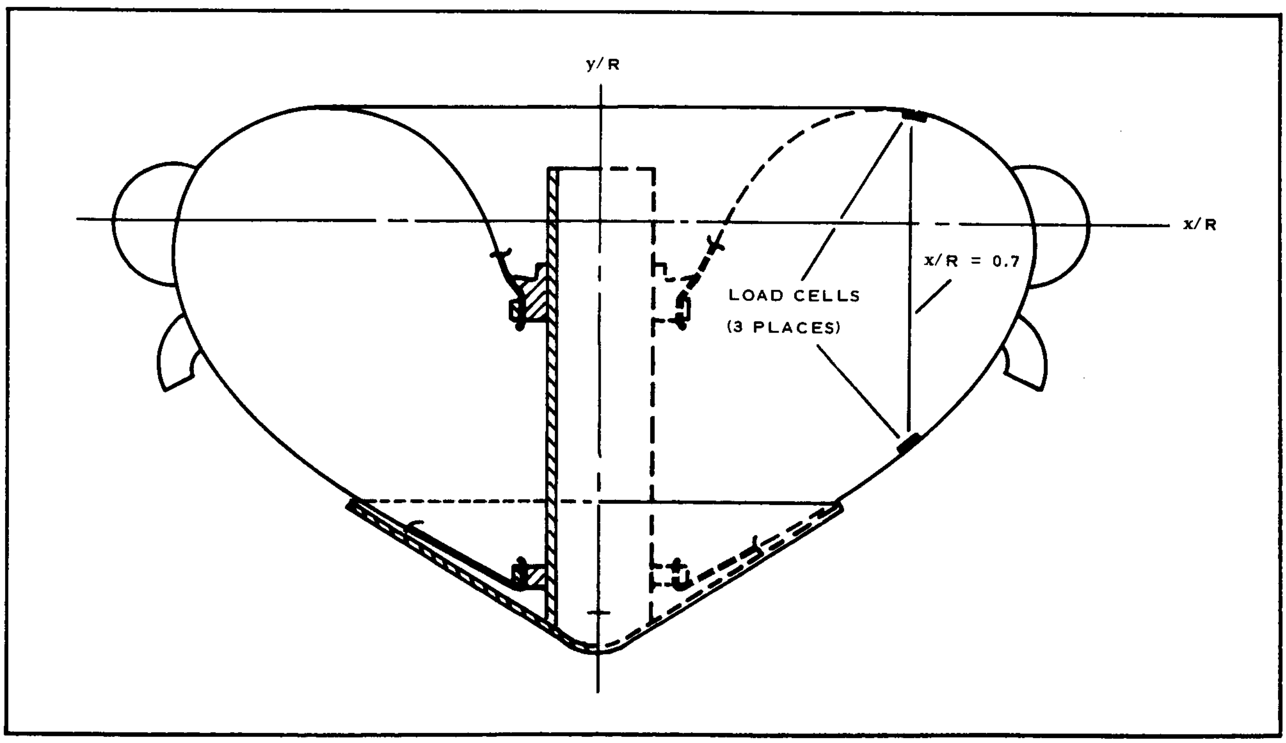

Figure 29. - Profile of AID Showing Meridional Tape Load Cell Locations

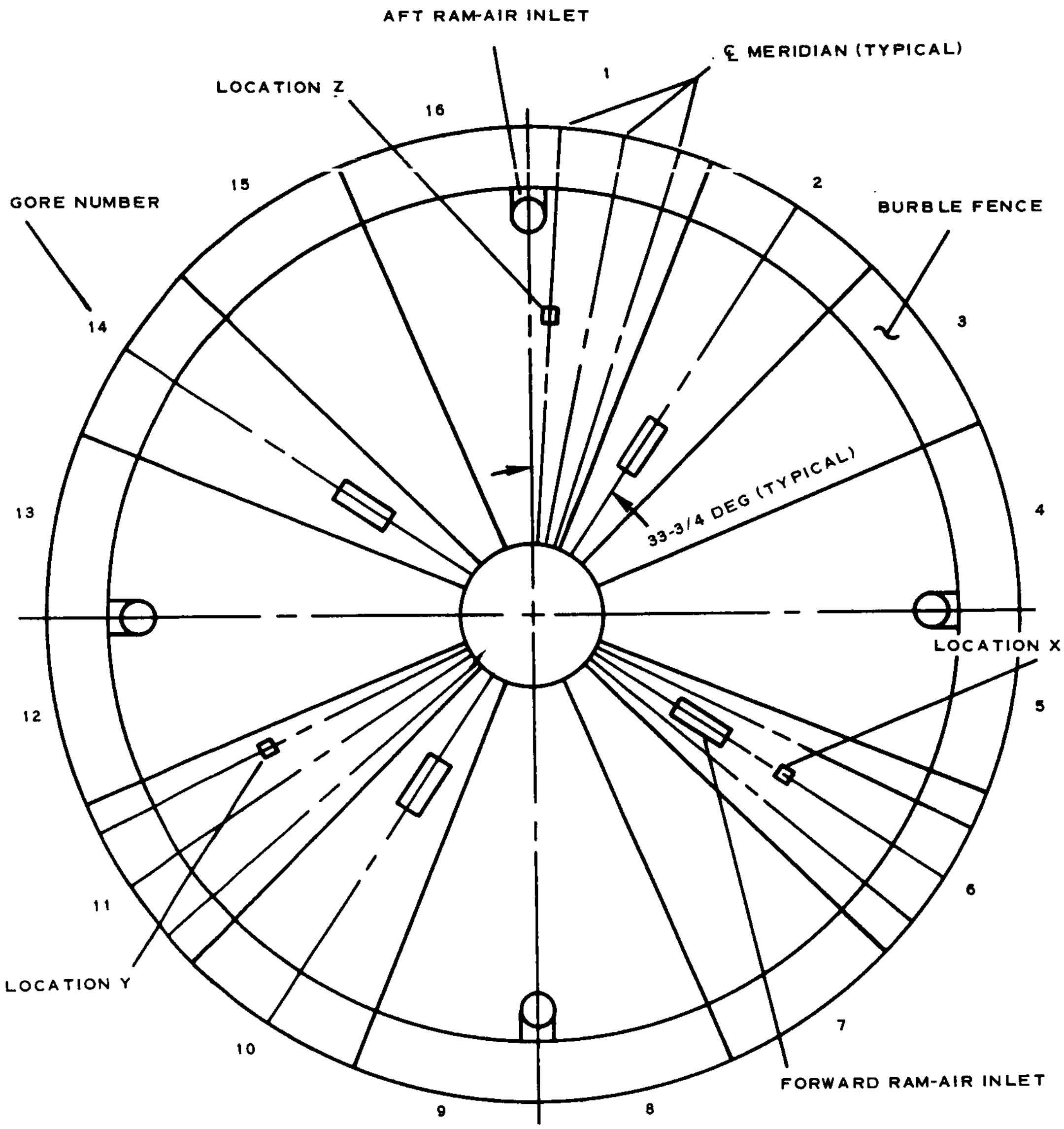

ASSEMBLY	POSITION	SERIAL NUMBER FRONT SURFACE	SERIAL NUMBER REAR SURFACE
-101	X	1	4
	Y	2	5
	Z	3	6
-103	X	7	10
	Y	8	11
	Z	9	12
-105	X	13	16
	Y	14	17
	Z	15	18

Figure 30. - Serial Numbers and Locations of Load Cells for Each Assembly

VII. - DESIGN DOCUMENTATION

The detailed engineering drawings of each AID assembly are presented in Appendix A. Table IV presents an index delineating the details and subassemblies for the three final assemblies.

TABLE IV.- INDEX TO ATTACHED INFLATABLE DECELERATOR DRAWINGS

Final assembly (645A000-003-___)	Subassemblies (645A000-___-___)	Details (645A000-___-__)
-101	-004-101, 115	-003-3, 5, 7, 9, 11, 13, 17, 19, 21
	-102-101	-116-7
	-103-103	-117-5, 7, 17, 19
	-116-101	-119-1, 7, 13
	-117-101, 103, 105, 111	
	-118-101	
	-119-103, 107, 109	
-103	-004-103, 115	-003-3, 5, 7, 9, 11, 15, 17, 19
	-102-101	-116-7
	-103-103	-117-7, 17, 19
	-116-101	-119-1, 7, 13, 47
	-117-101, 105, 107, 109, 111	
	-118-103	
	-119-105, 107, 109	
-105	-004-105, 115	-003-3, 5, 7, 9, 11, 13, 17, 19, 21
	-103-101	-116-7
	-103-103	-117-5, 7, 17, 19
	-116-101	-119-1, 7, 13
	-117-101, 103, 105, 111	
	-118-101	
	-119-103, 107, 109	

SECTION VIII - MATERIALS SELECTION

1. FABRIC

Two of the AID canopies were fabricated of Nomex and the other of Dacron. The Dacron fabric was chosen for one model because it results in a fabric ultimate load to developed load more representative of flight model design than does the Nomex fabric. The design factors for both the Nomex fabric and Dacron fabric are presented in Table V.

TABLE V. - DESIGN FACTORS

Factors	Nomex		Dacron*	
	Fabric	Meridians	Fabric	Meridians
Overload (flow breakdown)	1.50	1.50	1.00	1.00
Dynamic (flag snapping)	1.50	1.50	1.50	1.50
Temperature	1.38	1.33	1.38	1.33
Seam efficiency (see Section IX)	1.25	1.00	2.64	1.00
Racking	1.10	1.00	1.10	1.00
Safety factor	2.00	2.00	1.50	1.50
Composite design factor	8.55	6.00	9.00	3.00

*Design factors for Dacron are representative of those that would be used in a flight model design (see Reference 3).

From Appendix B the expected fabric stress, for the design conditions given in Table I of this report, is 3.09 lb/in. Thus, the ultimate room temperature material strength needed is:

$$F_{t_u} = (9.0)(3.09)$$

$$= 27.6 \text{ lb/in.}$$

The actual Dacron strength given in Section IX is 40.8 lb/in. which results in the following margin of safety:

$$(\text{M.S.}) = \frac{40.8}{27.9} - 1.0$$

$$= 0.46.$$

The actual Nomex fabric strength given in Section IX is 96.4 lb/in., which results in the following margin of safety:

$$(M.S.) = \frac{96.4}{27.9} - 1.0$$

$$= 2.45.$$

Thus, the Dacron fabric has a margin of safety which is approximately a factor of 5 less conservative than the Nomex fabric.

Meridional tapes with an ultimate strength of 548 lb, which is essentially the strength used on the previous wind-tunnel models, were used on the current models. Appendix B indicates that the actual loads in the meridians will not exceed 44.5 lb for the conditions presented in Table I of this report. By applying the flight test composite design factor of 3.0 for the meridians, the required meridian ultimate strength is

$$F_{t_u} = (3)(44.5)$$

$$= 134 \text{ lb},$$

which is well below the 548-lb strength actually used. The reason that the 548-lb strength meridians were used is because the basic isotensoid theory says that the elongations of the meridians and fabric must be the same if these two components are to carry the proportion of the total drag load predicted by the theory. A comparison of the elongations, which can be expected for the current models, is shown below. For the fabric,

$$\delta_f = \frac{F_{t_u}}{f_b}$$

$$= \frac{40.8}{3.09}$$

$$= 13.2 .$$

For the meridians,

$$\delta_m = \frac{F_{t_u}}{T_m}$$

$$= \frac{548}{44.5}$$

$$= 12.3$$

Therefore, the elongations are nearly the same, which means that the tapes and meridians will carry the proportion of the total load predicted by the isotensoid theory. This observation assumes that the stress-strain characteristics of the tapes and fabric are the same.

Both the Nomex and Dacron fabrics were calandered and coated to reduce their permeability to a level shuch that the ram-air recovered by the inlets will maintain the design shape and internal pressure. Calandering of the fabric, which is a mechanical process for reducing the fabric permeability, is accomplished by passing a heated mandrel under 85 tons of pressure over the cloth. The cloth is restrained at its perimeter to reduce shrinkage. The permeability of the fabric is then further reduced (see Section IX) by applying a coating which forms a mechanical bond with the fabric.

The Nomex fabric was coated with a Viton fluorelastomer coating that had been successfully employed in the model design of Reference 3. The Dacron fabric was coated with a single component silicone coating. Both coatings were machine applied, predirçied at 150 deg and final cured at 325 deg F.

The materials for the model hard structure were selected on the basis of meeting the AEDC wind tunnel quality control requirements and are not discussed in this report.

IX. - LABORATORY TESTING

General

Laboratory tests that were conducted include: (1) tensile tests of both the basic textile components and various seams and joints used in the decelerator construction; (2) permeability tests of both the coated and uncoated Dacron and Nomex cloths; (3) a functional evaluation of a full-scale aeroshell inlet assembly; and (4) a rapid deployment and inflation test of one of the completed AID assemblies. A discussion of the objectives and results of each of these tests is presented below.

Textile Tensile Tests

Variations in the tensile strength characteristics of different lots of textile materials woven to the same specification can occur. As a result, it is necessary to conduct tensile strength tests to determine the exact strength characteristics of the lot being used. Tensile tests were conducted for one-inch raveled strips of both the coated Nomex and Dacron fabrics in accordance with Federal Specification CCC-T-191b on a tensile testing machine. Strength tests were not conducted on the Nomex meridian tapes or on the various thread types used in the fabrication of the decelerators. These materials were taken from the same lot as the materials used in the fabrication of the models shown in Figures 6 and 7. The test results, which established the thread and tape strengths used on those models, are presented in Reference 3. However, tensile tests were conducted on the Dacron meridional tapes since previous tests had not been conducted. A summary of the results from the above tests is presented in Table VI.

Tensile tests also were performed to verify the structural integrity of the main gore seam, rear burble fence seam, and inlet seam for the Dacron canopy. The results of these tests are summarized in Table VII. Similar tests were conducted for the Nomex canopies of the model shown in Figure 6 (see Reference 3) and as a result were not repeated during this program. The structural

TABLE VI. - TENSILE STRENGTH TEST RESULTS OF CANOPY FABRIC AND MERIDIAN TAPES

Specimen	Nomex fabric ultimate load (lb/in.)	Dacron fabric ultimate load (lb/in.)	Dacron meridian tape ultimate load (lb)
Warp direction			
1	90.0	42.00	. . .
2	95.0	41.75	. . .
3	97.0	37.50	. . .
4	102.0	41.75	. . .
5	98.0	41.00	. . .
Average	96.4	40.80	. . .
Fill direction			
1	113.0	42.0	. . .
2	108.0	43.0	. . .
3	110.0	43.5	. . .
4	111.0	44.0	. . .
5	112.0	43.0	. . .
Average	110.8	43.1	. . .
1	. . .	. . .	518
2	. . .	. . .	561
3	. . .	. . .	540
Average	. . .	. . .	543

integrity of the load cell attachment to the meridians, and the forward inlet and forward attachment, also were established by tensile tests. The results of these tests are presented in Table VIII.

Fabric Permeability Tests

Results of wind-tunnel tests (see Reference 6) of AID models, similar to that shown in Figure 7, indicate that the rear surface permeability has a marked influence on the AID drag coefficients. Models tested with a high rear surface permeability (10 cu ft/min-sq ft at 0.5 in. of water pressure) had a drag coefficient on the order of 60 percent of that of the low permeability model (0.02 cu ft/min-sq ft at 0.5 in. of water pressure).

To obtain the high pressure recovery needed to produce the design shape and design drag coefficient, both the Nomex and Dacron canopies were calendered and coated to reduce their permeability levels. Permeability tests were conducted on the Nomex and Dacron fabrics before and after calendering and after coating. The results of these tests are presented in Table IX.

TABLE VII. - TENSILE STRENGTH TEST RESULTS OF DACRON CANOPY SEAMS

Item	Specimen	Ultimate load (lb/in.)
Main gore seam	1	15.0
	2	15.0
	3	17.0
	4	15.5
	5	15.0
	Average	15.5
Inlet gore seam	1	16.0
	2	16.0
	3	15.0
	4	19.0
	5	21.0
	Average	17.4
Upper burble fence seam	1	19.5
	2	20.0
	3	19.5
	4	19.5
	5	19.2
	Average	19.5
Lower burble fence seam	1	21.0
	2	18.5
	3	21.0
	4	21.5
	5	20.2
	Average	20.5

TABLE VIII. - TENSILE STRENGTH TEST RESULTS OF LOAD CELL ATTACHMENTS AND CANOPY FORWARD ATTACHMENTS

Specimen	Ultimate load (lb)
Load cell attachment	
Nomex	450
Dacron	425
Nomex	422
Canopy forward attachments	
Nomex	468 (average of 3 tests)
Dacron	464 (average of 3 tests)

TABLE IX. - FABRIC PERMEABILITY TEST RESULTS

Specimen	Permeability
Dacron (before calendering)	335 cu ft/sq ft/min at 0.5 in. of H_2O
Dacron (after calendering)	18 cu ft/sq ft/min at 0.5 in. of H_2O
Dacron (after calendering and coating)	0.21×10^{-3} cu ft/sq ft/min at 1.0 in. of H_2O
Nomex (after calendering and coating)	0.21×10^{-3} cu ft/sq ft/min at 1.0 in. of H_2O

Aeroshell Inlet Model Evaluation Tests

A functional model of an aeroshell inlet was fabricated for evaluation testing. The model was constructed of the materials to be used in the actual wind-tunnel assemblies. The following points were investigated during the model evaluation: (1) effect of fabrication tolerances on inlet functioning; (2) magnitude of friction force created between the inlet release lever and the inlet release rod; and (3) susceptibility of the inlet sliding spring to fatigue.

Tests were conducted with pressure loads on the inlet exceeding these anticipated in the wind tunnel tests (see Appendix D) to demonstrate the inlet release mechanism. The force on the inlet release spring (Figure 16) was always sufficient to overcome the friction force from the inlet release rod. Also, approximately 200 deployments were made with the model to determine if the sliding flat spring was susceptible to fatigue. Additionally, the time period that the wind-tunnel models will be stored, with the inlets in the closed position prior to testing, was duplicated with the inlet model. Again several deployments were performed without signs of fatigue in the sliding flat spring.

Deployment and Inflation Test

The -101 assembly was successfully inflation deployed in an environmental chamber at 20 psfa, 103,000 ft pressure altitude, and at approximately 162 F. Inflation was initiated by vaporization of a water-alcohol mixture contained in a reservoir within the packaged company. The primary objectives of the test were to demonstrate the adequacy of the packing, deployment, and inflation characteristics of the model. Additionally, load cells attached to the model (see Figure 30) provided an indication of the loads imposed on the meridians during deployment. Figure 31 shows the inflation test setup.

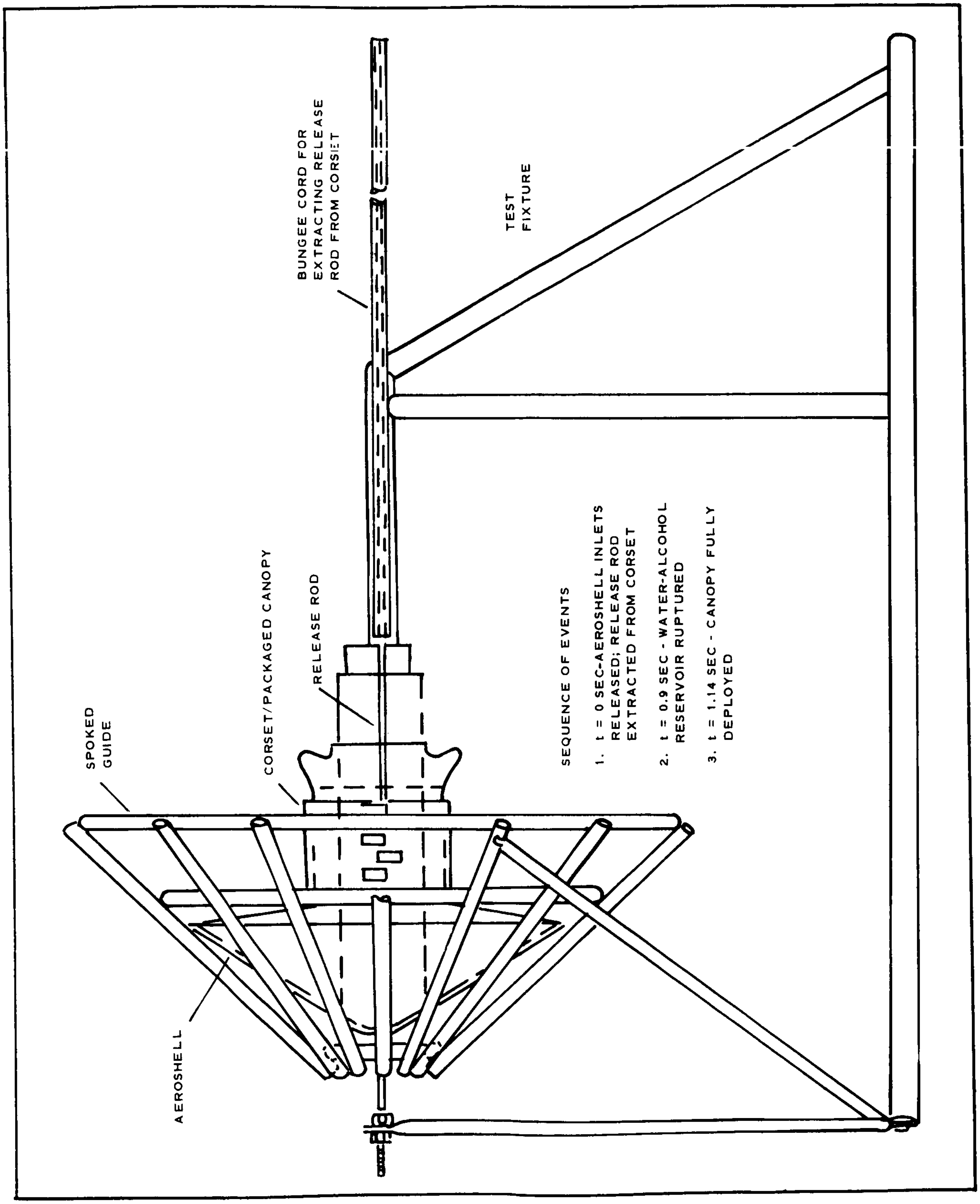

Figure 31. - Water-Alcohol Inflation Test Setup

The spoked guide serves to cradle the AID when inflated since the absence of aerodynamic forces would otherwise cause large deformations from the design shape. (See Reference 3.)

The differential pressure-time history of the AID during deployment of the canopy is shown in Figure 32. A pressure-time history for a similar test of the model in Figure 6 is shown for reference purposes. Full inflation of the canopy occurred in approximately 0.24 sec and the desired differential pressure of 1.0 psi essentially was obtained as indicated.

Load cell force-history for three load cells are shown in Figure 33. Load cells 4, 5, and 6 on the rear surface meridians were inoperative during this deployment. The peak load occurs just prior to full inflation and is slightly less than the calculated meridian tape load at that pressure. (See Appendix B).

Figure 34 is a photograph of the AID model shortly after inflation to the fully inflated shape. A review of the film coverage of the test indicated that the packing and deployment scheme was suitable for use in the wind tunnel.

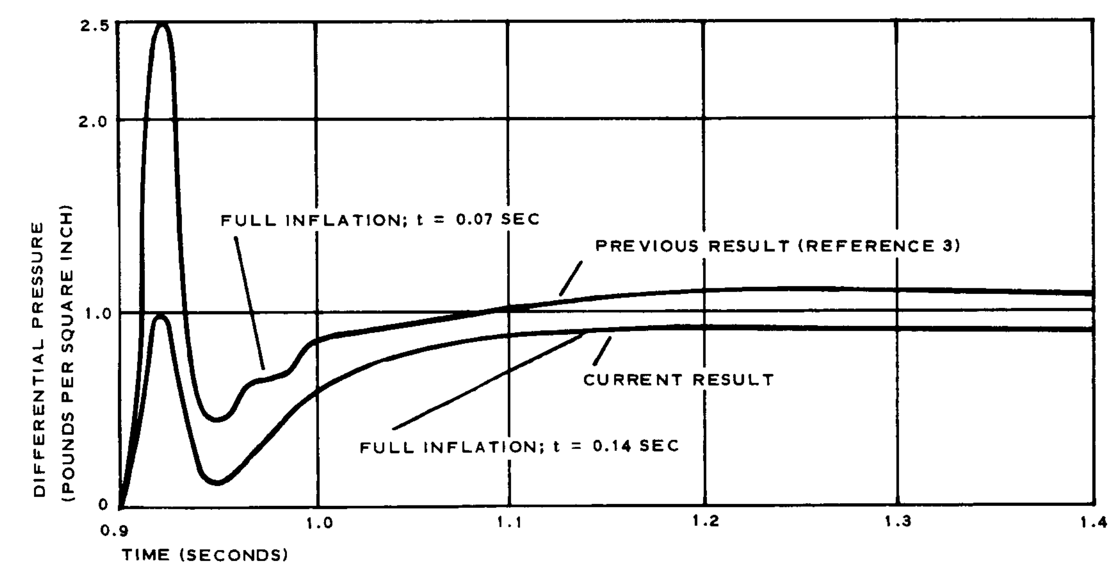

Figure 32. - AID Differential Pressure-Time History

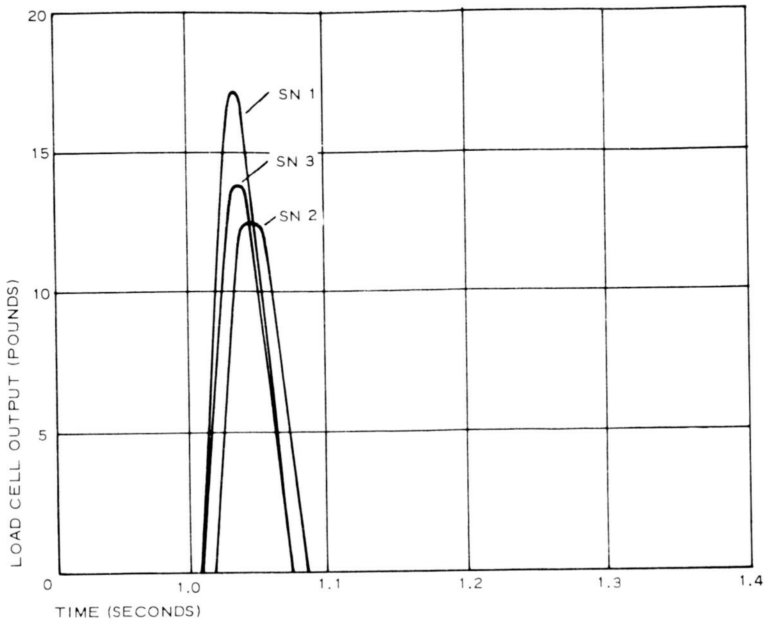

Figure 33.- Load Cell Force-Time History

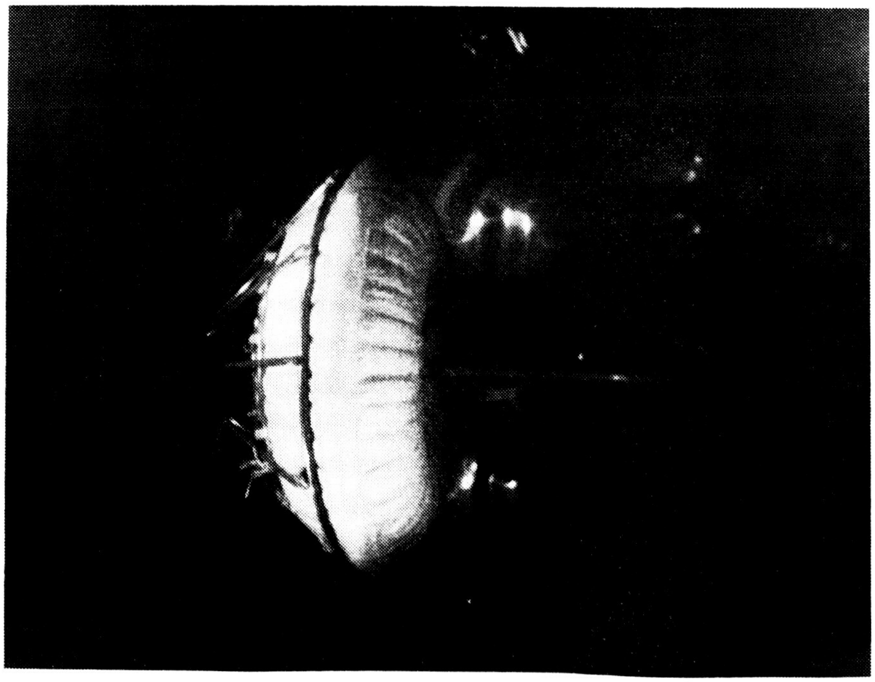

Figure 34. - Fully Inflated AID

X. - CONCLUSIONS AND RECOMMENDATIONS

Conclusions

Three attached inflatable decelerator models have been designed and fabricated for supersonic wind tunnel evaluation. The models incorporate four quick-release aeroshell inlets to accomplish deployment and four canopy inlets to effect final canopy pressurization. The following conclusions can be drawn:

1. AID models have been designed and fabricated which deminstrate alternate attachment schemes of the canopy to the aeroshell and payload.

2. An alternate means of ram-air deployment of the AID, by use of aeroshell inlets, has been developed.

3. A rapid inflation test demonstrated the workability of the AID model's inlet release system and packaging and deployment system.

APPENDIX A - DETAILED DESIGN DRAWINGS

This Appendix presents the detailed design drawings used in the manufacture of the AID assemblies. Only those drawings that differ significantly from those of Reference 3 have been included.

NOTES:

IDENTIFY PER MIL-STD-130 (GAC PROCESS SPEC J2)

2 DRESS AEROSHELL TOOLING HOLE AND SCREW HEADS WITH DOW CORNING RTV 140 MIXED WITH 1 PART IN 10 OF ALUMINUM POWER. PRIME ALUMINUM SURFACE WITH DOW CORNING A-4094 PRIMER

3 POT OR BEAD CANOPY END BANDS, TRANSDUCER, CUTTERS & FAIRING WITH DOW CORNING RTV-731 ADESIVE. WHEN USING RTV-731 ON METAL, PRIME AREA WITH DOW CORNING A-4094 PRIMER

4 TORQUE WITH MS33750 DRIVER, RECESS No 1, TO IN. LBS.

5 TORQUE WITH MS33750 DRIVER, RECESS No 3, TO 20 IN LBS.

6 TORQUE WITH MS33750 DRIVER, RECESS NO 4, TO 40 IN LBS.

7 TORQUE WITH MS33750 DRIVER, RECESS No 5, TO IN LBS.

8 INSTALL INSERT PER MIL-SPEC MS33646 (GAC PROCESS SPEC M69)

9 DECELERATOR/CLAMP LOCATION & ASSY PROCEDURE FOR -103 ASSY

A. LOCATE END BAND SNUG AGAINST CLAMP RADIUS AS SHOWN ON SH 3, -103 ASSY

B. REFERENCE TO SHEET 5, SECTION D-D, TO INSURE CORRECT POSITIONING OF CANOPY ON AEROSHELL, LOCATE ℄ OF A MERIDIAN (ON THE ℄ OF A GORE) WITH ℄ OF AN AEROSHELL INLET SUCH THAT AFT CANOPY INLET LOCATED 33 3/4 (OR 1 1/2 GORES) FROM THAT REFERENCE MERIDIAN.

C. SCRIB OR MARK FABRIC THRU CLAMP RETAINING HOLES, REMOVE & PUNCH 9/32 (.281) DIA HOLES THRU FABRIC.

D. BOND DECELERATOR WITH ELASTOMER TO CLAMP ASSY, USING AERO SHELL AS TEMPORARY CLAMP (TREAT AEROSHELL CLAMPING SURFACE WITH A SEPARATION AGENT TO PREVENT BONDING OF THIS SURFACE)

10 POT TUBES AND WIRES IN INTERIOR SLOTS WITH G.E. RTV 8112. PRIME METAL SURFACES WITH G.E. SS-4004 PRIMER

11 TWIST & WELD ENDS OF THERMOCOUPLE WIRE TO ENSURE GOOD CONDUCTIVE CONNECTION & BOND TO AEROSHELL LOCATION AS SHOWN WITH EPOXY ADHESIVE. W.T. BEAM CO. TYPE RTC

12. ALL "X" DIMENSIONS SHOWN ON DRAWINGS (-101, -103 & -105 ASSY) ARE REFERENCED FROM X=0.00

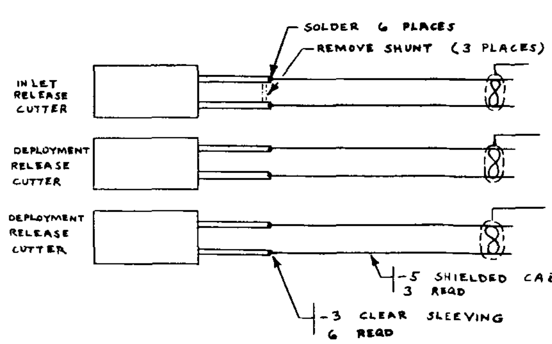

210918 LINE CUTTER SCHEMATIC

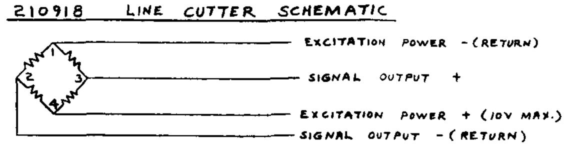

CEC 4-316 PRESSURE TRANDUCER & 4-019 ADAPTER

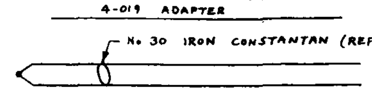

11 THERMOCOUPLE WIRE

-105	-103	-101 QTY REQD	CODE IDENT NO.	PART OR IDENTIFYING NO.	NOMENCLATURE OR DESCRIPTION	MATERIAL AND SIZE	ZONE	ITEM OR FIND NO.
1	1	1		-19	DOOR RELEASE WIRE	.055 DIA x 3 FT LG MUSIC WIRE MIL-W-470	6A5 4A4	
1	1	1		-17	WIRE RELEASE CORD	NYLON CORD MIL-C-7515 TYPE II 750LB. TEN. x 3 FT LG	8F2 6G3	
	1			-15 (DETAIL ON SH 4)	CORSET WIRE RELEASE	.067 DIA x 30.0 LG MIL-W-470 MUSIC WIRE	6H3	
1		1		-13 (DETAIL ON SH 4)	CORSET WIRE RELEASE	.067 DIA x 30.0 LG MIL-W-470 MUSIC WIRE	8F2	
4	4	4		-11	PIN - SPRING	.080 DIA x 1.75 LG MIL-W-470 MUSIC WIRE	D24	
	1			MS35338-43	LOCK WASHER			
2	2	2		AN507-832R16	SCREW			
1	1	1		TYPE 4-316 TYPE 4-019	PRESSURE TRANSDUCER & ADAPTER	SUPPLIED BY AEDC (ARNOLD ENGINEERING DEVELOPMENT CENTER	7E5 8C3	
1	1	1		No 30 IRON-CONSTANTAN TYPE No 30-50-4	THERMOCOUPLE WIRE	60 FT (720.0 IN.) LEEDS & NORTHRUP, PHILA. PA.	6G2	
1	1	1		-9	VITON TUBING	.18 I.D. x .31 O.D. x 12 FT. (144.00 IN.)	7G2	
1	1	1		-7	VITON TUBING	.06 I.D. x .18 O.D. x 12 FT. (144.0 IN.)	6G2	
3	3	3		-5	CABLE, SHIELDED	MIL-W-16878/4A, TYPE E, TWO CONDUCTOR 20 GAGE, BLK & WHITE 12 FT. (144.0 IN.)	7B1	
6	6	6		-3	SLEEVING - CLEAR (VINYL PLASTIC TUBING)	MIL-I-7444B TYPE I AWG No 10	7B1	
2	2	2		210918	REEFING LINE CUTTER	TECHNICAL ORDNANCE, INC MINNEAPOLIS, MINNESOTA	5E2	
1	1	1		LE-055D-9	SPRING	LEE SPRING CO. BROOKLYN, N.Y.	5A5 3B4	
4	4	4		SS-250-250N	SHOULDER SCREW	JERGENS TOOL SPECIALTY CO. CLEVELAND, OHIO	4H4	
1		1		-21	TUBE	3/16 x .035 WALL 1020 STEEL	4A4	
1	1	1		MS21042-3	NUT			
2	2	2		MS35338-42	LOCK WASHER			
2	2	2		AN515-8R16	SCREW			
1	1	1		AN520-10R6	SCREW			
AS REQD	AS REQD	AS REQD		RTV-173	ADESIVE SEALANT	DOW-CORNING MIDLAND, MICH		
AS REQD	AS REQD	AS REQD		RTV-140		DOW-CORNING MIDLAND, MICH		
4				SIZE 6	CORD (18.0 LG)	DACRON - NATURAL V-T-285, TYPE I, CLASS II		
		4		SIZE 6	CORD (18.0 LG)	NOMEX - NATURAL SIMILAR TO V-T-295 TYPE I OR II, CLASS I		
2	2	2		NAS679A08	NUT			
	4			AN507-632R9	SCREW			
1	1	1		AN507-1032R14				
4	4	4		AN960-8	WASHER			
16	16	16		AN960-4	WASHER			
11	6	11		AN960-10L	WASHER			
16	16	16		MS21209F5-20	INSERT - LOCK			
	8			MS21209F4-20	INSERT - LOCK			
9	5	9		AN960-10	WASHER			
	4			NAS620-6	WASHER			
	4			NAS679A06	NUT			
15	6	15		NAS679A3	NUT			
16	16	16		NAS679A04	NUT			
16	16	16		NAS1219-04-12	SCREW			
8		8		NAS1219-5-28	SCREW			
8	8	8		NAS1219-5-17	SCREW			
32	48	32		NAS1219-4-14	SCREW			
8	8	8		NAS1219-4-12	SCREW			
54	46	54		NAS1219-3-10	SCREW			

PARTS LIST

-105	-103	-101 QTY REQD	CODE IDENT NO.	PART OR IDENTIFYING NO.	NOMENCLATURE OR DESCRIPTION	MATERIAL AND SIZE	ZONE	ITEM OR FIND NO.
	1			NAS43DD3-14	SPACER		3D5	
1	1	1		645A000-117-111	LINE CUTTER CLAMP ASSY		3E2 5D2	
1	1	1		610A000-102-101	SUPPORT ASSY		8C2	
1	1	1		645A000-103-103	MODEL BALANCE PIN		5H2	
	3			645A000-119-47	TUBE		5D5	
11	6	11		MS21919WDG6	CLAMP		3G4	
1	1	1		MS21919WDG16	CLAMP		7E5 8B3	
1	1	1		645A000-119-109	WIRE CLAMP ASSY		3A4	
4	4	4		645A000-119-107	WIRE CLAMP ASSY		4H4	
	1			645A000-119-105	COVER		5D5	
1		1		645A000-119-103	COVER		3F4	
3		3		645A000-119-7	TUBE		4G4	
4	4	4		645A000-119-1	SWIVEL ARM		4H4	
1	1	1		645A000-004-115	CORSET ASSY		3C2 5C3	
	1			645A000-118-103	AEROSHELL		8A2	
1		1		645A000-118-101	AEROSHELL		3B2	
4	4	4		645A000-117-19	CLAMP		3B2 3B3	
4	4	4		645A000-117-17	CLAMP		3B2 3B3	
1	1	1		645A000-117-7	CLAMP		8C3 8D2	
1		1		645A000-117-5	CLAMP		8B2	
	1			645A000-117-109	COLLAR ASSY		8C3	
	1			645A000-117-107	CLAMP ASSY		3B3	
4	4	4		645A000-117-105	TUBE ASSY		3D4	
1		1		645A000-117-103	COLLAR ASSY		8C2	
1	1	1		645A000-117-101	COLLAR ASSY		8C2	
1	1	1		645A000-119-13	CUTTER CLAMP		2B4	
8	8	8		645A000-116-7	RETAINER		3E4	
4	4	4		645A000-116-101	SCOOP ASSY		3C4	
1				645A000-004-105	DECELERATOR ASSY		2C2	
	1			645A000-004-103	DECELERATOR ASSY		2C3	
		1		645A000-004-101	DECELERATOR ASSY		2C2	
X				-105	MODEL ASSY	DACRON DECELERATOR ATTACHED TO 120° AEROSHELL	SH 2	
	X			-103	MODEL ASSY	NOMEX DECELERATOR ATTACHED TO 140° AEROSHELL	SH 3	
		X		-101	MODEL ASSY	NOMEX DECELERATOR ATTACHED TO 120° AEROSHELL	SH 2	

PARTS LIST

Figure A-1- Model Assembly with 60-In. Dp (Drawing 645A000-003, Sheet 1)

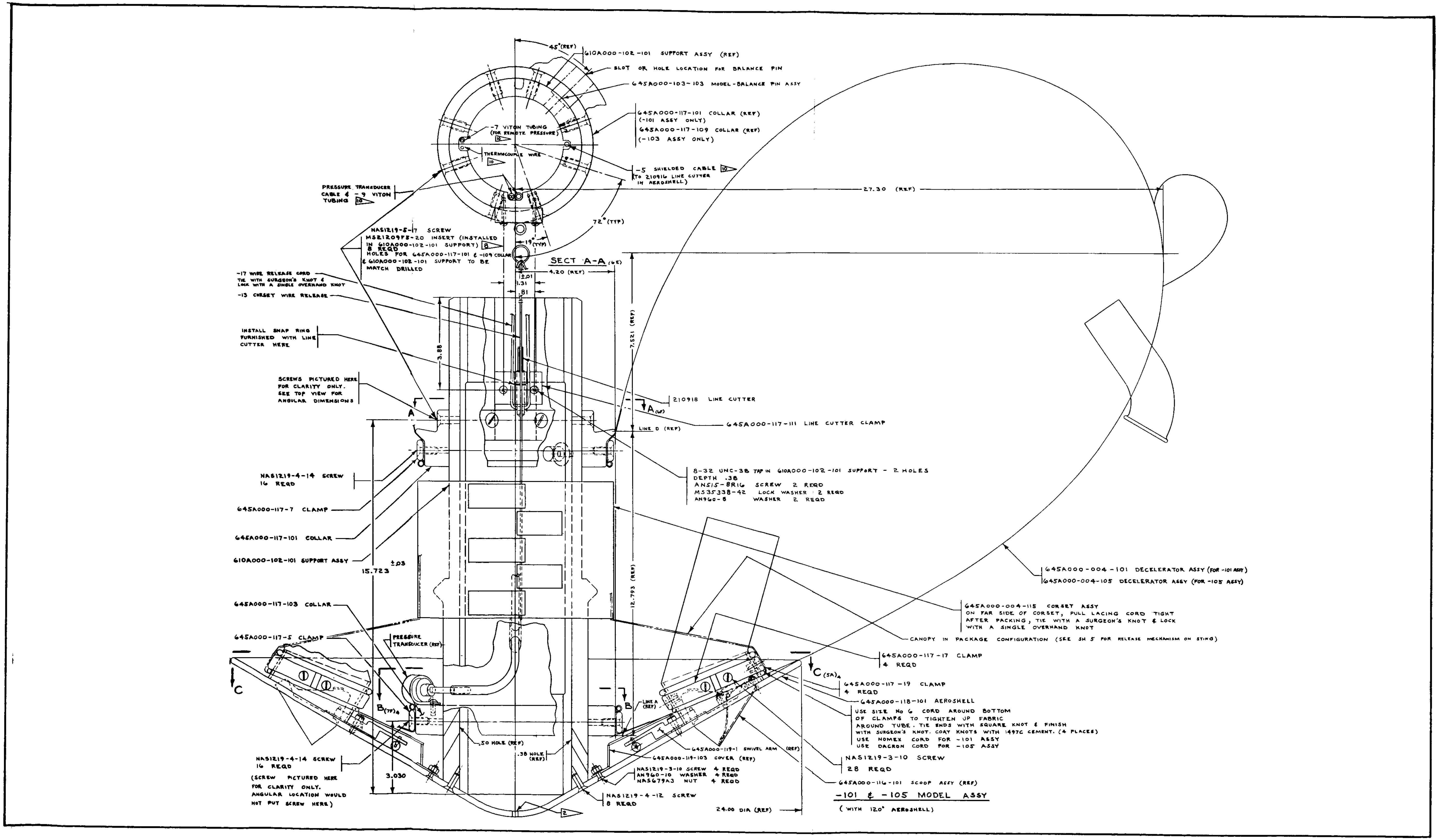

Figure A-2 · Model Assembly with 60-In. Dp (Sheet 2)

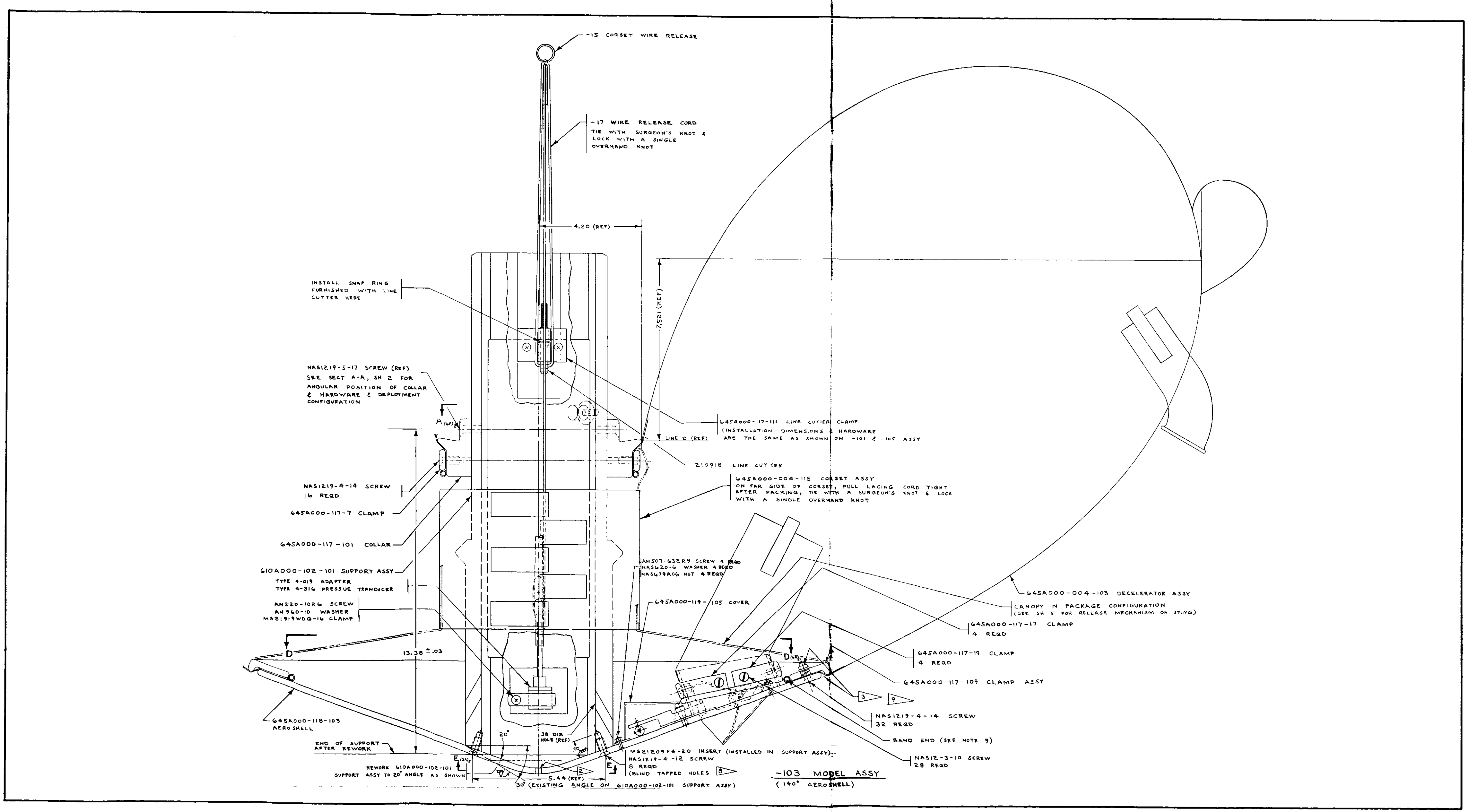

Figure A-3 - Model Assembly with 60-In. Dp (Sheet 3)

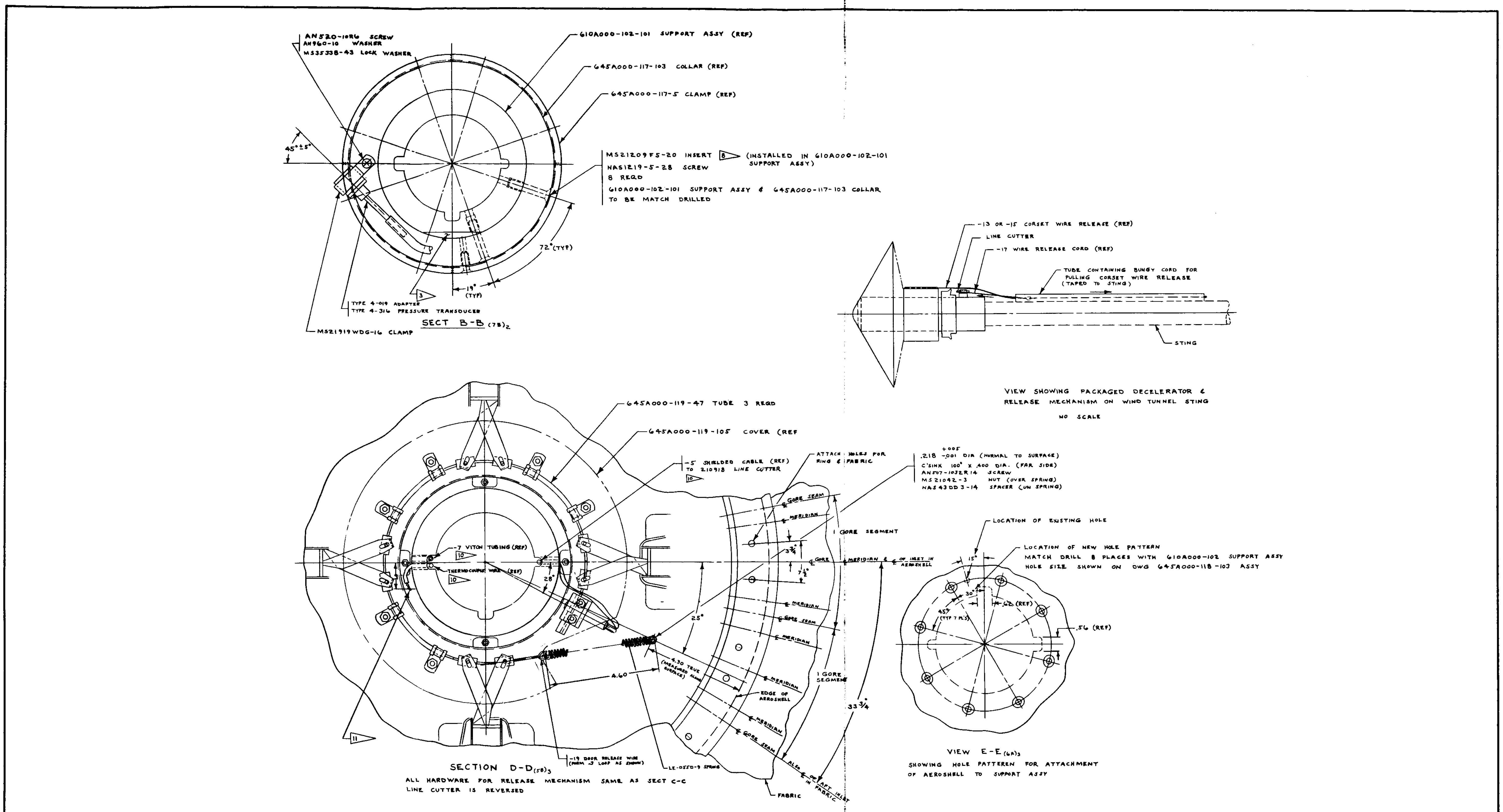

Figure A-4 - Model Assembly with 60-In. Dp (Sheet 4)

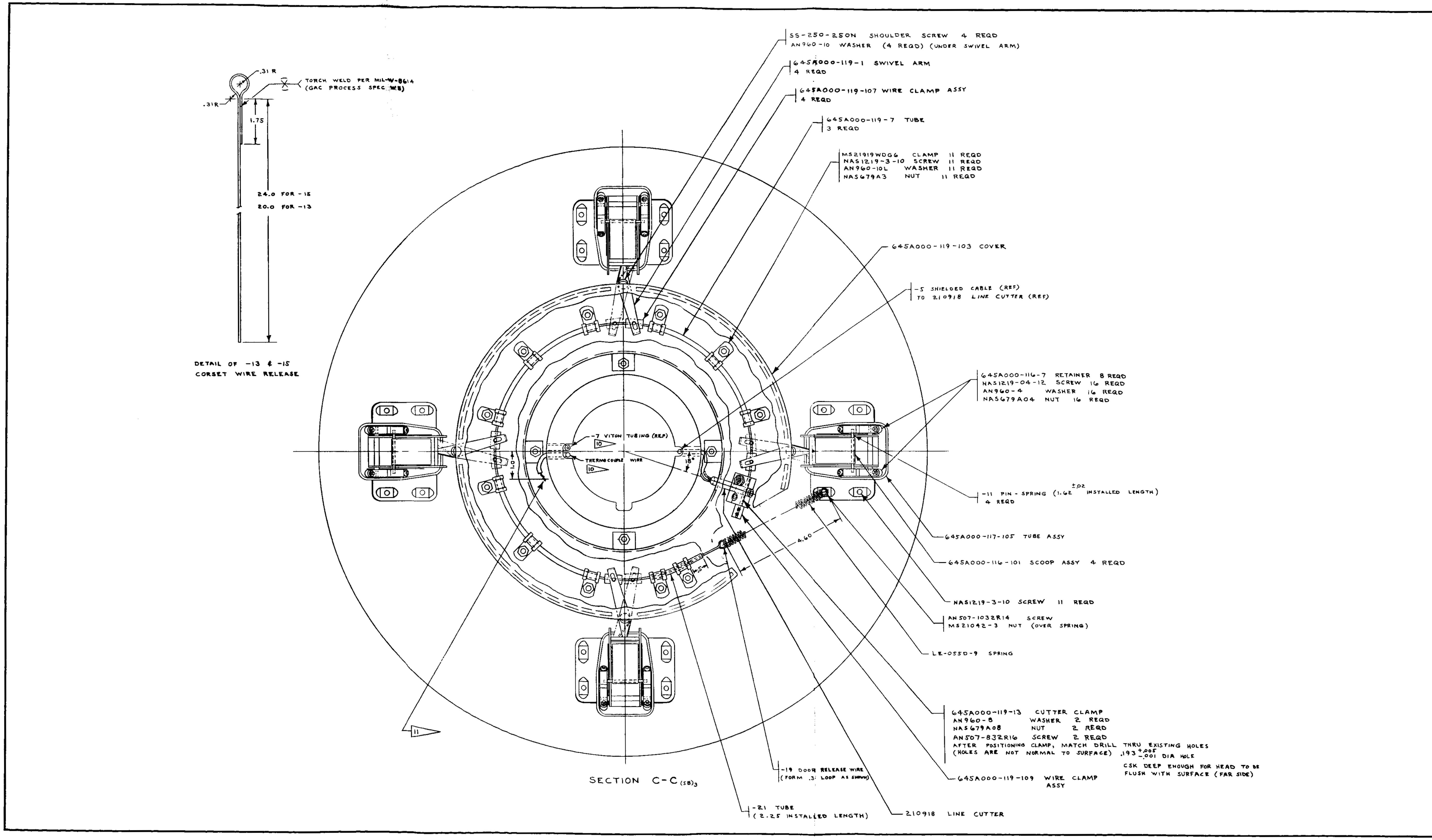

Figure A-5 - Model Assembly with 60-In. Dp (Sheet 5)

NOTES CONTINUED:

21. ALL "X" DIMENSIONS SHOWN ON DRAWINGS (-101, -103 & -105 ASSY) ARE REFERENCED FROM X= 0.00

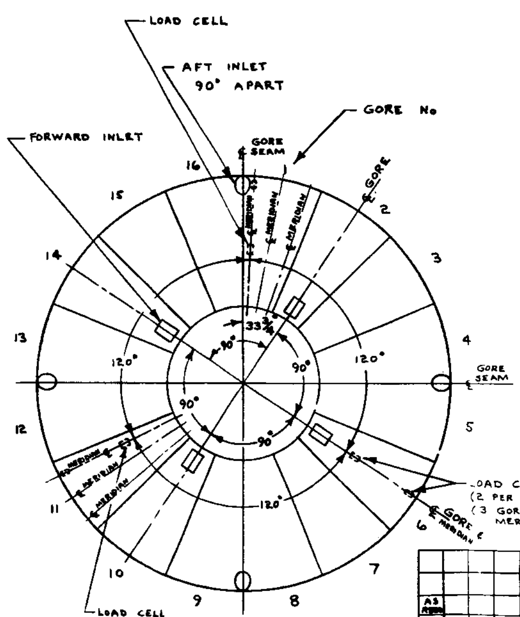

SCHEMATIC OF INLETS
(LOOKING INTO FORWARD END)
NO SCALE

NOTES:

1. IDENTIFY PER MIL-STD-130 (GAC PROCESS SPEC J2)
2. SEW PER STD 751
3. SEE GR60-4-51 FOR SEWING SYMBOL EXPLANATION

[4] PART No -1 THRU -10, -25 THRU -41, -49, -51, -59, -60 & -69 TO BE [5] FOR -101 & -103 ASSY & [6] FOR -105 ASSY

[5] GOODYEAR AEROSPACE CORP CODE GX601V0302, NOMEX/VITON FABRIC (WHITE) 2.6 OZ/YD^2, 95 x 85 LBS/IN T.S.

[6] DACRON CLOTH, 1.1 OZ/YD^2 (NATURAL), PATTERN No 15573, 35 x 35 LBS/IN T.S.

[7] NOMEX TAPE - SIMILAR TO MIL-T-5038, TYPE IV, 1.00 WIDE

[8] MAKE NOMEX TUBULAR BRAIDED CORD FROM 1200 DENIER 3 1/4 OZ TWIST NOMEX YARN AS FOLLOWS: 16 CARRIERS, 2 ENDS PER CARRIER, 9 TO 11 PICKS PER INCH

[9] MATERIAL FOR -101 & -103 TO BE NOMEX TAPE, SIMILAR TO MIL-T-5038 TYPE V, 9/16 WIDE, 500 LBS TEN.
MATERIAL FOR -105 ASSY TO BE DACRON TAPE, PATTERN No 7928. .50 WIDE, 500 LBS TEN. - BALLY RIBBON MILLS, BALLY, PA.

[10] NOMEX TAPE, SIMILAR TO MIL-T-5038, TYPE I, 9/16 WIDE, 500 LBS. TEN.

[11] LAP BIAS STRIP ONE INCH AT SPLICES

[12] PUT -11 MERIDIAN WEB UNDER 5 ± 1/2 LBS FOR ONE MINUTE MAX. TO MARK TO ENVELOPE MATCH MARKS

13. CANOPY SHAPE PARAMETERS: $K_f = 0.5199$, $K_r = 0.4421$, $\alpha = 0.685$
120° CONFIGURATION: FRONT ATTACHMENT - X/R = 0.1538, Y/R = 0.745
REAR ATTACHMENT - X/R = 0.1538, Y/R = 0.291
140° CONFIGURATION: FRONT ATTACHMENT - X/R = 0.44, Y/R = 0.6253
REAR ATTACHMENT - X/R = 0.1538, Y/R = 0.291

[14] DETERMINE -65 ROPE LOCATION BY FITTING TO CLAMP AT NEXT ASSEMBLY

[15] INSTALLATION INSTRUCTIONS FOR -29 REINF. TACK EDGE ALONG ℄ OF -11 MERIDIAN WEB, SEW LOWER EDGE AS SHOWN. SEW ALONG ALL MERIDIAN WEBS USING 1/8 / 304 E / 5-7 & CLOSING AT TACKED EDGE WITH 1/2 IN LAP

[16] PRIOR TO CLOSING ASSY, COAT ALL STITCHING INSIDE ENVELOPE (INCLUDING BURBLE FENCE) WITH ONE BRUSH COAT OF VITON (120° SOLIDS) IN ACCORD WITH GER 13317

[17] ALTERNATE DIRECTION OF WRAP FROM GORE TO GORE WHEN ASSEMBLY GORES

[18] PRIOR TO CLOSING ASSY, COAT ALL STITCHING INSIDE ENVELOPE (INCLUDING BURBLE FENCE WITH TWO BRUSH COATS OF DOW CORNING 92-009

[19] DACRON CLOTH TO BE COATED WITH 92-009 SILICONE, DOW CORNING, MIDLAND, MICH.
ALL COATING TO BE ON INSIDE OF DECELERATOR

[20] TOLERANCE FOR DIMENSION

0 TO 2.0 IN. ±.04 — 10 TO 30 IN. ±.19
2 TO 10.0 IN. ±.06 — 30 TO 60 IN ±.25
60 IN. & UP ±1%

PARTS LIST

-115	-113	-112	-111	-109	-108	-107	-105	-103	-101 (QTY REQD)	CODE IDENT NO.	PART OR IDENTIFYING NO.	NOMENCLATURE OR DESCRIPTION	MATERIAL AND SIZE	ZONE	ITEM OR FIND NO.
							12	12	12		-79	LOAD CELL TIE DOWN WEB	[9]		
							6	6	6			LOAD CELL	GOVT FURN EQUIP CONTR INSTALLED		
AS REQD											SIZE FF	THREAD	NOMEX-NAT. SIMILAR TO V-T-295 TYPE I		
							AS REQD	AS REQD	AS REQD		SIZE B	THREAD	NYLON-NATURAL V-T-295 TYPE I		
								AS REQD	AS REQD		SIZE E	THREAD	NOMEX-NAT. SIMILAR TO V-T-295 TYPE I		
								AS REQD	AS REQD		SIZE F	THREAD	NOMEX-NAT. SIMILAR TO V-T-295 TYPE I		
							AS REQD				SIZE E	THREAD	DACRON-NATURAL V-T-285 TYPE I, CL II		
							AS REQD				SIZE F	THREAD	DACRON-NATURAL V-T-285 TYPE I, CL II		
1											-77	CORD	NYLON-NATURAL MIL-C-7515 TYPE III 36 IN. LG.	$5C_8$	
							4				645A000-115-103	INLET ASSY		$4A_3$	
								4	4		645A000-115-101	INLET ASSY		$4A_3$	
5											-75	WEB	NOMEX WEBBING-NATURAL SIMILAR TO MIL-T-5038 TYPE III, 1.00 WIDE x 36 IN. LG	$2C_8$	
2											-73	PANEL	[5]	$6A_8$	
	1										-71	ROPE	3/16 DIA. DACRON (SAMSON CORDAGE STABLE BRAID	$5B_7$	
	1										-69 (DETAIL SH 7)	PATTERN	[4]	$8E_7$	
							1		1		-67	ROPE-FORWARD END	3/16 DIA. DACRON (SAMSON CORDAGE STABLE BRAID)	$7D_5$	
								1			-65 [14]	ROPE-FORWARD END	3/16 DIA. DACRON (SAMSON CORDAGE STABLE BRAID)	$8B_5$	
							1	1	1		-63	ROPE-AFT END	3/16 DIA. DACRON (SAMSON CORDAGE STABLE BRAID)	$7D_5$	
							1		1		-61	ABRASION WEB	[7]	$3F_6$	

PARTS LIST

-115	-113	-112	-111	-109	-108	-107	-105	-103	-101 (QTY REQD)	CODE IDENT NO.	PART OR IDENTIFYING NO.	NOMENCLATURE OR DESCRIPTION	MATERIAL AND SIZE	ZONE	ITEM OR FIND NO.
X											-115 (SH 8)	CORSET ASSY			
	X										-113	SOCK ASSY		$8D_7$	
		1									-60	FORWARD PANEL (OPP)	[4]	$3C_4$	
			1								-59	FORWARD PANEL (SHOWN)	[4]	$3C_4$	
							4		4		-57	LOOP	[10]	$5E_2$	
							4	4	4		-55	LOOP	[10]	$4G_2$	
	2			2							-53	LOOP	[10]	$7G_7$	
	1			1							-51 (DETAIL SH 7)	PATTERN	[4]	$6F_7$	
				1							-49 (DETAIL SH 7)	PATTERN	[4]	$7E_7$	
							8	8	8		-47	CORD	24.0 LG [8]	$4F_2$	
							8	8	8		-45	CORD	30.0 LG [8]	$6D_2$	
							4		4		-43	ROPE	3/16 DIA DACRON (SAMSON CORDAGE STABLE BRAID	$2C_6$	
							8		8		-41	REINF	[4]	$5F_6$	
							4		4		-39	STRIP-BIAS	[4]	$2C_6$	
							1	1	1		-37	STRIP-BIAS	[4] [11]	$4D_5$	
							1	1	1		-35	STRIP-BIAS	[4] [11]	$3B_5$	
							2	2	2		-33	STRIP-BIAS	[4] [11]	$4E_5$	
								2			-31 (DETAIL SH 5)	REINF	[4]	$6B_5$	
									1		-29 (DETAIL SH 7)	REINF [15]	[4]	$7F_5$	
							1	1	1		-27	STRIP-BIAS	[4] [11]	$8F_5$	
							8	8	8		-25	PATCH	[4]	$5B_3$	
							8	8	8		-23	LOWER CORD	16.0 LG [8]	$4A_3$	
							8	8	8		-21	UPPER CORD	16.0 LG [8]	$5F_3$	
									1		-19	WEB	[7] 12 FT LG	$4H_2$	
									1		-17	WEB	[7] 7 FT LG	$5G_2$	
									1		-15	WEB	[7] 6 FT LG	$6F_2$	
									1		-13	WEB	[7] 3 FT LG	$6E_2$	
							48	48	48		-11	MERIDIAN WEB	[9] [12] (100 YD)	$3F_3$	
							8	8	8		-10 (DETAIL SH 4)	B/F PANEL	[4]	$2E_5$	
							8	8	8		-9 (DETAIL SH 4)	B/F PANEL	[4]	$2E_5$	
											-7 (DETAIL SH 4)	REINF	[4]	$4B_4$	
		1			1						-6 (DETAIL SH 4)	GORE REINF (OPP)	[4]	$3D_4$	
			1			1					-5 (DETAIL SH 4)	GORE REINF (SHOWN)	[4]	$3D_4$	
		1			1						-4 (DETAIL SH 4)	AFT PANEL (OPP)	[4]	$2C_4$	
			1			1					-3 (DETAIL SH 4)	AFT PANEL (SHOWN)	[4]	$2C_4$	
					1						-2 (DETAIL SH 4)	FORWARD PANEL (OPP)	[4]	$3C_4$	
						1					-1 (DETAIL SH 4	FORWARD PANEL (SHOWN)	[4]	$3C_4$	
		X						8			-112	GORE ASSY (OPP)	[17]	$5B_4$	
			X					8			-111	GORE ASSY (SHOWN)	[17]	$5B_4$	
				X							-109	SOCKED ASSY	[17]	$5B_4$	
					X		8		8		-108	GORE (OPP)	[17]	$5B_4$	
						X	8		8		-107	GORE (SHOWN)	[17]		
				4			X				-105 [18] [19]	DECELERATOR ASSY	DACRON MATL. ATTACHED TO 120° AEROSHELL		
	4							X			-103 [16]	DECELERATOR ASSY	NOMEX MATL. ATTACHED TO 140° AEROSHELL		
				4					X		-101 [16]	DECELERATOR ASSY	NOMEX MATL. ATTACHED TO 120° AEROSHELL		

Figure A-6 - Decelerator Assembly 60-In. Dp (Sheet 1)

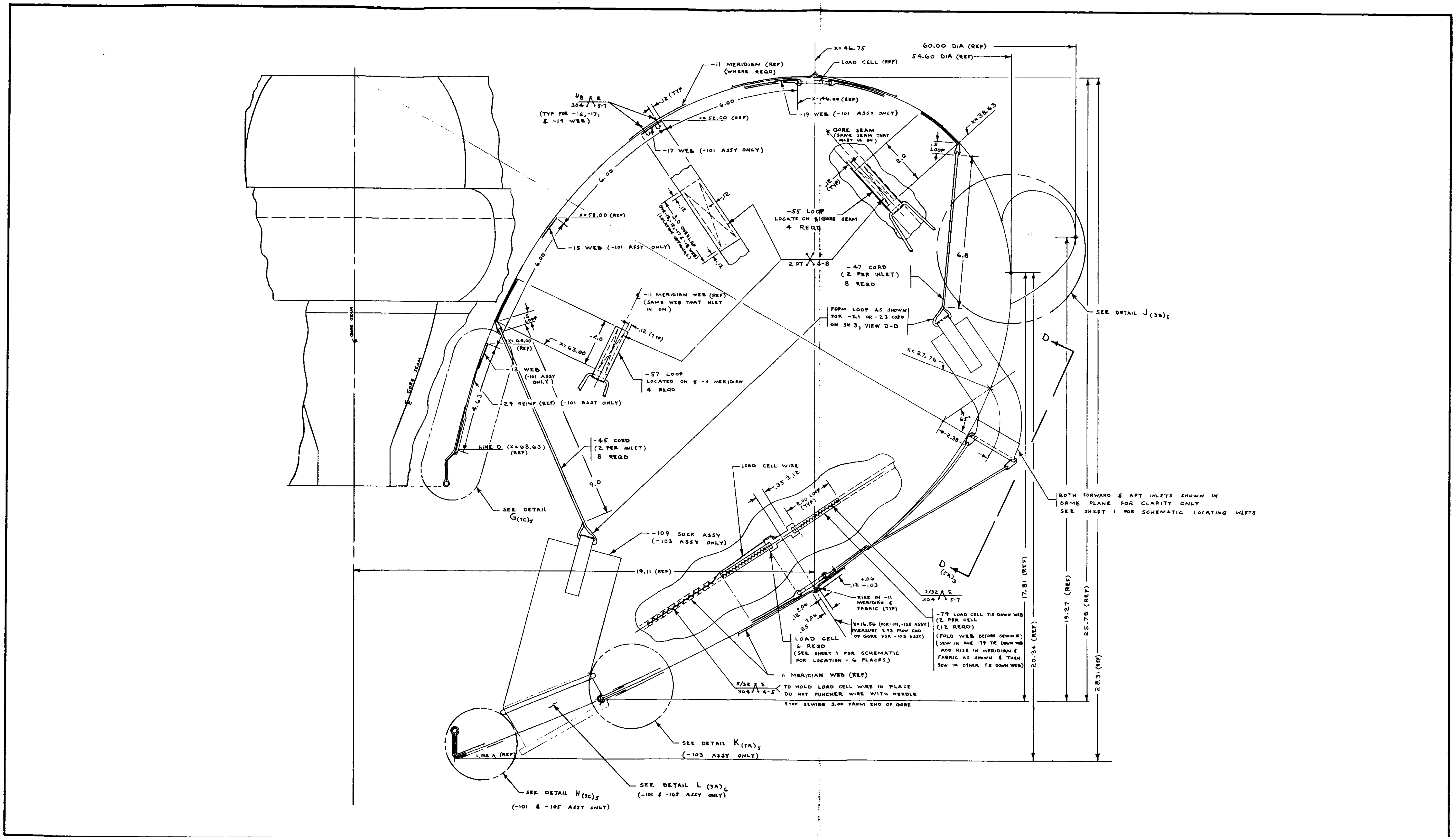

Figure A-7- Decelerator Assembly 60-In. Dp (Sheet 2)

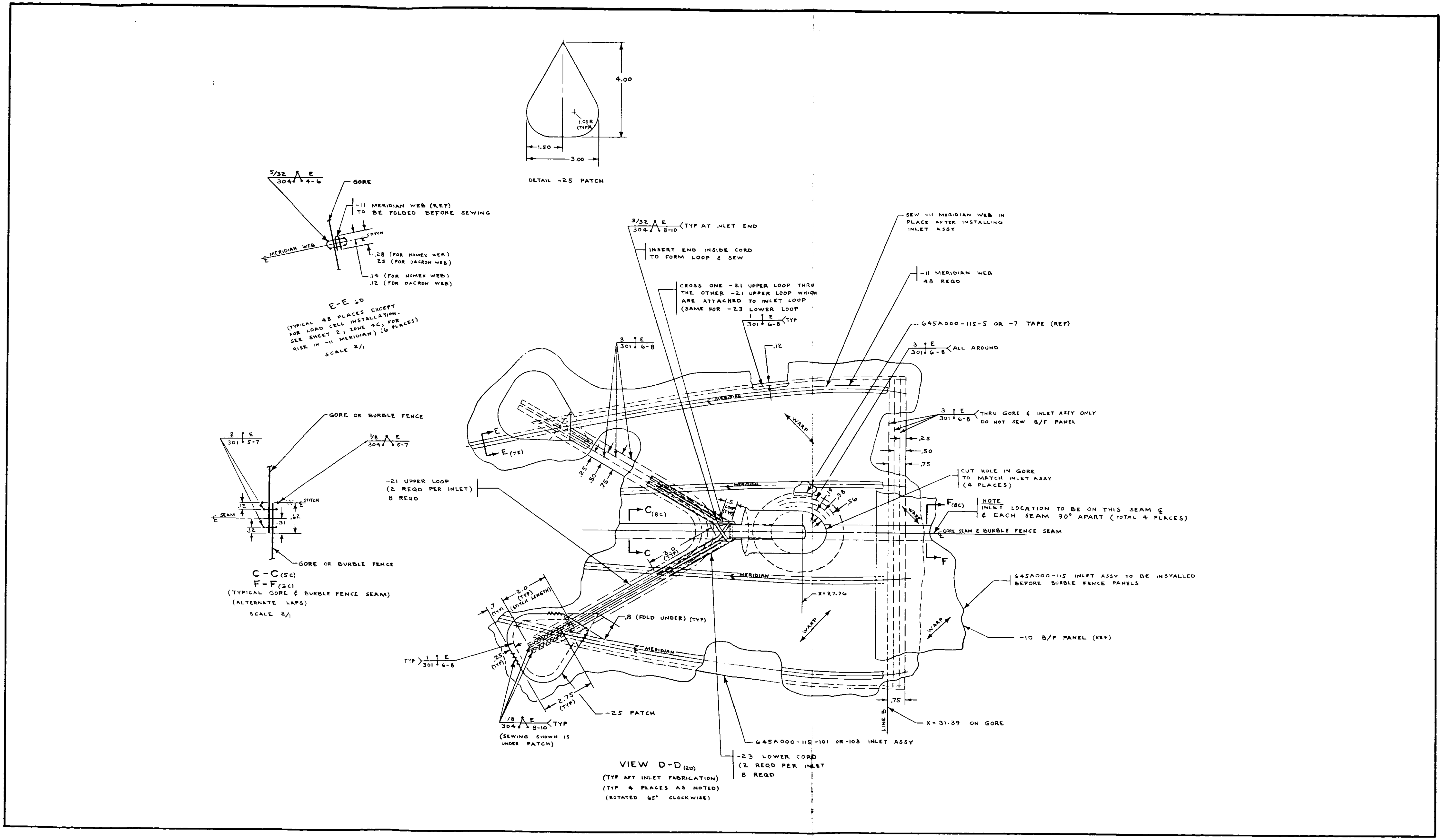

Figure A-8- Decelerator Assembly 60-In. Dp (Sheet 3)

TABLE OF COORDINATES FOR -5 & -6 B/F PANEL

X	Y
0.00	5.80
1.00	5.70
2.00	5.75
3.00	5.86
3.50	5.92
4.00	5.94
4.50	5.97
5.00	5.94
6.00	5.83
7.00	5.66
8.00	5.54
9.00	5.66
9.30	5.80

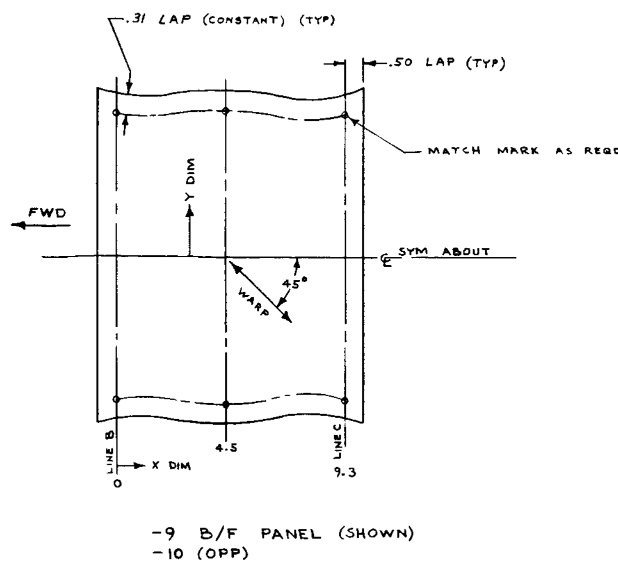

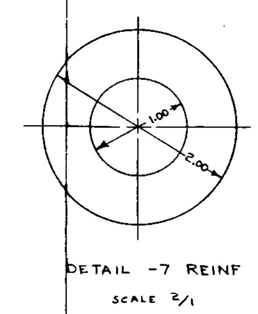

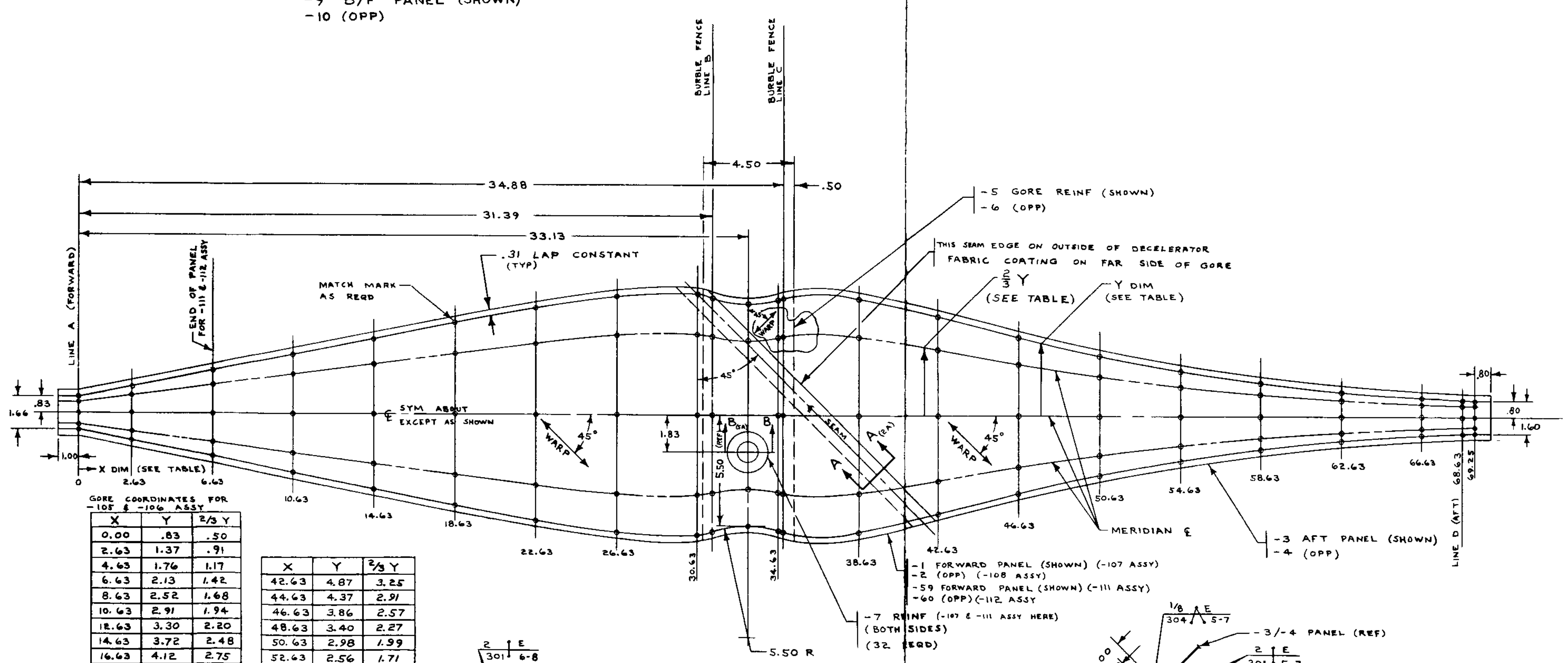

GORE COORDINATES FOR -105 & -106 ASSY

X	Y	2/3 Y
0.00	.83	.50
2.63	1.37	.91
4.63	1.76	1.17
6.63	2.13	1.42
8.63	2.52	1.68
10.63	2.91	1.94
12.63	3.30	2.20
14.63	3.72	2.48
16.63	4.12	2.75
18.63	4.52	3.01
20.63	4.90	3.27
22.63	5.26	3.51
24.63	5.58	3.72
26.63	5.82	3.88
28.63	6.00	4.00
30.63	5.98	3.98
32.63	5.50	3.67
34.63	5.72	3.82
36.63	6.03	4.02
38.63	5.74	3.83
40.63	5.33	3.56

X	Y	2/3 Y
42.63	4.87	3.25
44.63	4.37	2.91
46.63	3.86	2.57
48.63	3.40	2.27
50.63	2.98	1.99
52.63	2.56	1.71
54.63	2.20	1.47
56.63	1.89	1.26
58.63	1.62	1.08
60.63	1.39	.93
62.63	1.21	.81
64.63	1.04	.69
66.63	.92	.61
68.63	.83	.55
69.25	.80	.53

-107 & -111 GORE (SHOWN)
-108 & -112 (OPP)

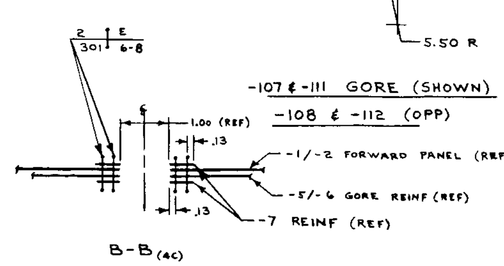

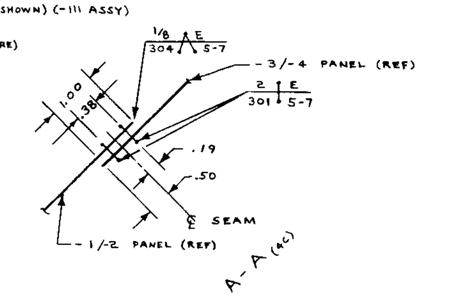

Figure A-9- Decelerator Assembly 60-In. Dp (Sheet 4)

APPENDIX B. - STRESS ANALYSIS

Fabric Stresses

The decelerator stress analysis in Reference 3 presents the relationships, based on the isotensoid method of analysis, for determining the limit loads for the meridians and fabric. These relationships are:

$$T_m = \frac{k p \pi R^2}{n} \qquad \text{(B-1)}$$

$$f_b = \frac{F p R}{2}, \qquad \text{(B-2)}$$

where from Reference 3

$$k_f = 0.52, \text{ and}$$

$$F = 0.1294.$$

From the relation $C_{p_i} = 2.0$, (see Reference 3),

$$\frac{p_i - p_\infty}{q_\infty} = 2.0 \; ;$$

or,

$$\frac{p_i - p_\infty}{0.7 M_\infty^2 p_\infty} = 2.0 \; .$$

Therefore,

$$\frac{p_i}{p_\infty} = 0.7 M_\infty^2 (2) + 1 \qquad \text{(B-3)}$$

$$= 13.6 \text{ for } M_\infty = 3.0 \; .$$

Since $p = p_i - p_b$,

$$\frac{p}{p_\infty} = \frac{p_i}{p_\infty} - \frac{p_b}{p_\infty} \; . \qquad \text{(B-4)}$$

From the analytical pressure distribution of Figure 9 and by substituting Equation B-4 into Equation B-3, the following relation is obtained:

$$\frac{p}{p_\infty} = 13.60 - 0.4$$

$$= 13.2$$

For $q_{\infty} = 120$ psf and $M_{\infty} = 3.0$,

$$p_{\infty} = 19.05 \text{ psf.}$$

Therefore,

$$p = (13.2)(19.05)$$

$$= 252 \text{ psf}$$

$$= 1.75 \text{ psi.}$$

Therefore, the limit meridian and fabric loads are, from Equations B-1 and B-2, respectively,

$$T_m = \frac{(0.52)(1.75)(\pi)(27.3)^2}{48}$$

$$= 44.5 \text{ lb,}$$

and

$$f_b = \frac{(0.1294)(1.75)(27.3)}{2}$$

$$= 3.09 \text{ lb/in.}$$

Hard Structure

The hard structure for the current models was stress analyzed in accordance with the AEDC wind tunnel quality control procedure (AEDC OCP-000-21). The analysis is not detailed in this report.

APPENDIX C. - AID INFLATION ANALYSIS

In setting up a computer program to predict the inflation rate of an attached inflatable decelerator, a basic opening model must be postulated to characterize the events that take place during the inflation process. An effort has been made to keep this model simple while still permitting an adequate modeling of the flow at the inlets. Wind-tunnel movies of the AID have been used to generate the inflation model shown in Figure C-1. Reasonable agreement with experimental results should be attainable with this model.

The initiation of the inflation sequence is taken as the time when the front inlets are facing the airstream. As this free-stream airflow approaches the blunted conical forebody, it passes through a detached shock wave that is very nearly normal to the flow in the nose region of the forebody. The flow that enters the inlets passes through this normal portion of the shock.

The free-stream total pressure and temperature of the flow are given by the following relations, respectively:

$$T_t = T_\infty \left[1 + \frac{(\gamma - 1)}{2} M_\infty^{\ 2}\right]$$

$$p_{t_\infty} = p_\infty \left[1 + \frac{(\gamma - 1)}{2} M_\infty^{\ 2}\right]$$

The total temperature of the air remains constant as it passes through the shock wave; however, the total pressure will decrease across the shock wave. For the flow passing through the normal portion of the detached shock, the new total pressure is:

$$p_t = p_\infty \left[\frac{(\gamma + 1)}{2} M_\infty^{\ 2}\right]^{\frac{\gamma}{\gamma - 1}} \left[\frac{\gamma + 1}{2\gamma M_\infty^{\ 2} - (\gamma - 1)}\right]^{\frac{1}{\gamma - 1}} .$$

The flow, after passing through the shock, slows briefly in the stagnation region, turns along the surface of the blunted nose and expands onto the conical surface and subsequently enters the forward inlets. If the cone angle is small or the Mach number high, the flow at the forward inlets could be supersonic. The static pressure at the forward inlet is found, assuming Newtonian flow over the cone, from the following relation:

$$p_f = \gamma\, p_\infty M_\infty^{\ 2} \sin^2 \frac{\alpha}{z}$$

The Mach number in the inlet region is given by the relation:

$$M_f = \sqrt{\frac{2}{\gamma - 1}\left[\left(\frac{p_t}{p_f}\right)^{\frac{\gamma - 1}{\gamma}} - 1\right]} .$$

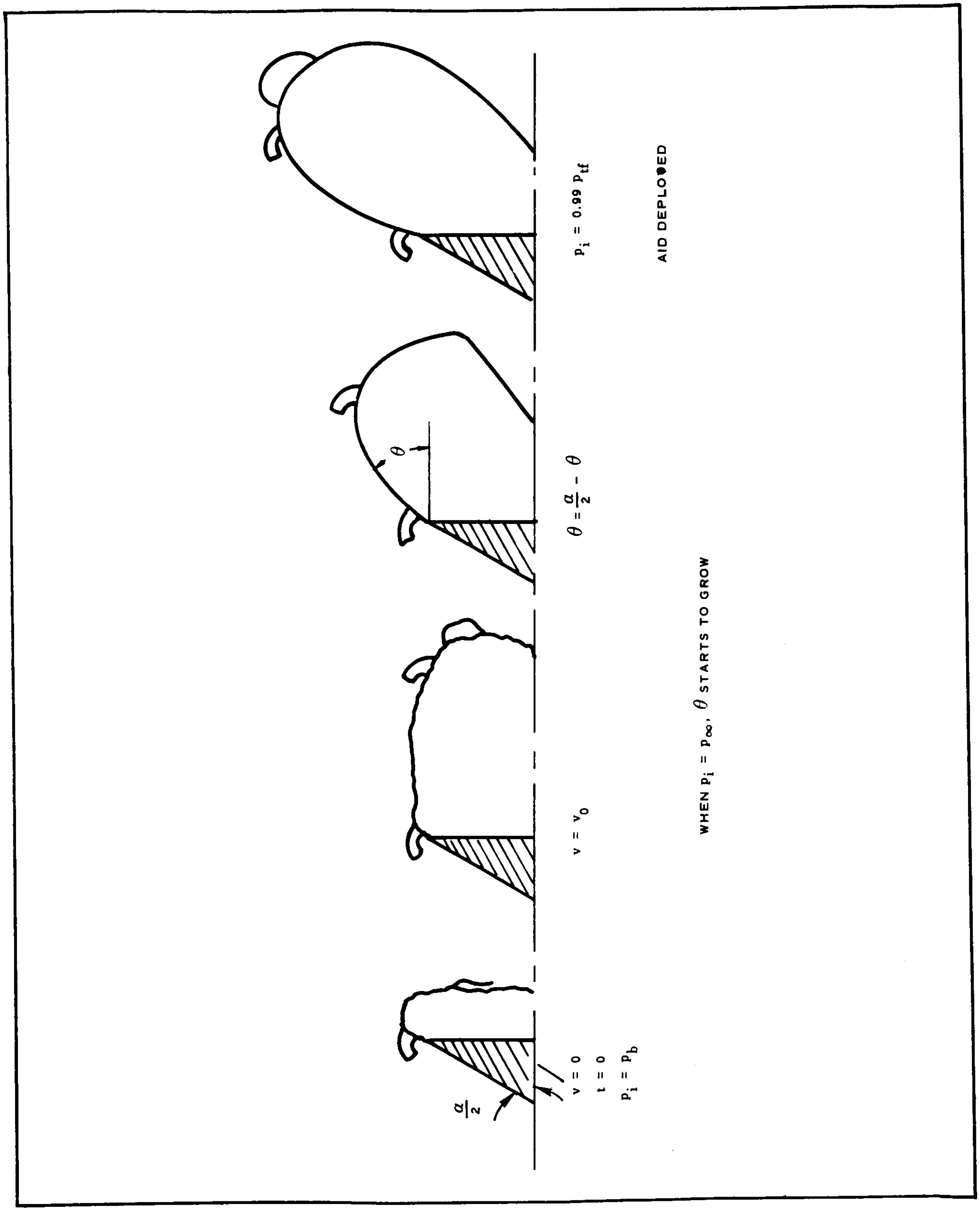

Figure C-1. - AID Inflation Model

Of course, if $M_f \leq 1$, the front inlet total pressure, p_{tf}, is still p_t. However, if $M_f > 1$, then the total pressure behind the inlet shock is given by the relation:

$$p_{tf} = p_t \left[\frac{(\gamma + 1) M_f^2}{(\gamma - 1) M_f^2 + 2} \right]^{\frac{\gamma}{\gamma - 1}} \left[\frac{\gamma - 1}{2 \gamma M_f^2 - (\gamma - 1)} \right]^{\frac{1}{\gamma - 1}} .$$

At the time the canopy starts to inflate it is assumed that the internal pressure, p_i, of the undeployed decelerator is equal to the base pressure of the vehicle. The base pressure is based on the empirical correlations:

$$p_b = p_\infty - \left(\frac{1}{M_\infty^2 + 0.7} \right) \frac{\gamma}{2} p_\infty M_\infty^2 .$$

The total pressure ratio across the inlet is now known and the mass flow rate into the inlet can be calculated. The mass flow rate is assumed to be proportional to the isentropic flow rate, where the proportionality constant is the inlet flow coefficient. This coefficient is treated in the manner suggested in Reference 1. The coefficient is expressed as a combination of two factors: the first is the flow coefficient of a sharp-edged orifice. This coefficient is expressed as a function of the total pressure ratio across the orifice. The second factor is a constant inlet efficiency to account for the inlet geometry and its fabric construction.

The mass flow rate at the forward inlet then, is given by the following relation:

$$\dot{m}_f = A_f \eta_f C_f \sqrt{\left(\frac{2\gamma}{\gamma - 1} \right) \left(\frac{p_{tf}^2}{RT_t} \right) \left(\frac{p_i}{p_{tf}} \right)^{2/\gamma} \left[1 - \left(\frac{p_i}{p_{tf}} \right)^{\frac{\gamma - 1}{\gamma}} \right]}$$

where $C_f = f(p_{tf}/p_i)$.

As the decelerator starts to inflate behind the aeroshell (see Figure C-1), the volume will increase with time, while the internal pressure remains at p_b according to the following relation:

$$V(t) = \frac{\dot{m}_f t}{\rho}$$

$$= \frac{\dot{m}_f t}{p_b} R T_t$$

At some nominal volume, the canopy will be filled with air at a pressure p_b and from that time on, the pressure will rise until the final pressure is reached. For the model in Figure C-1, the nominal volume was chosen as V_o, which is equivalent to the total canopy volume. After V_o is reached, the internal pressure rises as a function of time according to the following relation:

$$p_i = \int^t \frac{\dot{m}\,dt}{V_o} RT_t .$$

Once the pressure in the canopy exceeds that in the base region, the air will start to flow through the fabric. The rate of this flow will depend upon the porosity or permeability of the fabric. For a heavily coated cloth this loss will be neglegible, but for some lightly coated cloths, this loss may be significant enough to modify the inflation process. Another factor that must be considered in calculating the air flow from the rear surface fabric is the increase in effective porosity of the rear surface due to an increasing pressure differential across the rear surface as the model inflates. A relationship between the porosity and pressure ratio of the following form is used.

$$\lambda = \lambda_o \left\{ 1 + \beta \left[e^{-k \, (p_i - p_b)} - 1 \right] \right\} .$$

The mass flow rate due to this porosity is given by the following relation:

$$\dot{m}_p = A_s \lambda \sqrt{\left(\frac{2\gamma}{\gamma - 1}\right) \frac{p_i^2}{R} \left(\frac{p_b}{p_i}\right)^{z/\gamma} \left[1 - \left(\frac{p_b}{p_i}\right)^{\frac{\gamma - 1}{\gamma}}\right]} .$$

Now, the mass flow into the system is given by:

$$\dot{m} = \dot{m}_f - \dot{m}_p$$

The canopy cannot inflate beyond the edge of the conical forebody until the internal pressure exceeds the free-stream static pressure. When the pressure rises above the free-stream value, the fabric adjacent to the hard cone assumes the form and angle θ shown in Figure C-1 relative to the aeroshell longitudinal axis; in this case the assumed Newtonian pressure distribution is:

$$\theta = \arcsin \sqrt{\frac{p_i - p_\infty}{\gamma M_\infty^2 p_\infty}} .$$

As this angle increases, the AID continues to inflate as a result of the air flow into the front inlets only, until the rear inlets become effective. At the point where the rear inlets become effective, defined as the position where the rear inlets become parallel with the flow, the mass flow equation must be modified. The angle by which the inlet lags behind θ is defined by $\bar{\theta}$, therefore, the angle between the free-stream flow and the rear inlet is $\theta - \bar{\theta}$. The static pressure in the rear inlet region is:

$$p_r = \gamma M_\infty^2 \, p_\infty \sin^2 (\theta - \bar{\theta}) \quad ,$$

and the Mach number at the rear inlet is:

$$M_r = \sqrt{\left(\frac{2}{\gamma - 1}\right)\left[\left(\frac{p_t}{p_r}\right)^{\frac{\gamma - 1}{\gamma}} - 1\right]} .$$

Again, if $M_r \leq 1$, then the rear inlet total pressure is p_t. However, if $M_r > 1$, the value will be given by

$$p_{tr} = p_t \left[\frac{(\gamma + 1) M_r^2}{(\gamma - 1) M_r^2 + 2}\right]^{\frac{\gamma}{\gamma - 1}} \left[\frac{\gamma + 1}{2 \gamma M_r^2 - (\gamma - 1)}\right]^{\frac{1}{\gamma - 1}} .$$

As before a dual factor flow coefficient is used and the mass flow into the rear inlets is given by:

$$\dot{m}_r = \eta_r C_r A_r \sqrt{\left(\frac{2\gamma}{\gamma - 1}\right)\left(\frac{p_{tr}^2}{RT_t}\right)\left(\frac{p_i}{p_{tr}}\right)^{2/\gamma} \left[1 - \left(\frac{p}{p_{tr}}\right)^{\frac{\gamma - 1}{\gamma}}\right]}$$

The mass flow into the system is now:

$$\dot{m} = \dot{m}_f - \dot{m}_p + \dot{m}_r \quad .$$

This flow is allowed to continue until the pressure ratio across the inlets nears unity. If the rear pressure ratio p_i/p_{tr} exceeds 99 percent, then $\dot{m}_r$ is equated to zero. If the front inlet pressure ratio p_i/p_{tf} exceeds 99 percent, the computation is concluded and the system is considered to be fully inflated. The integration of the mass flow rate with time is done by simply summing $\dot{m}\Delta t$ values. If after $200\Delta t$ intervals, the system has not fully inflated, the computation is terminated. The summation of 200 Δt intervals can occur easily for systems with porous fabrics. The inflow through the inlets will be equalized by the outflow through the fabric and the pressure will stabilize at a value well below $0.99\ p_{tf}$.

APPENDIX D. - AEROSHELL INLET ANALYSIS

General

This appendix discusses the analysis conducted to determine the forces acting on the aeroshell inlets, the characteristics of the inlet spring, and the frictional forces that the deployment spring must overcome to release the aeroshell inlets.

Inlet Forces

When the door is in the closed position, the net force acting on the inlet is

$$F = (p_e - p_i) A_s \quad .$$

Pressure measurement from the wind-tunnel tests of models shown in Figures 6 and 7 indicate that the internal pressure, p_i, of the model prior to deployment is relatively small when compared to p_∞ . The external pressure, p_e, however, is approximately one order of magnitude greater than p_∞ as will be shown subsequently. Therefore, assuming that the internal pressure is negligible as compared to the external pressure, the maximum differential pressure acting on the inlet is equivalent to the external pressure. The maximum force acting on the inlet in the closed position then is:

$$F_m = p_e A_i \quad .$$

To determine the magnitude of the external pressure when the door is in the closed position, modified Newtonian theory is used to predict an average pressure ratio of p_e/p_∞. From the Newtonian theory, this ratio is defined as:

$$\frac{p_e}{p_\infty} = 1.0 + \left(\frac{p_{t_2}}{p_\infty} - 1.0 \right) \sin^2 \theta \quad .$$

From Reference 14, at $M_\infty = 3.0$:

$$\frac{p_{T_2}}{p_\infty} = \frac{1}{0.829}$$

$$= 1.21$$

For the 120-deg conical aeroshell, $\theta = 60$ deg. Therefore,

$$\frac{p_e}{p_\infty} = 1.0 \, (12.1 - 1.0) \sin^2 60 \text{ deg}$$

$$= 9.32 \quad .$$

For the 140-deg aeroshell,

$$\frac{p_e}{p_\infty} = 1.0 + (12.1 - 1.0) \sin^2 70 \text{ deg}$$

$$= 10.8 .$$

Using the larger of the pressure ratios, the maximum force acting on the inlet is:

$$F_m = \frac{p_e}{A_i}$$

$$= \frac{(10.8)(19.05)(3.75)}{144}$$

$$= 5.36 ,$$

where A_i is as determined in Figure 13.

As stated in Section V, the inlet spring was designed to ensure a positive force in the open orientation to present the possibility of inlet flutter. For design purposes the spring was considered to maintain a force equivalent to that acting on the inlet in the closed position, which was previously determined as 5.36 lb. The subsequent analysis will show that there is actually a small aerodynamic force tending to maintain the inlet open. Therefore, the aeroshell inlets should deploy rather positively and maintain the deployed position without unfavorable dynamics or flutter. The forces acting on the aeroshell inlet (see Figure D-1) at the beginning of inflation only are represented by the following relationships:

$$\vec{F}_1 = p_1 A_1 ,$$

and

$$\vec{F}_2 = p_2 A_2 .$$

The force resulting from the change in momentum in Figure D-2 must be equal to the resultant of the three forces shown in Figure D-1. Therefore,

$$\vec{F} - \vec{F}_1 - \vec{F}_2 = \frac{d}{dt}(m\vec{v}) .$$

By summing forces in the x direction, then:

$$\sum F_x = -\vec{F} + \vec{F}_1 \cos(90 - \alpha) + \vec{F}_2 \cos\alpha$$

$$= -\rho_1 \vec{V}_1 A_1 \left[\vec{V}_1 \cos(90 - \alpha)\right] - \rho_2 \vec{V}_2 A_2 \left[\vec{V}_2 \cos(90 - \theta + \alpha)\right] .$$

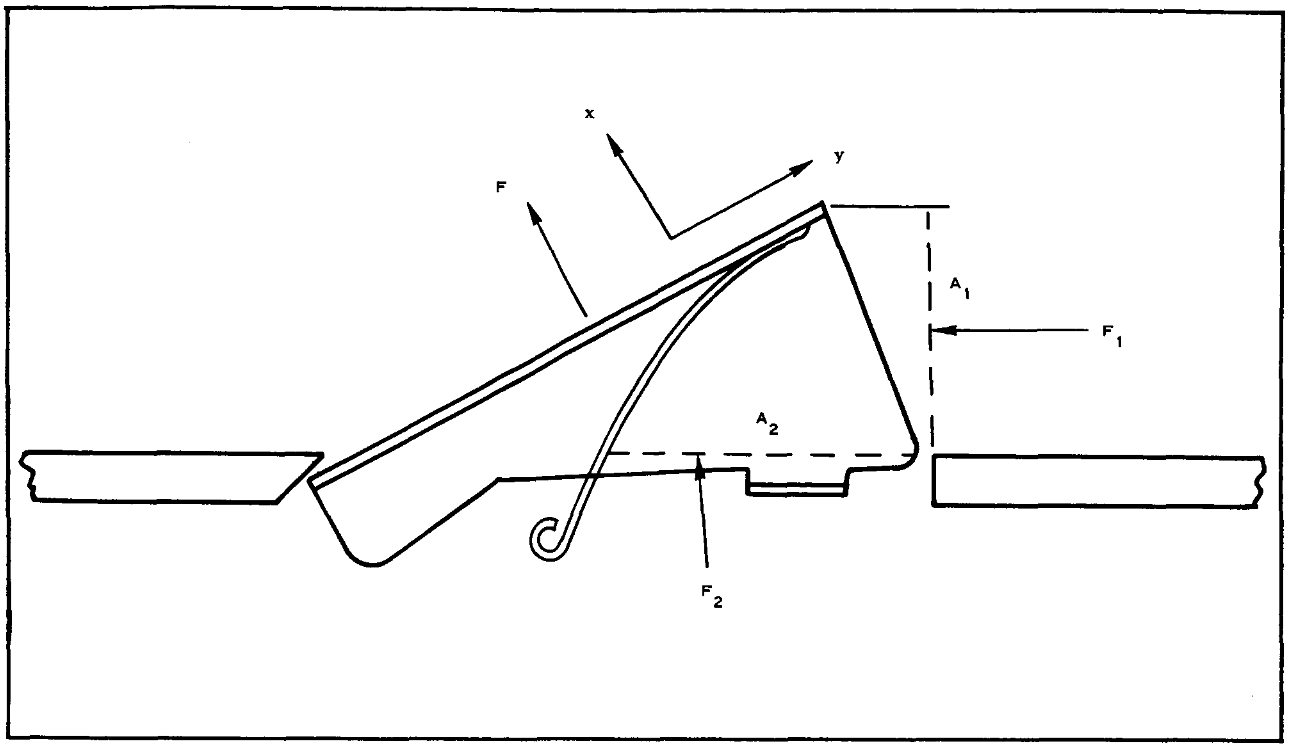

Figure D-1. - Forces Acting on Aeroshell Inlet

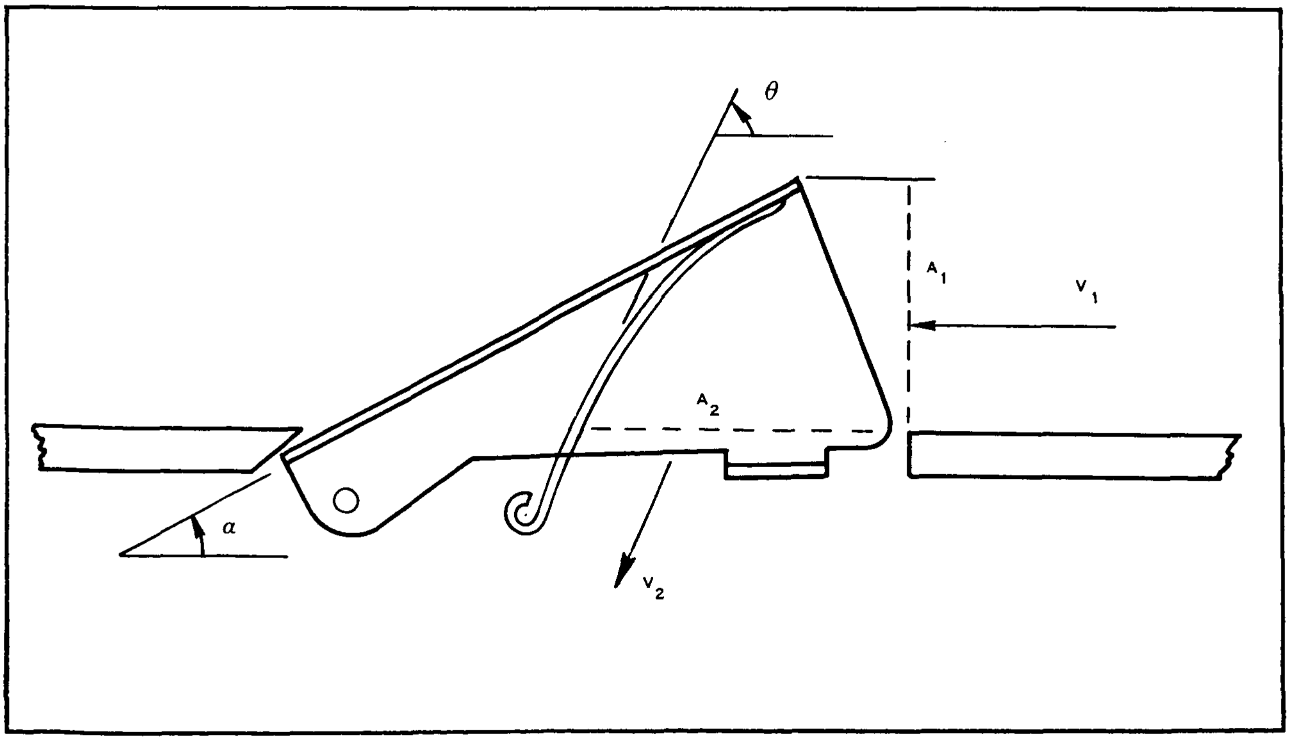

Figure D-2. - Change in Direction of Flow Entering Aeroshell Inlet

Therefore,

$$\vec{F} = \vec{F}_1 \cos(90 - \alpha) + \vec{F}_2 \cos\alpha + \rho_1 \vec{V}_1 A_1 \left[\vec{V}_1 \cos(90 - \alpha)\right] + \rho_2 \vec{V}_2 A_2 \left[\vec{V}_2 \cos(90 - \theta + \alpha)\right].$$

The force of the fluid on the inlet is computed below for both the 120- and 140-deg aeroshells at: (1) start of inflation and (2) full inflation. The following parameters do not vary for either configuration.

$$p_\infty = 190.5 \text{ psf},$$

$$m_\infty = 3.0\ ,$$

$$A_1 = 0.00892 \text{ sq ft},$$

$$A_2 = 0.0211 \text{ sq ft},$$

$$\theta = 65 \text{ deg, and}$$

$$\alpha = 23.6 \text{ deg}.$$

The inlet location is 0.64s, where s is the distance from the aeroshell apex to the base.

For the 120-deg configuration, $p_L/p_\infty = 9.97$, and $M_L = 0.49$ at 0.64s from the apex according to Reference 17.

Therefore,

$$p_L = (9.97)(19.05)$$
$$= 190 \text{ psf},$$

and

$$q_L = \frac{\gamma}{2} p_L m_L^2$$
$$= (0.7)(190)(0.49)^2$$
$$= 32 \text{ psf}.$$

At the start of inflation,

$$\rho_2 v_2 = \rho_1 v_1 = 2q_L\ ,$$

where

$$p_2 = p_1 = p_L\ .$$

To determine the resultant of the forces shown in Figure D-1, the values of the above parameters are substituted into Equation D-1:

$$\vec{F} = (190)(0.00892)(\cos 66.4) + (190)(0.0211)(\cos 23.6) +$$

$$2(32)(0.00892)(\cos 66.4) + 2(32)(0.0211)(\cos 48.6)$$

$$= 5.45 \text{ lb.}$$

The recirculation force, $\vec{F}_B$, acts on the back surface of the inlet in a negative x direction. It is assumed that

$$\vec{F}_B = p_L A_i ,$$

where A_i is determined from Figure 13.

Therefore,

$$\vec{F}_B = (190)(0.0236)$$

$$= 4.48 .$$

The resulting aerodynamic force acting on the inlet is:

$$\vec{F}_a = \vec{F} - \vec{F}_B$$

$$= 5.45 - 4.48$$

$$= 0.97 .$$

At full inflation, $F_a = qC_D A_1$, where the C_D of a flat plate is used.

Therefore,

$$\vec{F}_a = (32)(1.17)(0.00892)$$

$$= 0.884 \text{ lb.}$$

For the 140-deg configuration, $p_L/p_\infty = 10.28$ and $M_L = 0.441$ at 0.64s from the apex according to Reference 16.

Therefore,

$$p_L = (10.28)(19.05)$$

$$= 196 \text{ psf},$$

and

$$q_L = (0.7)(196)(0.441)^2$$

$$= 26.7 \text{ psf.}$$

Using the same calculation procedure as for the 120-deg cone, the resulting aerodynamic force at the beginning of inflation is

$$F_a = 0.92 \text{ lb},$$

and at full inflation, the resulting aerodynamic force is

$$F_a = 0.88 \text{ lb}.$$

Therefore the fact has been established that the resultant aerodynamic force acting on the inlets tends to maintain the inlet in the open position.

Release Spring Forces

The release spring must be capable of producing a force greater than the friction force generated between the four restraining rods and the release levers. By summing moments about the rotational axis of the inlet shown in Figure D-3, then

$$l_1(F_{rl}) = l_2(F_{rs})$$

or

$$F_{rl} = \frac{(0.65)(25)}{2.55}$$
$$= 6.38 \text{ lb}.$$

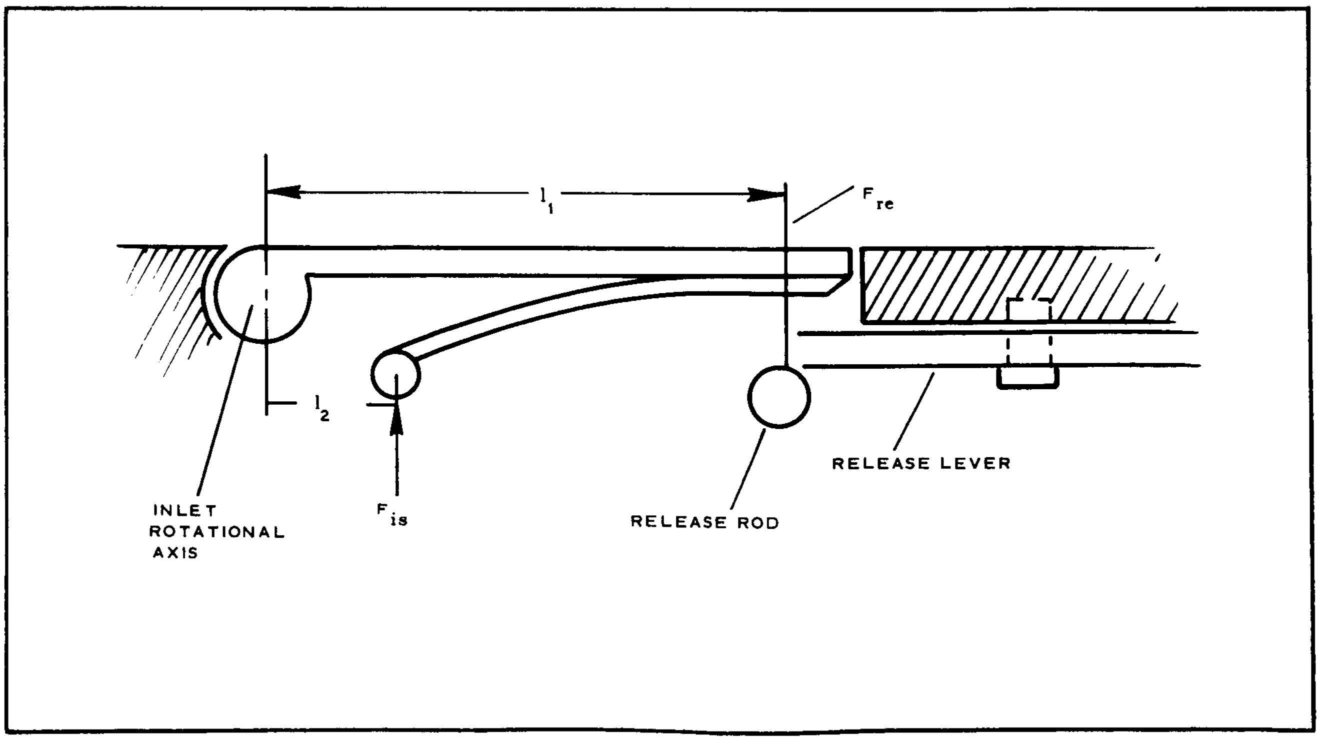

Figure D-3. - Forces Acting on Inlet Release Spring

The maximum friction force occurs as the inlet release lever starts to slide over the release rod. For steel on steel, the coefficient of static friction is $\mu = 0.28$; therefore,

$$F_{fm} = (0.28)(638)$$
$$= 1.78 \text{ lb.}$$

From the geometry in Figure D-4, F_{rs} is a minimum if l_1 is made as large as possible and l_2 as small as possible.

On the basis of the physical limitations involved, the maximum l_1 is 2.06 in. and the minimum l_2 is 0.90 in. Before the release spring can open inlet release, the following inequality must be satisfied:

$$F_{rs}(l_1) \geqq F_{fm}(l_2) \ .$$

Therefore,

$$F_{rs} \geqq \frac{(1.78)(0.90)}{2.06}$$
$$\geqq 0.78 \text{ lb.}$$

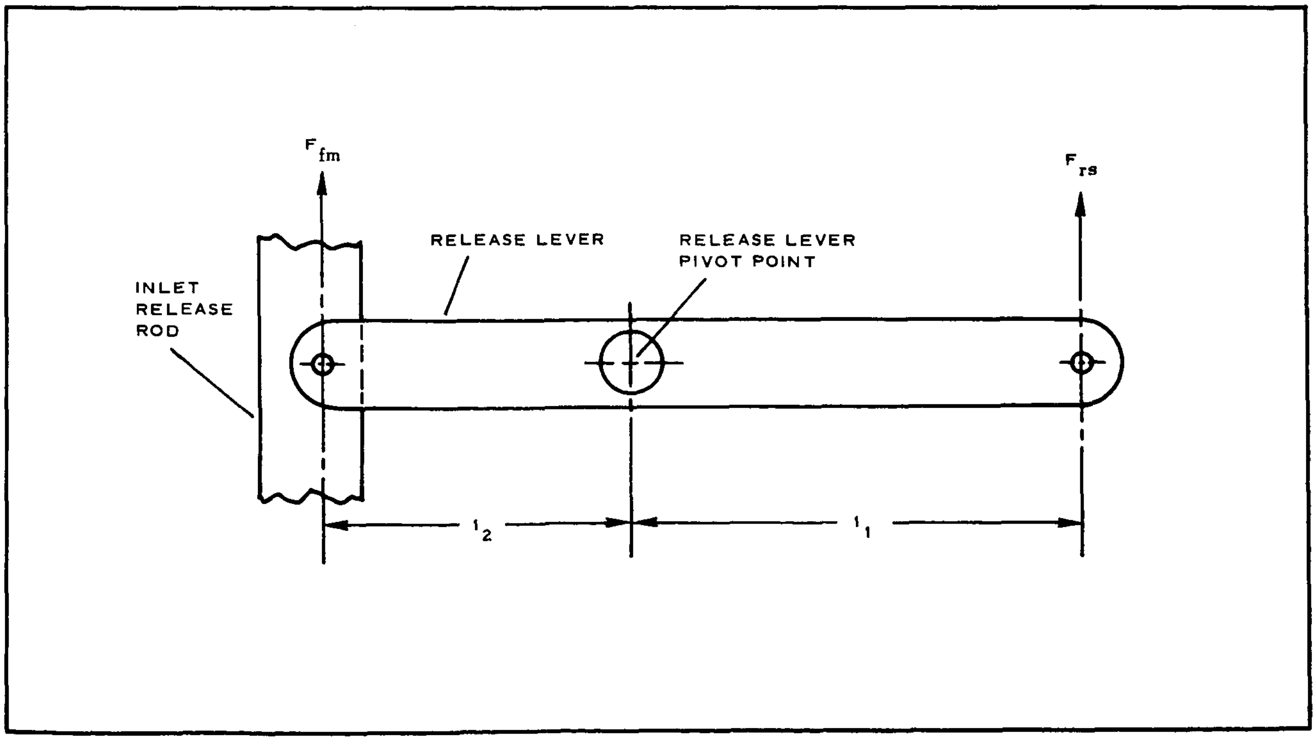

Figure D-4. - Forces Acting on Release Lever

Since the force developed by the release spring is transmitted about a circular plane of the cone (see Figure 13), a force input factor at the various locations on the circle must be determined. Table D-I summarizes these factors for the inlet locations (relative to the release spring) and the resulting release spring forces required.

By summing the forces in Table D-I and applying a safety factor of 2.0, the release spring must provide an 8.6-lb force to release the inlets. In addition the spring must possess the physical characteristic (see Figure D-5) to satisfy the following inequality:

$$l_i - l_f \geqq l_2 \theta.$$

TABLE D-I. - RELEASE SPRING INPUT FACTORS*

Inlet position relative to release spring (deg)	Input factor, H	HF_{rs}
20	1.24	0.97
110	1.27	0.99
200	1.40	1.09
290	1.60	1.25

*Source: Reference 19

Since $l_2 = 0.90$ in.,

$$l_i - l_f \geqq (0.90) \frac{3}{\pi}$$

$$\geqq 0.86 \text{ in.}$$

A helical spring with an $l_i = 3.0$ in. and an $l_f = 1.60$ in. satisfies this constraint. The spring chosen has a spring constant, K, of 14.5 lb/in. and will deliver a force for an elongation of 0.86 in.

$$F_{rs} = Kx$$

$$= (14.5)(0.86)$$

$$= 12.5 \text{ lb},$$

which is greater than the 8.6 lb previously determined as being required.

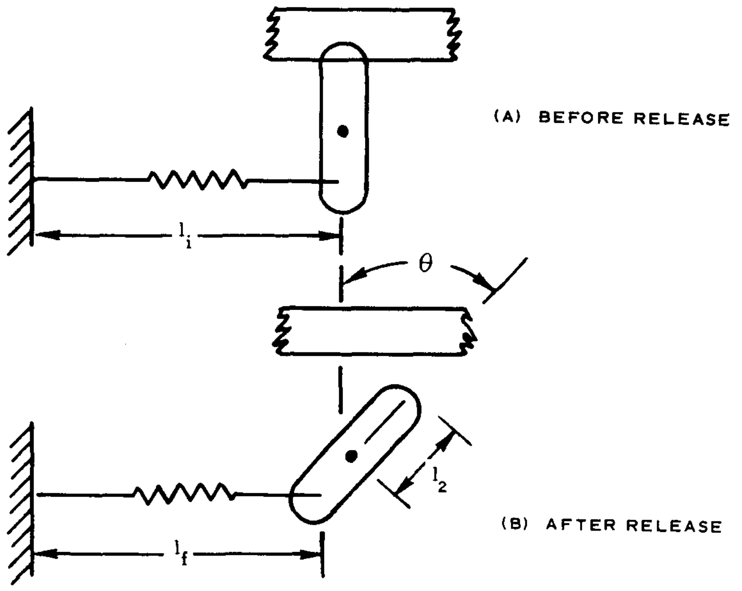

Figure D-5. - Release Spring Geometry before and after Release

Inlet Spring Forces

The force that the sliding flat spring was designed to exert to maintain the inlet in the deployed condition is computed by summing moments about the inlet rotational axis, from Figure D-6.

$$M = 0.0 = (0.5)(F_i) - xF_{s_o} \quad . \tag{D-1}$$

The force acting on the inlet, as determined previously, is 5.36 lb. Therefore from Equation D-1, for an inlet three inches in length,

$$xF_s = 8.04 \text{ in.-lb.} \tag{D-2}$$

The bending stress and deflection in the spring are defined by the following relations, respectively,

$$f_b = \frac{6F_s l}{wt^2} \tag{D-3}$$

and

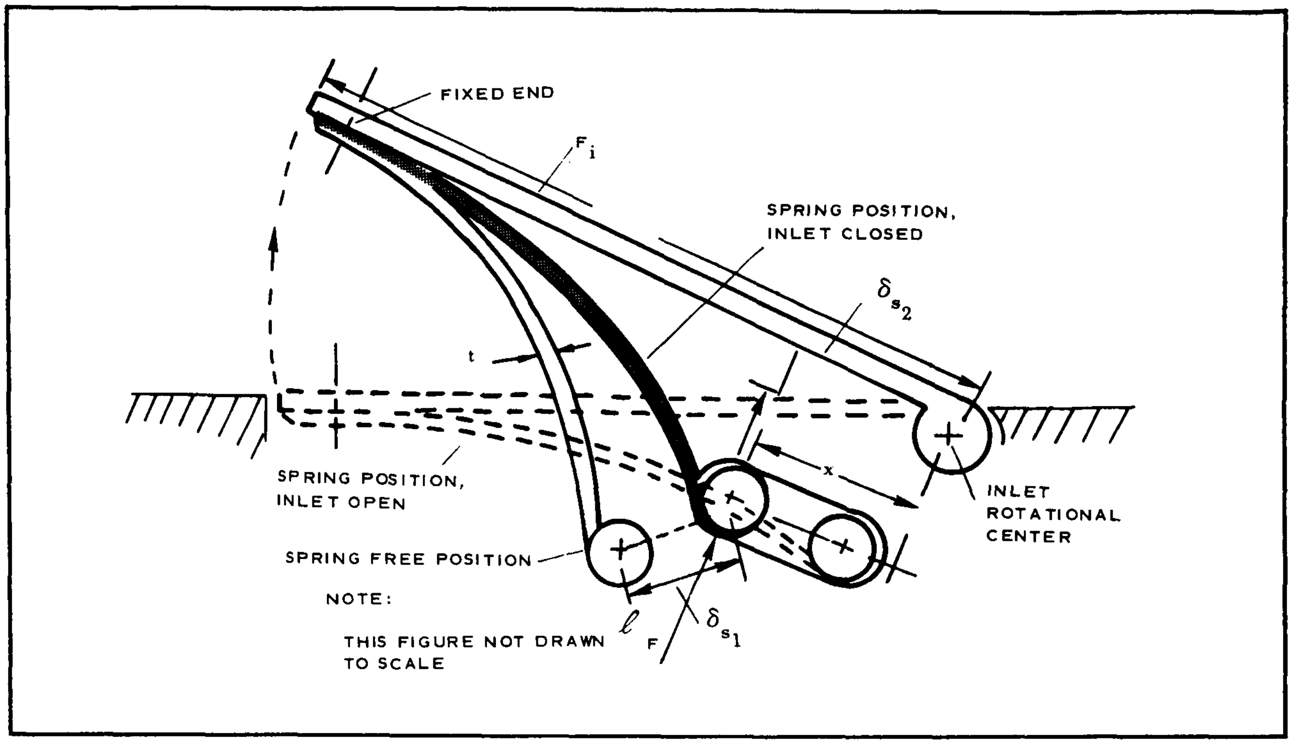

Figure D-6. - Aeroshell Inlet and Spring Geometry

$$\delta_s = \frac{F_s l^3}{3EI} \quad . \qquad \text{(D-4)}$$

Due to the number of variables involved in Equations D-2 through D-4, a trial-and-error method was employed to determine the maximum bending stress. A solution was sought that produced a bending stress below the ultimate of available steel alloys ($f_b \leq 200,000$ psi). A value of x = 0.83 in. satisfies this constraint as will be shown below. From Equation D-2,

$$F_{s_o} = \frac{8.04}{0.83}$$

$$= 9.68 \text{ lb.}$$

For a spring 2.0 in. long, 1.1 in. wide, and 0.04 in. thick, the resulting deflection required for the free end of the spring to move from the free position to the inlet open position (see Figure D-6) is:

$$\delta_{s_1} = \frac{F_{s_o} l^3}{3EI}$$

$$= \frac{(9.68)(2)(12)}{(3)(29 \times 10^6)(1.03)(0.04)^3}$$

$$= 0.162 \text{ in.}$$

The additional deflection, δ_{s_2}, that the spring must experience to permit the inlet to close is found from Figure D-6 (when drawn to scale) to be 0.26 in. Therefore, the maximum force in the spring, generated when the inlet is in the closed position, from Equation D-4 is:

$$F_{s_c} = \frac{3EI}{l^3}\left(\delta_{s_1} + \delta_{s_2}\right)$$

$$= \frac{(3)(29 \times 10^6)(1.03)(0.04)^3(0.422)}{(2.0)^3(12)}$$

$$= 25.0 \text{ lb.}$$

From Equation D-3

$$f_b = \frac{(6)(25)(2.0)}{(1.03)(0.04 \text{ in.})^2}$$

$$= 182{,}000 \text{ psi} < 200{,}000 \text{ psi}$$

Type 1090 spring steel tempered to 250,000 psi was chosen for this application.

The loading for the hard structure components making up the -103 assembly are either loaded less severely than the -101 and -105 assemblies or were previously shown to be adequate in Reference 3.

REFERENCES

1. Bohon, H. L.; and Miserentino, R.: Attached Inflatable Decelerator Performance Evaluation and Mission-Application Study. AIAA Paper No. 70-1163, AIAA Aerodynamic Deceleration Systems Conference (Dayton, Ohio), Sept. 1970.

2. Mikulas, M. M., Jr.; and Bohon, H. L.: Summary of the Development Status of Attached Inflatable Decelerators. AIAA Paper No. 68-929, AIAA Second Aerodynamic Decelerator Systems Conference (El Centro, California), Sept. 1968.

3. Barton, R. R.: Development of Attached Inflatable Decelerators for Supersonic Application. NASA CR-66613, 1968.

4. Houtz, N.: Optimization of Inflatable Drag Devices by Isotensoid Design. AIAA Paper No. 64-437, First Annual AIAA Meeting (Washington, D.C.), 29 June through 2 July 1964.

5. Baker, D.C.: Investigation of an Inflatable Decelerator Attached to a 120-Deg Conical Entry Capsule at Mach Numbers from 2.55 to 4.40. AEDC-TR-68-227, U.S. Air Force, October 1968.

6. Baker, D. C.: Investigation of an Attached Inflatable Decelerator with Mechanically Deployed Inlets at Mach Numbers from 2.25 to 4.75. AEDC-TR-69-132, U.S. Air Force. June 1969.

7. Reichenau, David E. A.: Investigation of an Attached Inflatable Decelerator System for Drag Augmentation of the Voyage Entry Capsule at Supersonic Speeds. AEDC TR-68-71, U.S. Air Force, April 1968.

8. Bohon, Herman L., and Miserentino, R.: Deployment and Performance Characteristics of 5-Foot-Diameter Attached Inflatable Decelerators From Med Number 2.2 to 4.4. NASA TND-5840, August 1970.

9. Gillis, C. L.: Aerodynamic Deceleration Systems for Space Missions. AIAA Paper No. 68-1081, AiAA Fifth Annual Meeting (Philadelphia, Pa.), Oct. 1968.

10. Burgess, J. L.; Sowa, W. W.; and Houmard, J. E.: Flight Model Attached Inflatable Decelerator (AID) Program. GER-14939. Goodyear Aerospace Corporation, Nov. 1970.

11. Deveikis, W. D.; and Sawyer, J. W.: Static Aerodynamic Characteristics, Pressure Distributions, and Ram-Air Inflation of Attached Inflatable Decelerator Models at Mach 3.0. NASA TN D-5816, May 1970.

12. Reshotko, E.; and Tucker, M.: Approximate Calculation of the Compressible Turbulent Boundary Layer with Heat Transfer and Arbitrary Pressure Gradient. NACA TN 4154, December, 1957.

13. Weinberg, S. A.; and Tucker, D. W.: User's Manual for the Boundary Layer and Wake Computer Program. GER-14534. Goodyear Aerospace Corporation, September, 1969.

14. Barton, R. R.: Development of Inflatable Attached Supersonic Decelerators, Design Report - Phase I. GER-13429. Goodyear Aerospace Corporation, 18 August 1967.

15. Roark, R. J.: Formulas for Stress and Strain. Third ed. McGraw-Hill Book Co., Inc., 1954.

16. Ames Research Staff: Equations, Tables, and Charts for Compressible Flow. NACA Report 1135, 1953.

17. Stallings, R. L.; and Tudor, D. H.: Experimental Pressure Distribution on a 120° Cone at Mach Numbers from 2.96 to 4.63 and Angles of Attack from 0 to 20. NASA TN D-5054, March 1969.

18. Campbell, J. R.; and Tudor, D. H.: Pressure Distribution on 140°, 160°, and 180° Cones at Mach Numbers from 2.30 to 4.63 and Angles of Attack from 0° to 20°. NASA TN D-5204, May 1969.

19. Anon.: Tru-Lay Push-Pull Controls. Folder DH-219-B, American Chain and Cable Company, Inc. (Detroit, Michigan).